MorphOMICs, a tool for mapping microglial morphology, reveals brain region- and sex-dependent phenotypes

by

Gloria Colombo

October, 2022

A thesis submitted to the
Graduate School
of the
Institute of Science and Technology Austria
in partial fulfillment of the requirements
for the degree of
Doctor of Philosophy

Committee in charge:
Prof. Dr. Caroline Muller
Prof. Dr. Sandra Siegert
Prof. Dr. Beatriz Vicoso
Prof. Dr. Sarah Ackerman

The thesis of Gloria Colombo, titled *Microglial MorphOMICs, a tool for mapping microglial morphology, reveals brain region- and sex-dependent phenotypes*, is approved by:

Supervisor: Sandra Siegert, ISTA, Klosterneuburg, Austria

Signature:

Committee Member: Beatriz Vicoso, ISTA, Klosterneuburg, Austria

Signature:

Committee Member: Sarah Ackerman, Center for Brain Immunology and Glia, Washington University, Saint Louis, MO 63130, USA

Signature:

Defense Chair:Caroline Muller, ISTA, Klosterneuburg, Austria

Signature:

Signed page is on file

ISTA Thesis, ISSN: 2663-337X

I hereby declare that this thesis is my own work and that it does not contain other people's work without this being so stated; this thesis does not contain my previous work without this being stated, and the bibliography contains all the literature that I used in writing the dissertation.

I declare that this is a true copy of my thesis, including any final revisions, as approved by my thesis committee, and that this thesis has not been submitted for a higher degree to any other university or institution.

I certify that any republication of materials presented in this thesis has been approved by the relevant publishers and co-authors.

Signature: ___ _____

Gloria Colombo

October, 2022

Signed page is on file

Abstract

Environmental cues influence the highly dynamic morphology of microglia. Strategies to characterize these changes usually involve user-selected morphometric features, which preclude the identification of a spectrum of context-dependent morphological phenotypes. Here, we develop MorphOMICs, a topological data analysis approach, which enables semi-automatic mapping of microglial morphology into an atlas of cue-dependent phenotypes, overcomes feature-selection bias and minimizes biological variability.

First, with MorphOMICs we derive the morphological spectrum of microglia across seven brain regions during postnatal development and in two distinct Alzheimer's disease degeneration mouse models. We uncover region-specific and sexually dimorphic morphological trajectories, with females showing an earlier morphological shift than males in the degenerating brain. Overall, we demonstrate that both long primary- and short terminal processes provide distinct insights to morphological phenotypes. Moreover, using machine learning to map novel condition on the spectrum, we observe that microglia morphologies reflect a dose-dependent adaptation upon ketamine anesthesia and do not recover to control morphologies.

Next, we took advantage of MorphOMICs to build a high-resolution and layer-specific map of microglial morphological spectrum in the retina, covering postnatal development and rd10 degeneration. Here, following photoreceptor death, microglia assume an early development-like morphology. Finally, we map microglial morphology following optic nerve crush on the retinal spectrum and observe a layer- and sex-dependent response.

Overall, MorphOMICs opens a new perspective to analyze microglial morphology across multiple conditions, and provides a novel tool to characterize microglial morphology beyond the traditionally dichotomized view of microglia.

Acknowledgments

The work presented in this Thesis was carried out at the Institute of Science and Technology Austria (ISTA), and was partially founded by the European Commission through the International IST Doctoral Program (Grant number: 665385). I thank the scientific service units at ISTA, in particular Michael Schunn's team at the preclinical facility, and especially our colony manager Sonja Haslinger, for excellent support. I am also grateful to the ISTA Imaging & Optics facility, and in particular Christoph Sommer for helping with the data file conversions. I also thank Ricarda Erhart from the ISTA Scientific Computing Unit for improving the script performance.

I owe special thanks to my supervisor, Prof. Sandra Siegert, for all her support in these years and for encouraging me without ever stopping to be optimistic on my projects.

My defense would not have been possible without any of Siegert's group members. Ale, Rouven, Ryan, Maggie, Balint, Verena, Medina, Fleur, Aaron, Nathalie I must thank you all one by one for the support, the scientific (and often not) discussions, the experiments and the laughs we have had in the past years. In particular, I want to thank Ryan, who literally made this day possible. Thank you for your neatness, your patience and your hard working with me on this project. I then I thank Alessandro, the most gifted mouse surgeon a lab could ever want, you taught me almost everything I know in the lab. Then comes Rouven, the smartest, kindest and best colleague I could ever hope for to share this journey with. It is going to be weird not to have you sitting on my right side. I think I am going to miss it.

I thank all the people from ISTA and outside, who I have met and with whom I have shared moments here. In particular, Rachele and Jasmin for sharing moments inside and outside ISTA. Seeing your amazing kids growing up was the best distraction from the lab.

Last but absolutely not least, I thank my family. You taught me curiosity as a kid, and encouraged me to follow my interests while I was growing up even when you stopped understanding what they were all about.

About the Author

Gloria Colombo obtained a *BSc* in molecular biotechnology and a *MSc* in neurobiology at the University of Pavia (Italy). In 2016, she joined the ISTA graduate school program and affiliated to Prof Siegert's laboratory in 2017. Her project aimed to develop a new strategy to analyze the impact of region and sex on microglial morphology in health and disease. She identified that microglial morphology is deeply influenced by brain region and sex, and built an algorithm to map microglial morphology from regions of interest. The results of this study led to a publication in nature neuroscience in 2022. She is now working on expanding MorphOMICs to the retina to apply the MorphOMICs algorithm to sub-region and derive the high time-resolution spectrum of their morphology.

Furthermore, Gloria has been involved in multiple projects to elucidate microglia function, amongst others how microglia respond to ketamine anesthesia (Venturino *et al.* 2021) and upon mitochondria manipulation (Maes *et al.* 2022) as well as she was involved in optimization of viral vectors for microglia transduction (Maes *et al.* 2021) and designing chemogenetic G protein-coupled receptors (Schulz *et al.* 2022). She also co-authored a review article discussing the current limitations and challenges of employing viruses for microglia transduction (Maes *et al.* 2019). Gloria presented her research at several international conferences such as the European glia meetings Porto (2019), the European retina meetings in Paris (2017) and Helsinki (2019), and ARVO in Vancouver (2019). Her PhD was partially funded by the European Union's Horizon 2020 research and innovation program. She received travel support from Austrian Neuroscience Association (ANA) and Erasmus+ to attend the CAJAL Advanced Neuroscience Training Program in Bordeaux (2016) and travel support from Erasmus+ to attend the Neuroscience School of Advanced Studies in Venice (2022).

Besides her work in the lab, in 2022, Gloria took part to the organizing committee of the Young Scientists Symposium entitled "Energy", a yearly interdisciplinary meeting organized by graduate students and postdoctoral fellows from different disciplines represented ad IST Austria.

List of Publications

1. **Colombo, G.**, John Cubero, R., Kanari, L , Venturino, A. , Schulz, R. , Scolamiero, M. , Agerberg, J. , Mathys, H. , Tsai, L.H. , Chachólski, L. , Hess, H., Siegert, S. "Microglial MorphOMICs unravel region- and sex-dependent morphological phenotypes from postnatal development to degeneration". Nat.Neuroscience. https://doi.org/10.1038/s41593-022-01167-6.

2. Rouven Schulz, Medina Korkut-Demirbaş, Alessandro Venturino, **Gloria Colombo**, Sandra Siegert. "Chimeric GPCRs mimic distinct signaling pathways and modulate microglia responses." Nature Communications 13.1 (2022): 1-26.

3. Margaret E. Maes, Gabriele M. Wögenstein, **Gloria Colombo**, Raquel Casado-Polanco, Sandra Siegert. "Optimizing AAV2/6 microglial targeting identified enhanced efficiency in the photoreceptor degenerative environment". Molecular Therapy – Methods & Clinical Development. 2021 Sep 14;23:210-224. doi: 10.1016/j.omtm.2021.09.006. PMID: 34703843; PMCID: PMC8516996.

4. Alessandro Venturino, Rouven Schulz, Héctor De Jesús-Cortés, Margaret E. Maes, Bálint Nagy, Francis Reilly-Andújar, **Gloria Colombo**, Ryan John A. Cubero, Florianne E. Schoot Uiterkamp, Mark F. Bear, Sandra Siegert. "Microglia enable mature perineuronal nets disassembly upon anesthetic ketamine exposure or 60-Hz light entrainment in the healthy brain." Cell Report. 2021 Jul 6;36(1):109313. doi: 10.1016/j.celrep.2021.109313. PMID: 34233180; PMCID: PMC8284881

5. Margaret E. Maes, **Gloria Colombo**, Rouven Schulz, and Sandra Siegert. "Targeting microglia with lentivirus and AAV: Recent advances and remaining challenges." Neuroscience letters (2019):134310. doi: 10.1016/j.neulet.2019.134310. PMID: 31158432; PMCID: PMC6734419.

Under review

1. Margaret E. Maes, **Gloria Colombo**, Felix Sternberg, Elena E. Pohl, and Sandra Siegert. "Sex, stress and UCP2: mitochondria illuminate microglial identity beyond the dichotomy." bioRxiv, https://doi.org/10.1101/2022.08.22.504738

List of Collaborators and Publications mentioned in this thesis

MorphOMICs:

Conceptualization - **Gloria Colombo**; Ryan John A Cubero, PhD; Lida Kanari, PhD; Martina Scolamiero, PhD; Jens Agerberg, PhD; Wojciech Chachólski, PhD; Kathryn Hess Bellwald, PhD; Sandra Siegert, PhD

Methodology - **Gloria Colombo**, Ryan John A Cubero, PhD; Lida Kanari, PhD; Sandra Siegert, PhD

Software - Ryan John Cubero, PhD; Lida Kanari, PhD;

Validation - **Gloria Colombo**; Ryan John A Cubero, PhD;

Formal analysis - **Gloria Colombo**; Ryan John A Cubero, PhD; Lida Kanari, PhD;

Investigation - **Gloria Colombo**; Ryan John A Cubero, PhD; Alessandro Venturino, PhD; Rouven Schulz, PhD; Sandra Siegert, PhD

Resources - Lida Kanari, PhD; Hansruedi Mathys, PhD; Li-Huei Tsai, PhD

Data Curation - **Gloria Colombo**; Ryan John A Cubero, PhD

Writing original Draft and Visualization - **Gloria Colombo**; Ryan John Cubero, PhD; Sandra Siegert, PhD

Supervision, Project Administration, Funding Acquisition - Sandra Siegert, PhD

Stable ranks:

Conceptualization - **Gloria Colombo**; Ryan John A Cubero, PhD; Lida Kanari, PhD; Martina Scolamiero, PhD; Jens Agerberg, PhD; Wojciech Chachólski, PhD; Kathryn Hess Bellwald, PhD; Sandra Siegert, PhD

Software Validation and Formal Analysis - Ryan John A Cubero, PhD; Jens Agerberg, PhD

Publications appearing in this thesis:

1. **Colombo, G.**, John Cubero, R., Kanari, L , Venturino, A. , Schulz, R. , Scolamiero, M., Agerberg, J. , Mathys, H. , Tsai, L.H. , Chachólski, L. , Hess, H., Siegert, S. "Microglial MorphOMICs unravel region- and sex-dependent morphological phenotypes from postnatal development to degeneration". Nat.Neuroscience. https://doi.org/10.1038/s41593-022-01167-6

Table of Contents

List of Figures and tables

List of Extended Data Material

List of Abbreviations

TMD	Topological morphology descriptor
KXA	Ketamine-Xylazine-Acepromazine
OB	Olfactory bulb
FC	Frontal cortex
DG	Dentate gyrus of the hippocampus
S1	Primary somatosensory cortex
SN	Substantia nigra
CN	Cochlear nucleus
CB	Cerebellum
Mg	Microglia
CNS	Central nervous system
UMAP	Unifold manifold approximation and projection
DAM	Disease-associate microglia
ARM	Activated response microglia
IRM	Interferon-responsive microglia
HAM	Human Alzheimer's disease microglia
MIMS	Microglia inflamed in multiple sclerosis
LDAM	Lipid droplet accumulating microglia in aging mice and human
WAM	White matter associate microglia
ATM	Axon-tract associated microglia
PAM	Proliferative-region associated microglia
CSF1R	colony stimulating factor 1 receptor
DAP12	DNAX activation protein 12
IRF8	Interferon regulatory factor 8
IL-34	Interleukin 34
OPCs	Oligodendrocyte progenitor cells
IGF	Insulin-like growth factor
AD	Alzheimer's disease

TLRs	Toll-like receptor
GWAS	Genome-wide association studies
APOE	Apolipoprotein E
TREM2	Triggering receptor expressed on myeloid cells 2
PGE2	Prostaglandin-E2
MMP-9	Metalloproteinase-9
IL-10	Iinterleukin-10
LPS	Lipopolysaccharide
PCA	Principle component analysis
SVM	Support vector machine
FLIM	Fluorescence lifetime imaging microscopy
ANN	Artificial neural network
CD68	Cluster of differentiation 68
CaMKII	Calcium/calmodulin-dependent kinase-2
Cdk6	Cyclin-dependent kinase-6
PNN	Perineuronal nets
RGCs/GCL	(Retinal) ganglion cell layer
INL	Inner nuclear layer
IPL	Inner plexiform layer
ONL	Outer nuclear layer
OPL	Outer plexiform layer
CD11c	Cluster of differentiation-11c
RP	Retinitis pigmentosa
ONC	Optic nerve crush
LM	L-Measure
AI	Artificial intelligence
tSNE	t-distributed Stochastic Neighbor Embedding

1 Introduction

Approximately 10% of the cells in the brain have a mesodermal origin and belong to the innate immune system [1]. These resident macrophages named microglia occupy the entire brain and were merely seen as supporting cells for neuronal function. Microglia were first described by Pio Del Rio-Hortega and referred to as the "third element of the central nervous system" [2–4]. They are disposed in close proximity to neurons and preferably to synaptic layers, where they interact with the neuronal environment and ensure tissue homeostasis [5]. During development, health, and disease, microglia are involved in synaptic function and synaptic remodeling putting microglia on the spotlight for any alteration in the nervous system. Although microglia populate the entire brain, their distribution varies across regions or even sub-regions like white and gray matter [6,7]. Moreover, microglia are extremely sensitive to the micro-environmental modifications. They regulate the activity of neurons through feedback mechanisms, whereas neurons influence microglia biology with their electrophysiological properties [8–12]. A recent paper from Stogsdill and colleagues showed how microglia across the brain adapt to the identity of surrounding neurons, and detected layer-dependent ligand-receptor pairs candidates that might explain the microglia-neuron crosstalk [13].

1.1 Microglia support the circuit formation during brain development

Microglia derive from erythromyeloid precursors in the yolk sac and migrate to the mouse embryo nervous system at the onset of blood circulation around E8.5 [14]. From E9/E9.5, they exit the blood stream and colonize the neuroepithelium during the wave of CNS vascularization and give rise to embryonic microglia [14–16]. Microglia distinguish from other myeloid cells based of their transcriptomic profile, where CSF1R (colony-stimulating factor 1 receptor), DAP12 (DNAX-activation protein 12), IRF8 (interferon regulatory factor 8) and transcription factor PU.1 (also known as SPI1) are essential for their survival and maintenance [17–20]. Since they enter the nervous system prenatally, microglia are in a privileged position to participate in the maturation of neuronal connectivity. Microglia prune synapses during circuitry formation and phagocytose newborn neurons in response to IL-33, C1q and C3 produced by astrocytes and neurons [21–23]. Transcriptional analysis confirmed these microglia functions based on gene signatures typically for enhanced phagocytosis and proliferation (**Fig. 1**) [8,24].

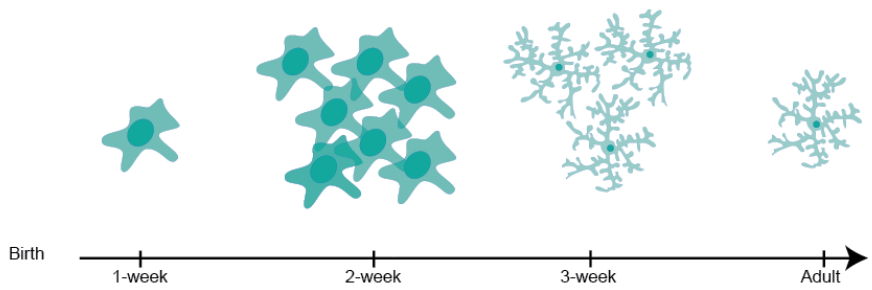

Fig. 1. Microglial phenotype during postnatal development. Microglia display an amoeboid morphology after birth and an increased density, which peaks at around 2-weeks of age in mice

Microglia phagocytosis occurs with a gradual increase during the first two to three postnatal weeks, and then decreases as structural and functional stabilization of the circuitry becomes established [25–29]. Notably, microglial function is not limited to phagocytosis of synapses and neurons [30]. Microglia also influence neuronal activity through the release of key molecules such as brain-derived neurotrophic factor (BDNF), which impacts inhibitory transmission and regulates synaptic plasticity also in adulthood and in response to damage [31–33]. Moreover, microglia promotes the maturation of oligodendrocyte progenitor cells (OPCs) due to the production of insulin-like growth factors (IGF) and a physical exchange between the cell types [34–36]. Thus, microglia play a critical role and are likely part in the development of psychiatric disorders such as major depression, schizophrenia, autism, obsessive-compulsive disorder, and Tourette syndrome [37].

1.2 Microglia response to neurodegeneration

Microglia are extremely sensitive to subtle changes in the brain and as such they have been shown to be responsive in various neurodegenerative disorders such as Alzheimer's disease (AD) [38]. Genome-wide association studies (GWAS) identified genetic loci that highly correlate with the risk of AD such as Apolipoprotein E (APOE) and TREM2, both are highly enriched in microglia and confirming their pathological relevance [39,40,49–53,41–48]. The exact role of microglia in degenerations has not been fully addressed and contradictory results propose them as either neuroprotective or detrimental [54]. Recent works in the field of AD suggest that microglia could exert both effects. One of the hallmarks of AD are $A\beta_{42}$ fibrils that form the amyloid plaques. These plaques trigger a robust immune response [55], which is sensed with the Toll-like receptors (TLRs) leading to an innate immune response directed against plaques [56]. Whereas this can be seen initially as neuroprotective, it leads to a prolonged inflammation that eventually turns toxic. Similarly, cellular degradation pathways such as phagocytosis and autophagy, the mechanism for turning over organelles and protein too large to be targeted by the proteasome, might have both a protective and detrimental effect respectively during the

premature and the late state of the pathology. Confirming this, they are found to be dysregulated in AD patients [57–59]. In Parkinson's disease, microglia engulf exogenous alpha-synuclein to protect neurons from the toxic effects of its accumulation. However, the uptake causes metabolic stress on microglia due to alpha-synuclein accumulation, which reduces microglia capability to continue degrade. A recent study has been shown that microglia build tunneling nanotube, which allow them to spread the toxic cargo (**Fig. 2**) [60]. Overall, microglia have an impact in neurodegeneration, which we are just starting to uncover.

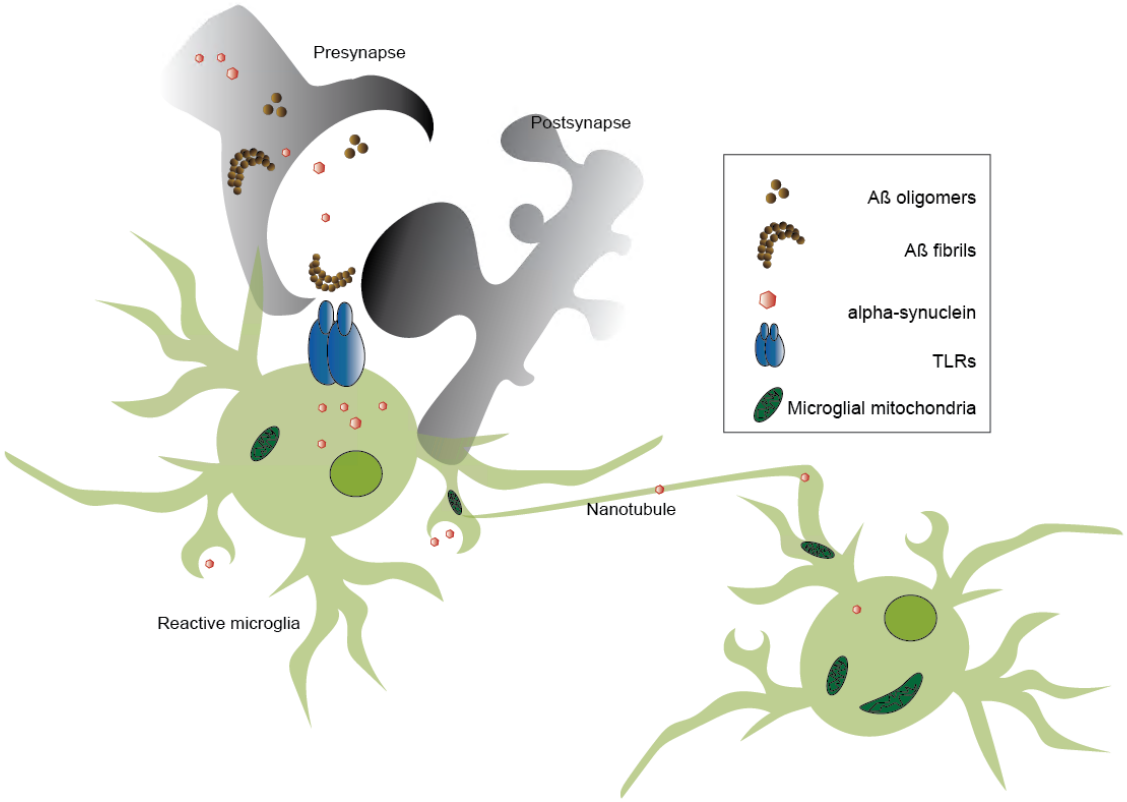

Fig. 2. Microglial response to AD degeneration. Microglia sense Aß42 fibrils and oligomers through TLRs. To face cellular stress induced by and tau-synuclein, they build nanotubes allowing the distribution of cargo and the exchange of mitochondria with non-stressed microglia

1.3 Microglia: one cell, multiple identities

A current main challenge in the community is how to deal with the variability of microglia functions. Microglia regulate neuronal activity, provide trophic factors to ensure healthy function and during development prune away nonfunctional synapses, which influences their states. However, to define microglial states has been challenging [61]. Classically, microglia were considered a uniform cell type, existing in either a surveilling form with highly ramified processes or a reactive, phagocytic form causing an amoeboid morphology [62]. When reacting to an insult, microglia were hypothesized to undergo two alternative activation programs

defined as M1 and M2 (**Fig. 3**): M1 describes a microglia responsible for the release of pro-inflammatory signaling, while M2 microglia have been seen as anti-inflammatory and active contributors to tissue healing and debris clearance [63,64].

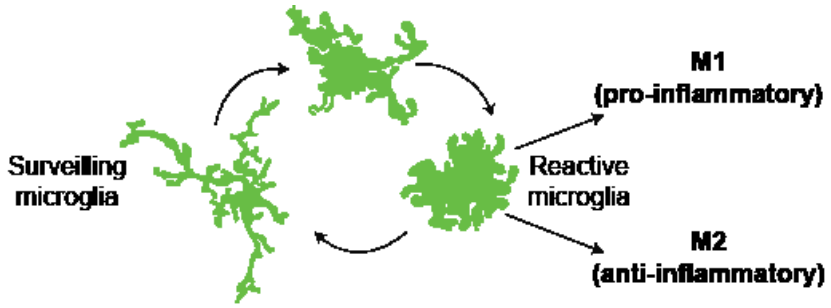

Fig. 3. Microglia morphology undergoes dynamic changes. Schematic illustrating microglial morphological changes, classically associated to either reactive or surveilling microglia

However, further observations at microglial functions in health and during pathological response suggested a higher degree of microglial diversity as well as multiple activation phenotypes where classical and alternative activation co-exist [63]. In the past years, several states of microglia polarization have been described such as the alternative activation (M2a), alternative type II activation (M2b), acquired deactivation (M2c) and even an additional activation state M3 [65,66]. This suggests that the M1/M2 theory oversimplifies the range of microglial activation states [67]. Classically, the concept of heterogeneous microglia has been based on their transcriptional response [9–11,68–71]. With the advent of single cell RNA sequencing analysis, microglia have been profiled across conditions like development and disease progression [9]. However, each transcriptomic study defined new microglial clusters based on their gene signature causing the growth of a complex nomenclature to indicate microglia states from different conditions (**Tab. 1**).

Name	**Description**	**Publication**
DAM	Disease associated microglia	Keren-Shaul et al., 2017 [72]
ARM	Activated response microglia	Sala Frigerio et al., 2019 [73]
IRM	interferon responsive microglia	
HAM	human Alzheimer's disease microglia	Srinivasan et al., 2020 [74]
MIMS	Microglia inflamed in multiple sclerosis	Absinta et al., 2021 [75]
LDAM	Lipid droplet accumulating microglia	Marschallinger et al. 2020 [76]
WAM	White matter associated microglia	Safaiyan et al., 2021 [77]
ATM	Axon tract associated microglia	Hammond et al., 2018 [78]
PAM	Proliferative-region-associated microglia	Li et al., 2018 [79]

Tab. 1. Overview of various microglial nomenclatures based on transcriptomic signatures.

Overall, transcriptomics studies alone do not suffice in enhancing the understanding microglial states and only explore one level of their heterogeneity. As an example, microglial turnover

rate is higher close to the subventricular zone, where microglia play a role in sustaining neurogenesis [80]. Amongst the factors that can influence microglial heterogeneity sex should be considered, but also other parameters like microglial motility, their cell density, or the regulation of their metabolism might also have a role. However, they have not been systematically analyzed. A recent review brought the microglia nomenclature to the attention of the community and stressed that the traditionally form of surveillant and reactive microglia is too simplified [81]. They suggest that it is critical to determine microglia based on the environment, in which they are embedded, combined with a multidisciplinary approach to define the microglial functional state.

1.4 The debated sexual dimorphism of microglia

In the past years, a growing body of evidence suggested that microglia from males and females differ at transcriptomics, proteomics, morphological and functional level across health and disease [82–85]. However, literature presenting a systematic investigation of the regional impact of sexual dimorphism impact is limited.

The immune system acts as a bridge between hormonal exposure and the development of CNS sexual dimorphism [86]. Microglia are key players during postnatal circuital maturation and in the sexual differentiation of the brain [86–88]. Concomitant to peaks in sex hormones around the second postnatal week, microglial density increases differently in females and males during the first postnatal days. Immediately after birth, the number of microglia is higher in males than in females but reverses at around P30 [89]. Moreover, microglia in neonatal female hippocampus have more phagocytic cups than in male, target more neuronal progenitors and healthy cells, and display higher expression of several phagocytic pathway genes in the hippocampus compared to males [90]. Morphologically, female microglia have longer and thicker processes. In contrast, males display a more pro-inflammatory baseline phenotype [85,88,90–93]. To confirm a potential impact of hormones in postnatal microglial sexual-dimorphism, female were exposed to estradiol. This reduced the number of phagocytic cups in female microglia to male microglia levels [90]. Similarly, administration of prostaglandin E2 (PGE2) in the brains of neonatal females causes a male sexual behavior as adults (**Fig. 4**) [94].

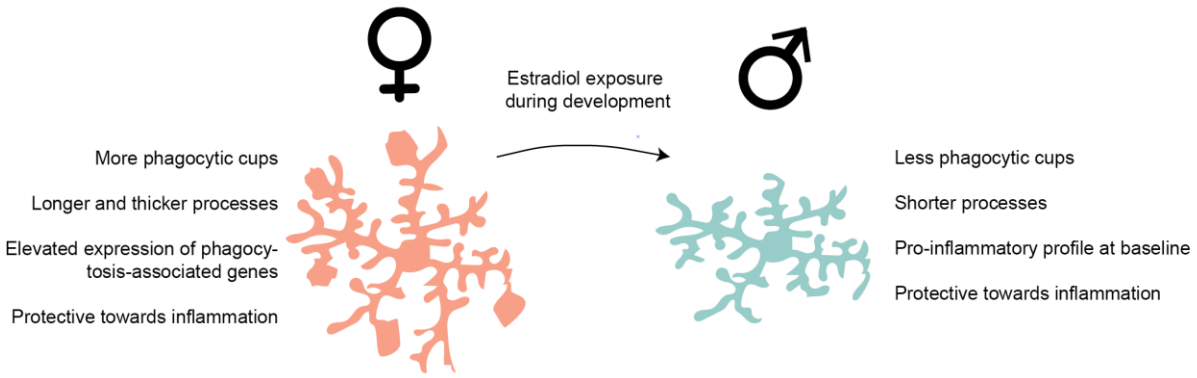

Fig. 4. Postnatal sexual dimorphism of microglia. Schematic showing the main sex-specific features of microglia during the postnatal development of the brain. Exposure of female to estradiol during a postnatal critical time-window induces the masculinization of microglial phenotype [90].

However, the role of circulating estrogens is only partially understood. Both the ovariectomy and the transplant of females microglia into males recipient showed that female microglia tends to keep their protective phenotype [85]. However, a caveat of such studies is that hormonal exposure is difficult to control experimentally, that ovariectomy only decreases circulating estrogens, and that the transplant of microglia requires a prior depletion which alone might influence observations. Other studies suggest that estrogens push microglia to an anti-inflammatory phenotype *in vitro* and *in vivo* and prevent the production of inflammatory mediators like iNOS (inducible form of NO synthase), prostaglandin-E2 (PGE2), and metalloproteinase-9 (MMP-9) [85,95–97]. They also facilitate the progression of the inflammatory process toward the IL10-dependent phenotype, which is responsible for tissue remodeling and the restoration of homeostatic conditions [96]. Interestingly, the removal of endogenous estrogens decreases both pro- and anti-inflammatory cytokine production [98]. Thus, a drop in estrogens during menopause is linked to increased degeneration in females [99]. During Alzheimer's degeneration, estrogen replacement therapies have been shown to delay microglia activation and prevents the induction of inflammatory mediators in the brain [100]. Moreover, we have a very limited understanding on the influence of sex on microglial morphology, as we miss a systemic investigation.

1.5 Determining microglia morphology

In neuroscience, morphology greatly contributed to define a common nomenclature of cell types with similar shape and became quickly a gold standard [101,102]. The analysis of cellular shape provides important insights on its function as e.g. a highly branched dendritic tree indicate many inputs, the dimension of their spines correlates with their excitability etc.

Whether a similar statement holds true for microglia morphology is not known. Our first insights about microglia morphology came from observations of Del Rio-Hortega. He adapted the metal impregnation staining method used on neurons and categorized microglia across different conditions. Del Rio-Hortega distinguished several subtypes of microglia: perineuronal microglia with a round soma and centrifugal ramified processes; perivascular microglia with a more elongated shape and contacting the parenchymal vessels [103]; in the injured brain with retracted processes and thicker somata. His observation suggested functional adjustment of microglia reflecting in their shapes. The advancement of immunohistochemistry and immunofluorescence staining techniques in the early 2000s helped the effort to study microglial morphology and their dynamics. Several key markers are highly enriched in microglia: Iba1 [104], F4/80 [105], Cx3cr1 [106], CD45^{low} and CD11b^{high} [107], P2rY12 [108] and TMEM119 [109] amongst others (**Fig. 5**). One drawback of these antibodies is that they also label monocytes, macrophages, dendritic cells, T-cells, and natural killer cells [1,110].

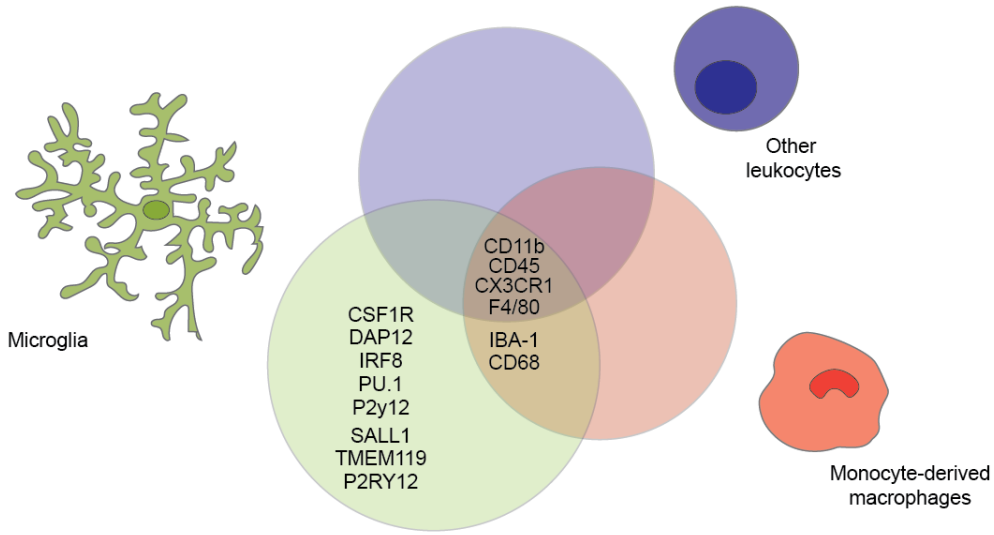

Fig. 5. Microglial markers. Schematic showing the most common markers for microglia staining, including those that are unique and those that are shared with monocyte-derived macrophages and other leukocytes.

Besides immunostaining, the development of transgenic animals carrying an immunofluorescent tag has been instrumental to visualize microglial cells also under *in vivo* conditions [111] and identify their fast response to injuries and degeneration [112–115]. These studies also showed that microglia demonstrate a high degree of morphological and functional adjustment as soon as their microenvironment changes [116]. Thus, morphological modifications in microglia are an early event, which precedes behavioral symptoms during neurodegeneration or persist after the resolution of external stimuli [117–119].

1.5.1 Strategies to analyze microglial morphology

In neuroscience, several strategies to trace morphologies have been established. These diverse approaches starting from simple morphometric-based classification to integrated support vector machine approaches have been applied for microglia (**Tab. 2**). The first analysis attempts to compare microglial morphology across conditions relied on simple classifiers such as their area, perimeter or length of their processes [120]. Dedicated software for image analysis such as ImageJ, Imaris, or Neurolucida makes it now possible to either manually or semi-automatically extract multiple morphometric parameters and to compare them across conditions.

In the next paragraphs, I will review the most used approaches for the morphological analysis of microglia and focus on the strengths and weaknesses of each method. I will then present the novel interdisciplinary approaches that we have developed to overcome the challenges in the field. Finally, I propose future perspectives where standardized unbiased automatic analysis of microglial morphology proves as a powerful tool for predicting sex and regional differences in microglial dynamics during development and disease.

Authors	Animal model	Analyzed region	Condition	Sex	Main technique
Sholl et al., 1953 [121]	Cat	Visual and motor cortices	Naïve	ND	Sholl analysis
Lawson et al., 1990 [12]	Mouse	Hippocampus, olfactory telencephalon, basal ganglia, substantia nigra, corpus callosum, cerebellum, brainstem, cerebral cortex, thalamus hypothalamus	Naive	ND	Analysis of microglia distribution
Wu et al., 1992 [120]	Rat	Corpus callosum	Development	ND	Feature extraction, statistical comparison
Soltys et al., 2005 [122]	Rat	cerebral cortex, hippocampus	Ischemia	ND	Feature extraction and dimensionality reduction with principal component analysis (PCA)
Kozlowski and Weimer, 2012 [123]	Mouse	Neocortex	LPS	ND	Automated segmentation and feature extraction
Valous et al., 2013 [124]	Mouse	ND	Ischemia	ND	Multi-step automatic segmentation
Lu et al., 2013 [125]	Rat	ND	Brain tissue perturbed by the insertion of a recording device	ND	Automatic tracing, extraction of 127 features based on the L-measure and unsupervised harmonic co-clustering
Xu et al., 2013 [126]	Rat	ND	Brain tissue perturbed by the insertion of a recording device	ND	Automatic tracing, extraction of 131 features, clustering algorithm based on Pearson's correlation, k-NNG structural similarity analysis
Kongsui et al., 2014 [127]	Rat	Prefrontal cortex	Naive	ND	Neurolucida digital reconstruction of cells, extraction of features, fractal analysis and Sholl analysis
Del Mar Fernández-Arjona et al., 2017 [128]	Rat	Septofimbrial nucleus, hippocampus and hypothalamus	Neuroinflammation	ND	Fiji based extraction of 15 features, hierarchical clustering, principal component analysis
Ding at al., 2017 [129]	APPswe/PS1dE9 mouse model of AD	Hippocampus	LPS	females	Automatic segmentation, multifractal analysis and SVM based classification
Healy et al., 2018 [130]	Rat	Cerebellum	ND	ND	Comparison of threshold-based segmentation algorithms
Salamanca et al., 2019 [131]	CRND8Tg AD mouse model and human samples from patients with dementia	Hippocampus	Dementia	ND	MIC-MAC based automatic extraction of 62 features, PCA and k-mean clustering
Leyh et al., 2021 [132]	Mouse	Hippocampus and cortex	Ischemia	ND	Segmentation and machine learning-based classification
Ash et al., 2021 [133]	I307N *Rho* and Balb/c TLR2−/− mouse models	Retina	Degeneration	ND	Automatic segmentation, feature selection, Chi^2 and principal component analysis
Clarke et al., 2021 [134]	Mouse	Visual cortex	LPS or high-fat diet	ND	Segmentation, extraction of 62 features to extract inflammation index and PCA

Silburt and Aubert, 2021 [135]	TgCRND8 mice	Hippocampus	BBB permeabilization	ND	MORPHIOUS definition of microglial clusters, based on one-class support vector machine
Choi et al., 2022 [136]	Mouse	Retina	Ageing mice	ND	Segmentation and SVM based classification of morphologies

Tab. 2. Overview of published papers focusing on microglial morphology. ND = not determined; SVM = Support vector machine; LPS = Lipopolysaccharide.

1.5.2 Extraction of morphological features

Image segmentation is a widely applied technique in the analysis of biological data. It consists in discriminating individual objects such as cells from the background and splitting them from the image. This reduces image complexity and therefore computational needs (**Fig. 6**). Segmentation became one of the most exploited approaches for extracting morphological information, and has therefore been widely used in the field of microglia [123,124,126,137].

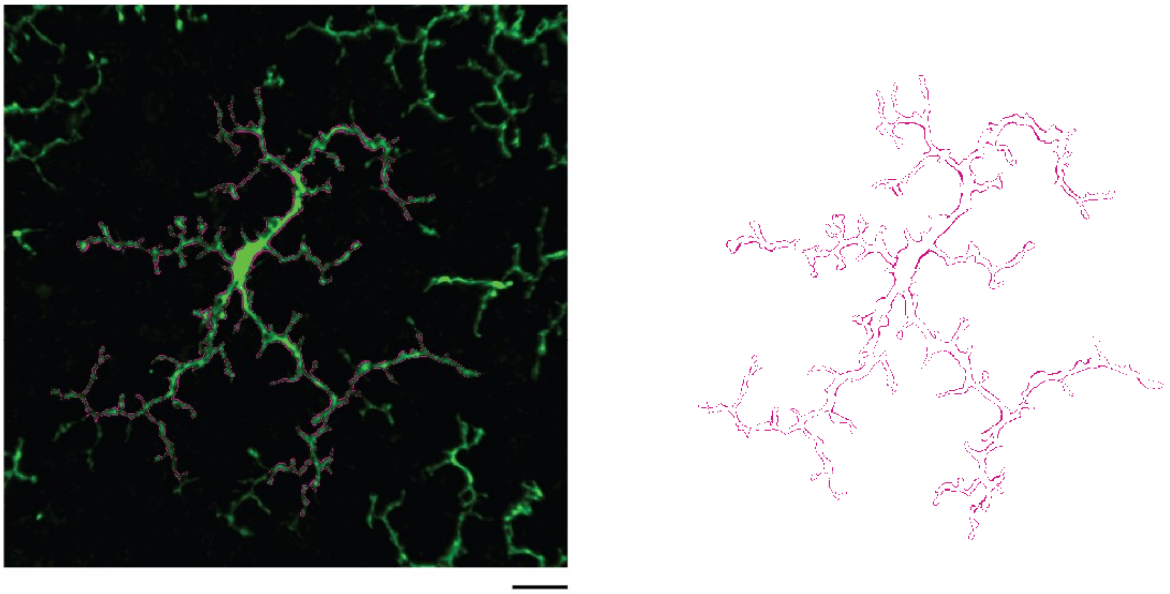

Fig. 6. Image segmentation. Example of segmentation (left) applied to a confocal image of microglia (right). Scale bar: 20 µm.

Salamanca and colleagues applied 3D-automated segmentation and developed MIC-MAC with which they extracted 62 different morphological microglial features and classified microglia into 10 sub-groups of microglia based on their morphology[131]. A major drawback of segmentation is that it heavily relies on thresholding [130]. To avoid user-selected single threshold approach, automatic multi-threshold algorithms have been implemented. Using this approach after exposure to lipopolysaccharides (LPS) *in vivo,* it was possible to distinguish resting *versus* activated populations of microglia comparably to traditional immunohistochemistry methods [123].

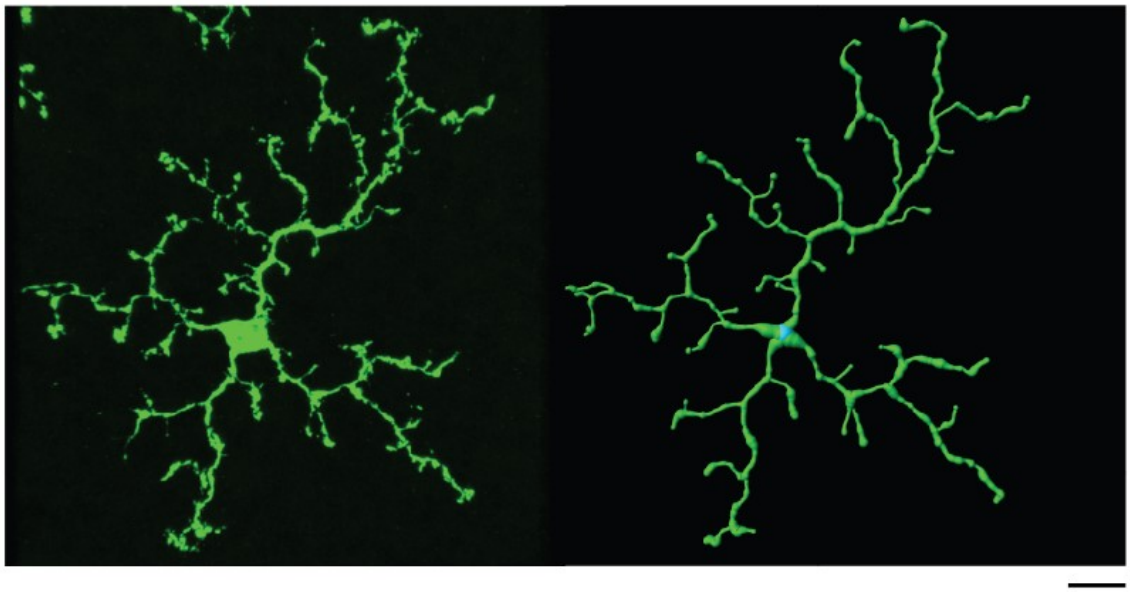

Fig. 7. Cell tracing. Confocal image of a microglial cell (left) and corresponding skeleton reconstruction (right). Scale bar: 10µm.

Thus, an alternative strategy to segmentation is the reconstruction of cell processes (**Fig. 7**). First, the cellular processes are traced in either 2D- or 3D. From this skeleton, parameters such as number of processes, their length, or branching points can be extracted. Besides being the first step for Sholl analysis (see chapter: Sholl analysis), it also provides the basis for novel analytic approaches. Kanari *et al.* [138] developed a topological morphology descriptor (TMD) to exploit persistent homology to classify cortical neurons.

Segmentation and tracing approaches both facilitate the simultaneous extraction of multiple morphometrics and the production of high dimensional data, which makes it difficult to visually interpret the data. To overcome this challenge, dimensionality reduction techniques are often exploited to allow a better interpretation of the data together with non-supervised clustering [131,133,139]. However, also dimensionality reduction techniques such as PCA, t-SNE and UMAP are not equivalent. They might produce different results and their choice should be cautiously based on the nature of the data [130].

1.5.3 Sholl analysis

One of the most widely used tools to estimate microglial complexity is Sholl analysis. This strategy is commonly applied on neurons to predict dendritic arbor complexity [121], which is quantified by the number of intersection between cell processes and a series of concentric

spheres centered on the soma. Thus, Sholl analysis does not rely on scalar comparisons but rather on relational measures. The obtained process distribution can then be compared across conditions (**Fig. 8**). However, Sholl is limited in resolving smaller adaptations, so it failed in identifying phenotypic differences in microglial morphology in rat prefrontal cortex [127]. Moreover, this approach is severely affected by the choice of parameters like the step size of the concentric spheres.

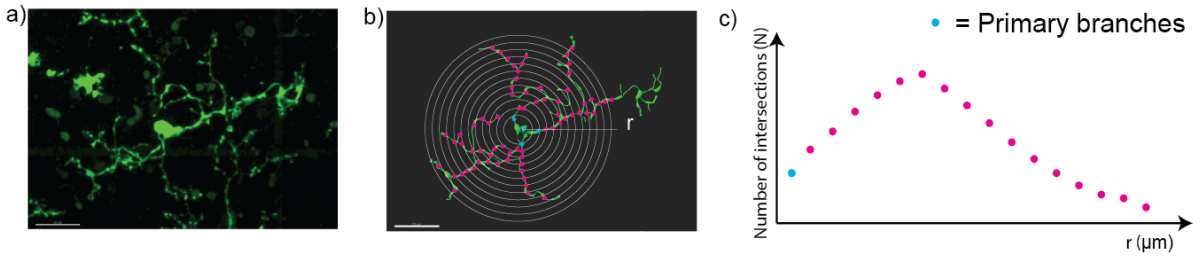

Fig. 8. Sholl analysis. Example of linear Sholl analysis to estimate cell complexity. (a) Confocal image of microglia in the retina of Cx3cr1-GFP$^{+/-}$. Scale bar 20 µm. (b) A 3D-traced microglia is virtually included in a series of concentric spheres and the number of intersection between the skeleton and each sphere is quantified and plotted (c) as a function of the distance from the soma.

1.6 Multidisciplinary approaches for morphological classification

In the last few years, multi-disciplinary approaches were implemented to extract morphological information of microglia. Scorcioni *et al.* developed L-Measure (LM), a free software to quantitatively characterize and classify neuronal morphology [140]. LM is based on the automatized extraction of metric functions like process length, angles, or volume and returns simple statistics, histogram distributions, and a measure of feature interdependency. Lu and colleagues applied LM to classify microglia following brain tissue perturbation due to the implant of an electrical probe [125]. They identified 4 groups of microglia based on their morphology, indicative of their activation state, and compared their distribution in unperturbed and perturbed brain.

A different angle for the classification of microglial morphology is provided by machine learning algorithm. Recently, machine-learning strategies have been further explored to categorize microglia morphologies. Machine learning is a subset of artificial intelligence (AI) that provides computers with the ability to learn specific tasks like image classification without being explicitly programmed to do so. Two major forms of machine learning exists: supervised

and unsupervised, depending on whether labelled input data is used to train the algorithm or not, respectively [141]. Support vector machine (SVM) is a widely used supervised machine-learning algorithm in image classification that enables binary linear classification. SVM was implemented to classify microglia based on multi-fractal analysis of their morphology in mouse models of Alzheimer's disease [129]. Based on this algorithm, microglia were classified in four activation states such as ramified, partially ramified, slightly ramified and activated. Another SVM application applied on microglial morphology discriminated activated and non-activated morphology [136], as well as classification in more than two classes of microglia following ischemic injury [132]. MORPHIOUS is an unsupervised one-class SVM, which was able to discriminate between activated and non-activated microglia based the solely discrimination from the baseline morphology [135]. However, all these strategies have in common that they rely on the choice of morphometrics and are not able to distinguish subtle differences.

1.6.1 Morphology analysis *caveats*: the feature selection bias and a priori classification

All morphological analysis require a reduction of the morphological complexity, which might cause information loss. Therefore, every feature selection, even though widely used, introduces biases that deeply affect the outcomes of the morphology analysis. Moreover, the relevance of some feature depends on the cell to analyze. As an example, parameters such as spine length are a good predictor for neuronal electrical properties, but are not relevant in microglia. Moreover, if the chosen parameters are interdependent, their redundancy might influence the classification.

Thus, the choice of different sets of morphological features deeply influences the outcome, and it is subjective to users, and the same group of objects can be classified in different ways based on different parameter or a combination of them (**Fig. 9**). In contrast to neurons, microglia are not static cells but rather dynamic. They continuously protrude and retract their processes [112]. This introduces variability in their morphology and makes it extremely challenging to dissect subtle adaptations beyond the extreme ends of a morphological spectrum. For example, we have shown that microglia respond to repeated ketamine exposure by removing perineuronal nets (PNN) from the extracellular space [117]. When we looked at the microglial morphology with morphometric extraction, we could not detect any morphological response and even so, this microglia interference reinstated juvenile-like plasticity.

Current strategies frequently bin microglia into *a priori* morphological categories [122,129]. However, this biases the readout and limits our knowledge of morphological diversity. Although classification successfully extracts microglial morphological information in extreme conditions such as degeneration and injuries, we are underestimating the range of microglial morphological states.

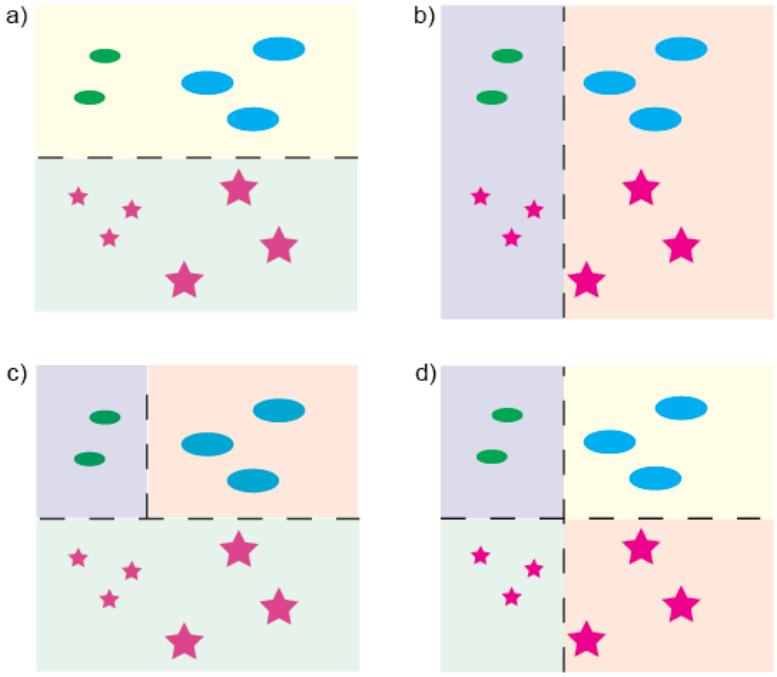

Fig. 9. Feature selection bias. Schematic simplifying the loss of information linked to the selection of one or few morphometric features. The classification of the same set of objects is deeply influenced by the choice of the feature that leads the classification. The set can be classified on shape (a), on size (b), on color (c), or on a combination of features like shape and size (d).

In summary, many different approaches have been developed to investigate microglial morphology. However, they all rely on feature extraction and often classify microglia into predefined morphological classes, which underestimates their wide morphological spectrum. Therefore, we still miss a reliable tool to analyze microglial morphology minimizing the feature selection-dependent information loss and avoiding and a priori classification of microglia.

2 MorphOMICs unravels region- and sex- specific microglia across seven brain regions

2.1 Context

Microglia are highly influenced by environment and responds morphologically. Strategies to characterize these changes are based on user-selected morphometric features, which causes information loss and therefore underestimate the spectrum of context-dependent morphological responses. To fill the gap, we develop MorphOMICs, a topological data analysis approach, which enables semi-automatic mapping of microglial morphology into an atlas of cue-dependent phenotypes and overcomes feature-selection biases and biological variability.

This study was performed in collaboration with Prof. Kathrine Hess and Dr. Lida Kanari from EPFL Lausanne, who previously developed the TMD algorithm and applied it to classify rat cortical neurons [142]. To apply it on microglia, I created a comprehensive library of microglia cells coming from brains, which I collected at different ages, sex and degeneration time points after selecting seven representative brain regions. I performed immunofluorescent staining and acquired confocal images, followed by image preprocessing and analysis. With Imaris software I determined cell density, microglia-CD68 co-localization, and built the skeletons of over 40.000 cells. Together with Dr. Cubero, we derived TMD persistence images for microglia in every brain region and adopted a bootstrap approach to reduce their variability. I assisted Dr. Cubero in the computation of dimensionality reductions, while he mostly performed the computational validation of the algorithm and the optimization of parameters such as the bootstrapping size. I joined multiple discussions with Dr. Scolamiero, Dr. Agerberg and Dr. Chachólski for the stable-ranks base stable vector machine-based application to classify microglia and contributed to the biological interpretation of the data.

2.2 Introduction

The morphological characterization of neuronal shapes has provided important insights into the diversity of cell types related to their genetic and functional features [143]. Numerous studies have tried to apply a similar morphological analysis on microglia [127,144,145]. Although they have revealed microglial heterogeneity [71,116,146], no study has established a high-throughput, minimally biased, and consistent way to capture context-specific and sex-dependent changes in microglial morphology during development and degeneration. Detecting subtle changes in the microglial morphology along the spectrum would offer an early readout of their immediate responses to local environmental cues [116], as microglia are sensitive to changes in neuronal activity [117,147,148]. Moreover, the majority of these analyses rely on restricted microglia sample sizes underestimating their full morphological spectrum.

Microglia morphological phenotype is commonly determined with user-selected features from a three-dimensional (3D) reconstructed branching tree: these features can include total process length, branch number, or number of terminal points. These scalar morphometric descriptors are then statistically compared across conditions. The drawback of this approach is the number and the type of selected features, which biases the biological readout: while too few selected features underrepresent a phenotypic difference, too many cause overfitting and introduce noise [149]. Moreover, in contrast to neuronal morphological trees that are static on the gross structure, microglia processes are highly dynamic [112,113] as they constantly survey their local environment [113]. This introduces considerable intrinsic variability within the traced microglia population of a defined condition as well as the risk of selection bias to the extreme phenotypes. Establishing a reliable brain-region-specific morphological phenotype is critical for characterizing baseline morphology and tracking changes as deviations from the baseline.

To capture morphological phenotypes, complex morphological trees must be simplified with minimal information loss, retaining as many features as possible. Applied topology provides new strategies for solving this problem, as it focuses on the shape properties of geometric objects without the need of morphometrics [138,150]. In particular, the topological morphology descriptor (TMD), which assigns a barcode to any three-dimensional tree, has been successfully applied for classification of cortical neuron morphologies [138]. When we first applied the TMD to ~10,000 3D-traced microglia across the rostro-caudal axis of seven selected adult brain regions, the data indicated a regional phenotype, but the diversity of the individual microglia obscured any well-defined separation.

Here, we developed our MorphOMICs pipeline to overcome the major limitations of feature-selection-based analysis and biological data variability. MorphOMICs combines TMD with bootstrapping, dimensionality reduction, and data visualization techniques, enabling minimally-biased identification of the baseline phenotype. When we applied this strategy, we found that the morphologies of adult microglia vary between brain regions and are different between sexes. This microglial sexual dimorphism gradually diminished along postnatal development. In contrast, the sex-specific phenotype diverged during neurodegenerative disease progression, where females differ in their context-dependent response from males. When we aligned the trajectories of development and degeneration, we obtained for each brain region a morphological spectrum that we used as a reference atlas to map novel conditions. Remarkably, we resolved morphological changes after repeated exposure to the anesthetic cocktail Ketamine-Xylazine-Acepromazine (KXA) and revealed that microglial morphology revert away from the control during the recovery process. By unraveling a spectrum of phenotypes, MorphOMICs overcomes the dichotomized view of microglial morphology and lays out an avenue towards a multimodal definition of the microglia state.

3 Material and methods

Experiments/Analysis performed by researchers other than Gloria Colombo are indicated.

Animals. C57BL/6J (Cat#000664) and B6.129P-Cx3cr1tm1Litt/J (Cat#005582, named here $Cx3cr1^{GFP/-}$, only heterozygous were used) were purchased from The Jackson Laboratories. All animals were housed in the ISTA Preclinical Facility, with 12 hours light-dark cycle, food and water provided ad libitum. Animal from both sexes were used, as indicated in the results. The number of animals used for each condition is detailed in **Supplementary Table 5**. All animal procedures are approved by the Bundesministerium für Wissenschaft, Forschung und Wirtschaft (bmwfw) Tierversuchsgesetz 2012, BGBI. I Nr. 114/2012, idF BGBI. I Nr. 31/2018 under the numbers 66.018/0005-WF/V/3b/2016, 66.018/0010-WF/V/3b/2017, 66.018/0025-WF/V/3b/2017, 66.018/0001_V/3b/2019, 2020-0.272.234.

5xFAD and CK-p25 mice were obtained from the Tsai lab at MIT. All animal work was approved by the Committee for Animal Care of the Division of Comparative Medicine at the Massachusetts Institute of Technology. 5xFAD mice (B6SJL-Tg(APPSwFlLon,PSEN1*M146L*L286V)6799Vas/Mmjax, Stock No: 34840-JAX) were

obtained from Jackson laboratory. CK-p25 mice [151,152,153] were generated by breeding CaMKIIα promoter-tTA mice (CK controls) (B6;CBA-Tg(Camk2a-tTA)1Mmay/J, Jackson Laboratory, Stock No: 003010) with tetO-CDK5R1/GFP mice (C57BL/6-Tg(tetO-CDK5R1/GFP)337Lht/J, Jackson Laboratory, Stock No: 005706). CK-p25 mice were conceived and raised in the presence of doxycycline-containing food to repress p25 transgene expression. To induce p25 transgene expression, mice were fed a normal rodent diet. P25 transgene expression was induced in adult mice at the age of 3 months. For MorphOMICs, we compared CK-p25 brains upon drug withdrawal with our reference C57BL/6J adult microglia population. As a note, doxycycline withdrawal might affect the gut microbiome [154] that can influence on the microglia population in the brain and could cause some variability.
Mice were housed in groups of three to five on a standard 12 h light/12 h dark cycle, and all experiments were performed during the light cycle. Food and water were provided ad libitum.

Brain samples and analyzed brain regions. We analyzed brains of both sexes from C57BL/6J adult mice (8-12 weeks); exposed to 1×, 2× or 3×KXA (100 mg/kg ketamine, MSD Animal Health, Cat #A137A01; 10 mg/kg xylazine, AniMedica, Cat#7630517; 3 mg/kg acepromazine, VANA GmbH, Cat#18F211) and recovered 3-days, 1-week, 2-weeks after 3×KXA [117,155]; Cx3cr1$^{GFP/-}$ mice at postnatal time points P7, P15, P21; 5xFAD mice after 3 and 6 months; and CK-p25 mice 1, 2, and 6 weeks after doxycycline withdrawal. We focused on the following brain regions: the glomerular layer of the olfactory bulb (OB), cortical layer III-V of the frontal cortex (FC) and the primary somatosensory cortex (S1), the dentate gyrus of the hippocampus (DG), the substantia nigra (SN), the cochlear nucleus (CN), and the third lobe of the cerebellum (CB). The sagittal view of the brain sections analyzed (**Fig. 18A, 21A, 26, 31**) was taken from the Allen Developing Mouse Brain Atlas-Sagittal atlas and modified to show brain regions-of-interest [156].

Ovariectomy. Adolescent C57BL/6J females at P20 were anesthetized with 5% isoflurane in 0.5 l/min O_2 during the anesthesia induction and 2% isoflurane in 0.5 l/min O_2 during the maintenance phase. Using an electric razor, the fur was shaved to expose the skin over the lumbar spine and the region was sterilized with 70% (v/v) ethanol. A midline incision of approximately 1 cm was made on the skin in the lower back, below the chest. The subcutaneous tissue was gently dissected to expose the muscular fascia, and the ovarian fat-pad was identified under the muscular layer. The peritoneal cavity was cut with a 0.5 cm incision. The Fallopian tube was exposed, and the ovary identified and cut at the level of the oviduct. The blood vessels

were cauterized to prevent bleeding. The remaining part of the Fallopian tube was placed back in the peritoneal cavity, and the muscular fascia was sutured. The same protocol was repeated for the contralateral ovary. At the end, the skin was sutured. The animals received Metamizol (Sanofi Aventis, Cat#Ay005, *s.c.* 200 mg/kg during surgery) and Meloxicam (Boehringer-Ingelheim, Cat#KPOEH3R, *s.c.* 5 mg/kg after surgery every 24 h for 3 consecutive days), *s.c.,* 2 mg/kg after surgery. Animals were sacrificed at P60. Ovariectomy surgeries were performed together with Dr. Alessandro Venturino

Transcardiac perfusion. For histological analysis, animals were quickly anesthetized with isoflurane (Zoetis, Cat#6089373) and secured to the perfusion plate as described previously [117]. In short: animals were initially perfused with 30 ml of phosphate-buffered saline (PBS) with heparin (100 mg/l, Sigma, Cat#H0878), followed by 30 ml of 4% (w/v) paraformaldehyde (PFA, Sigma, Cat#P6148) in PBS using a peristaltic pump (Behr, Cat#PLP 380, speed: 25 rpm). Animals were decapitated, the brain explanted, fixed in 4% (w/v) PFA for 30 minutes and post-fixed in 4% (w/v) PBS overnight (16h). Then the tissues were washed in PBS and stored at 4C with 0.025% (w/v) sodium azide (VWR, Cat#786-299). For cryoprotection, the tissue was transferred to 30% (w/v) sucrose (Sigma, Cat#84097) in PBS and incubated overnight at 4C. To increase antibody permeability, the brain slices were frozen over dry-ice and thawed at room temperature for three cycles.

Vibratome sections. Cryo-protected brain samples were embedded into 3% (w/v) Agarose/PBS to obtain coronal brain sections. The brain was sliced in 100 µm coronal sections on a vibratome (Leica VT 1200S).

Immunofluorescence staining. The brain slices were incubated in blocking solution containing 1% (w/v) bovine serum albumin (Sigma, Cat#A9418), 5% (v/v) Triton X-100 (Sigma, Cat#T8787), 0.5% (w/v) sodium azide (VWR, Cat#786-299), and 10% (v/v) serum (either goat, Millipore, Cat#S26, or donkey, Millipore, Cat#S30) for 1 hour at room temperature on a shaker. Afterwards, the samples were immunostained with primary antibodies diluted in antibody solution containing 1% (w/v) bovine serum albumin, 5% (v/v) triton X-100, 0.5% (v/v) sodium azide, 3% (v/v) goat or donkey serum, and incubated for 48 hours on a shaker at room temperature. The following primary antibodies were used: rat α-CD68 (AbD Serotec, Cat#MCA1957, clone FA-11, Lot 1807, 1:250); goat α-Iba1 (Abcam, ab5076, Lot FR3288145-1, 1:250); rabbit anti-Iba1 (GeneTex, Cat#GTX100042, Lot 41556, 1:750). The slices were then washed 3 times with PBS and incubated protected from light for 2 hours at room

temperature on a shaker, with the secondary antibodies diluted in antibody solution. The secondary antibodies raised in goat or donkey were purchased from Thermo Fisher Scientific (Alexa Fluor 488, Alexa Fluor 568, Alexa Fluor 647, 1:2000). The slices were washed 3 times with PBS. The nuclei were labeled with Hoechst 33342 (Thermo Fisher Scientific, Cat#H3570, 1:5000) diluted in PBS for 15 minutes. The slices were mounted on microscope glass slides (Assistant, Cat#42406020) with coverslips (Menzel-Glaser #0) using an antifade solution [10% (v/v) mowiol (Sigma, Cat#81381), 26% (v/v) glycerol (Sigma, Cat#G7757), 0.2M tris buffer pH 8, 2.5% (w/v) Dabco (Sigma, Cat#D27802)].

Confocal microscopy. Images were acquired with a Zeiss LSM880 upright Airy scan or with a Zeiss LSM700 upright using a Plan-Apochromat 40× oil immersion objective N.A. 1.4. 2 × 2 z-stack tail-images were acquired with a resolution of 1024 × 1024 pixels.

Image processing. Confocal tile images were stitched using the software Imaris Stitcher 9.3.1.v. Then, the confocal images were loaded in Fiji 1.52e (http://imagej.net/Fiji). To remove the background, the rolling ball radius was set to 35 pixels, and images were filtered using a median 3D filter with x, y, z radii set at 3. Image stacks were exported as .tif files, converted to .ims files using the Imaris converter, and imported into Imaris 8.4.2.v. (Bitplane Imaris).

Quantification of CD68 volume within cells. Surface renderings were generated on microglia and CD68 z-stacks using the surface-rendering module of Imaris 9.2.v Surfaces were generated with the surface detail set to 0.2 µm. To determine the CD68 surface within microglia, the surface-surface coloc plugin was used. This analysis was performed on the entire image. The total ratio of CD68 volume within microglial volume (CD68-to-microglial volume) was calculated per image. To compute the CD68 fold change, the total CD68-to-microglial volume from each condition (sex/time-point) was scaled to the CD68-to-microglial volume ratio from the respective controls. CD68 fold change > 1 means an increase in CD68 volume, CD68 < 1 means a decrease in CD68 volume. CD68 fold-change = 1 denotes no change in CD68 volume.

Quantification of microglia density and statistical analysis. The spot-function plugin of Imaris 9.2.v was used to count the number of cells, i.e the soma of iba-1 positive microglia within every confocal image. Microglial cell density was estimated as total number of cells obtained in this way, divided by the size of the imaged sample in mm^2. After testing the normal distribution of the data, sex averages for microglia from each region were compared with two-sided t.test or Kruskall-Wallis test for non parametric data.

Reconstruction of 3D-traced microglia. After filtering and background subtraction, images were imported in Imaris 9.2.v (Bitplane Imaris). Microglial processes were 3D-traced with the filament-tracing plugin. Since the filament-tracing plugin provides a semi-automated reconstruction, this eliminates the need for a user-blind approach for selecting representative microglia. New starting points were detected when the largest diameter was set to 12 µm and with seeding points of 1µm. Disconnected segments were removed with a filtering smoothness of 0.6 µm. After the tracing, we manually removed cells that were sitting at the border of the image and were only partially traced so that these cells would not be analyzed. The generated skeleton images were converted from .ims format (Imaris) to .swc format [157] by first obtaining the 3D positions (x, y, z) and the diameter of each traced microglial process using the ImarisReader toolbox for MATLAB (https://github.com/PeterBeemiller/ImarisReader) and then exporting for format standardization using the NL Morphology Converter (http://neuroland.org). Artifacts from the 3D-reconstructions automatically failed to be converted into .swc format.

Analysis of morphometric features. Classic morphometric features were calculated from the .swc files using the functions Length (for total process length), N_branch (for number of branches), N_bifs (for number of branching points) and N_tips (for number of terminal points) from L-measure [140] (http://cng.gmu.edu:8080/Lm/). Statistical analysis was performed using scipy.stats (v1.6.2) and scikit-posthocs (v0.6.7). These morphometric features were first tested for normality using the Kolmogorov-Smirnov test (scipy.stats.kstest). After determining the non-normal distribution of the features, we performed non-parametric pairwise tests for independence between measurements from two brain regions using the Kruskal-Wallis test (scipy.stats.kruskal). We used Bonferroni-corrected P values, calculated using Dunn's test via scikit_posthocs.posthoc_dunn (**Ext. Data Table 2-3**). These experiments were performed with Dr. Ryan J. Cubero

Sholl analysis. Sholl curves were calculated from the .swc files using the sholl_crossings function of the NeuroM Python toolkit (https://github.com/BlueBrain/NeuroM). In brief, concentric Sholl spheres centered on the soma of a given traced microglia are constructed with a given step size radius. The number of microglial processes that intersect each Sholl sphere are determined. This step is performed for each traced microglia in the data. From this, Sholl curves of a microglial population are then calculated as the average number of intersections across the population. These computations were performed with Dr. Ryan J. Cubero

Topological morphology descriptor (TMD). A topological data analysis algorithm, the TMD, was used to extract topological phenotypes, called persistence barcodes, from 3D morphological structures (https://github.com/BlueBrain/TMD, Kanari et. al., 2018). In brief, the 3D reconstructed microglia is represented as a tree T rooted in its soma. The TMD summarizes this tree by calculating *persistence barcodes*, where each bar represents a persistent microglial process with respect to a filtering function, i.e., the radial distance from the soma. Note that the persistence barcode that the TMD associates with T under this filtering function is invariant under rotations about the root and rigid translations of T in R^3.

Each bar is described by two numbers: the radial distance, d_i, at which a process originates; and the distance, b_i, when it merges with a larger, more persistent process or with the soma. A bar can be equivalently represented as a point (d_i, b_i) in a *persistence diagram*. We could therefore convolve each point in the persistence diagram with a Gaussian kernel and discretize it to generate a matrix of pixel values, encoding the persistence diagram in a vector, called the *persistence image*. These computations were performed with Dr. Ryan J. Cubero.

Average and bootstrapped persistence images. To construct the *average persistence image* of a given condition, all the persistence barcodes of microglia from the same condition are combined before Gaussian convolution and discretization are performed. We also constructed average persistence images by performing first the Gaussian convolution and discretization of individual microglia persistence barcodes before taking the pixel-wise average. This produced qualitatively similar results.

The bootstrapping method subsamples the microglial population within a given condition, thereby introducing variations around the average persistence image. Starting from the population of all microglia from the same condition, called the *starting population* of size n, the persistence barcodes of a pre-defined number of unique microglia, called the *bootstrap size*, are combined to calculate the *bootstrapped persistence image*. We iterate this process a pre-defined number of times, $n_{samples}$, with replacement to obtain the *bootstrap sample*. These computations were performed by Dr. Ryan J. Cubero.

Subtraction images and TMD distance. The subtraction image is the pixel-wise difference between two given persistence images. From the subtraction image, the TMD distance can be computed as the sum of the absolute pixel-wise difference. For stability of the TMD distance,

we refer the reader to Kanari *et al.* [138]. These computations were performed by Dr. Ryan J. Cubero.

Hierarchical clustering. Hierarchical clustering allowed us to find similarities between microglia across several conditions. Hierarchical clustering was done on the basis of the average persistence images. Clusters were then identified hierarchically using the average linkage criterion with the TMD distance metric and was implemented using cluster.hierarchy.linkage from SciPy v1.6.2 (https://www.scipy.org). Dendrograms were generated using cluster.hierarchy.dendrogram to visualize the arrangement of the resulting cluster. These computations were performed by Dr. Ryan J. Cubero.

Dimensionality reduction.

UMAP. A fast, non-linear dimensionality reduction algorithm, UMAP [158] (Uniform Manifold Approximation and Projection), was applied to visualize the high-dimensional pixel space of bootstrapped persistence images using a 2D representation while preserving local and global structures in the bootstrap samples (https://github.com/lmcinnes/umap) [158]. Given a bootstrap sample containing multiple conditions, a TMD distance matrix containing pairwise distances between bootstrapped persistence images in the bootstrap sample is calculated. Principal components are then obtained using a singular value decomposition of the TMD distance matrix. The first 7 principal components, where the elbow in the singular values is located, were used as input to UMAP with n_neighbors = 50, min_dist = 1.0 and spread = 3.0. Note that we have tested for a wide range of parameter values which did not qualitatively change any of the observations we made in the main text (**Fig. 17**).

tSNE. An alternative dimensionality reduction algorithm is tSNE [83] (t-distributed Stochastic Neighbor Embedding, https://github.com/DmitryUlyanov/Multicore-TSNE) which finds a dimensionality-reduced representation where similar points are pulled closer together while dissimilar points are pushed farther apart with high probability. The first 7 principal components were taken as an input to run tSNE with perplexity = 50. These computations were performed by Dr. Ryan J. Cubero.

Pseudotemporal ordering. The concept of morphological phenotypes as encoded in the persistence images can be likened to transcriptional phenotypes in single-cell RNA sequencing studies. Bootstrapped persistence images, which encapsulate morphological phenotypes of microglial populations from similar conditions, are comparable. Furthermore, it is reasonable

to assume that morphological changes in bootstrapped microglial populations from control to disease conditions occur with incremental differences in the persistence images. This conceptual similarity allowed us to use the pseudo-temporal trajectory inference algorithms that are well-used in the single-cell RNA sequencing community to study the morphological progression during microglial development and degeneration. These computations were performed by Dr. Ryan J. Cubero.

Palantir. Palantir [159] uses principles from graph theory and Markov processes to calculate the pseudo-time and the probability of a cell reaching each of the terminal conditions in the sample (https://github.com/dpeerlab/Palantir). First, the principal components of the bootstrapped persistence images were obtained using 25anhatta.utils.run_pca with n_components = 100 and use_hvg = False. The diffusion maps were then calculated from the PCA projections using 25anhatta.utils.run_diffusion_maps with n_components = 10 and knn = 20 which outputs the Palantir pseudo-times. Harmony [160] is then used to construct an augmented affinity matrix from the Palantir pseudo-times to connect together the Palantir pseudo-times and construct a trajectory using a force-directed graph (https://github.com/dpeerlab/Harmony). These computations were performed by Dr. Ryan J. Cubero.

Monocle. To corroborate the Palantir trajectories, an alternative pseudo-temporal trajectory-inference algorithm called Monocle was employed. Monocle [161] uses reverse graph embedding which learns a principal graph which approximates a lower-dimensional manifold to construct a pseudo-time trajectory (https://github.com/cole-trapnell-lab/monocle3)[161]. Similar to Palantir implementation, the principal components of the bootstrapped persistence images were first obtained using preprocess_cds with num_dim = 100. A 2D UMAP representation was then obtained using reduce_dimension with umap.metric = "25anhattan", umap.min_dist = 1.0, and clusters were identified using cluster_cells with cluster_method = 'leiden'. Finally, the pseudo-temporal trajectory was then obtained using learn_graph with use_partition = FALSE and close_loop = FALSE. These computations were performed by Dr. Ryan J. Cubero.

Stable ranks analysis. An alternative representation of the persistence barcodes is through stable ranks [162]. Stable ranks are functional summaries of persistence which depend on pseudometrics to compare persistence barcodes. Given a pseudometric d, the stable rank $\hat{rank}_d(X)(t)$ of a persistence barcode X is a function that assigns to t the number:

$$\hat{rank}_d(X)(t) = min\{rank(Y)|d(Y,X) \leq t\}.$$

Whereby $rank(Y)$ denotes the number of bars of the persistence barcode Y. The stable rank $\hat{rank}_d(X)(t)$ associates to a persistence barcode a non-increasing and piece-wise constant function with values in $[0, \infty)$. An important property is that this mapping is continuous with respect to the chosen pseudometric d and the L_p metric on the space $\mathscr{M}$ of measurable functions.

A class of pseudometrics on persistence barcodes can be constructed from density functions [162], which intuitively are used to vary the weight along the filtration scale parametrizing a barcode. With such pseudometrics, the stable rank is a bar count based on length of bars as scaled by the density. The standard stable rank is defined by a density function with constant value one. In this case, $\hat{rank}_d(X)(t)$ is the number of bars in X with length greater than or equal to t, i.e., all filtration scales are weighted equally.

Stable ranks can be used in place of persistence images in the MorphOMICs pipeline. Similarly, to MorphOMICs, the persistence barcode X of a given microglia is calculated using the TMD algorithm. To obtain *bootstrapped standard stable ranks*, we combined the persistence barcodes of a pre-defined number of microglia and computed their standard stable ranks. Dimensionality reduction was then implemented similar to the methods above (see **Methods: *Dimensionality reduction***). These computations were performed by Dr. Ryan J. Cubero, Dr. Martina Scolamiero and Jens Agerberg.

Classification accuracy using stable ranks. To support and quantify the impact of bootstrapping on the regional segregation visualized in the reduced UMAP space (**Fig. 17**), we performed a classification task for microglia morphologies represented by their standard stable rank and labeled by brain region. We used a support vector machine (SVM) with a specific kernel based on stable ranks [163] for the classification. For persistence barcodes X and Y, the stable rank kernel with respect to a pseudometric d is given by

$$K_d(X,Y) := \int_0^\infty \hat{rank}_d(X)(t)\hat{rank}_d(Y)(t)dt.$$

Where we used the pseudometric induced by the constant function with value one.

We performed pairwise classifications. For each pair of brain regions, we constructed a dataset consisting of 400 bootstrap samples, i.e., 200 from each region and bootstrap sizes of either 10, 20 or 50 (the results are reported separately for these three values). We randomly partition the

dataset for cross-validation wherein 240 samples were used for SVM training (training set) and 160 samples for validation (test set). We report the average accuracy over 10 repeated cross-validations on the test set. The SVM was trained using the implementation in the Python library sklearn (https://scikit-learn.org/stable/) with default settings except for the usage of the stable rank kernel. These computations were performed by Dr. Martina Scolamiero and Jens Agerberg.

Bootstrapped morphometric features and bootstrapped Sholl curves. To understand whether classical morphology analysis pipelines are able to recapitulate the microglial dynamics recovered by MorphOMICs, a similar bootstrapping analysis was also done where we pooled together a pre-defined number of microglia. Each morphometric quantity in the extended list enumerated in **Ext. Data Table 4** was then averaged to obtain a 27-D vector, with each dimension corresponds to a morphometric feature, called the *bootstrapped morphometric features*. On the other hand, Sholl curves averaged across the pooled microglia to obtain the *bootstrapped Sholl curves*. Dimensionality reduction was then implemented similar to the methods above (see **Methods: *Dimensionality reduction***). These computations were performed by Dr. Ryan J. Cubero.

Mapping morphologies onto the reference atlas. We have generated a larger reference atlas with $n_{samples}$= 2000 bootstrapped persistence images per condition to construct the Palantir trajectories. Palantir coordinates *(x,y)* were rescaled to [0,1]. We took and filtered the bootstrapped persistence images keeping only the 500 most highly variable pixels across the images in all conditions. We used linear regression, one for each axis, to learn the mapping from the filtered bootstrapped persistence image to the rescaled Palantir coordinates. Given a novel condition, we generated the bootstrapped persistence images and filtered them with the 500 most highly variable pixels identified earlier. We used the trained regression model to infer the locations of each image in the reference atlas. Then, we calculated the mean position denoting the center of the inferred locations and indicated the spread using the standard deviation. These computations were performed by Dr. Ryan J. Cubero.

Statistics and Reproducibility

Each experiment was repeated independently with similar results. **Ext. Data Table 4** provides the numbers of 3D-traces obtained per condition, sex, and brain region. **Ext. Data Table 5** describes the number of animals per condition, their sex, and brain region.

4 Results

4.1 MorphOMICs uncovers adult microglial heterogeneity

To address how morphological phenotypes differ between microglia across brain regions, we immunostained the adult C57BL/6J mouse brain with the allograft inflammatory factor 1 (Aif1/Iba1) [104] for both sexes with at least biological triplicates. Then, we traced 9,997 cells and generated a library of three-dimensional (3D) microglial skeletons from seven brain regions chosen to span the rostro-caudal axis with a preference for regions that are known to be affected in Alzheimer disease [164,165,174–183,166–173]: the olfactory bulb (OB_{mg}), frontal cortex (FC_{mg}), dentate gyrus of the hippocampus (DG_{mg}), primary somatosensory cortex ($S1_{mg}$), substantia nigra (SN_{mg}), cochlear nucleus (CN_{mg}), and cerebellum (CB_{mg}, **Fig. 10**).

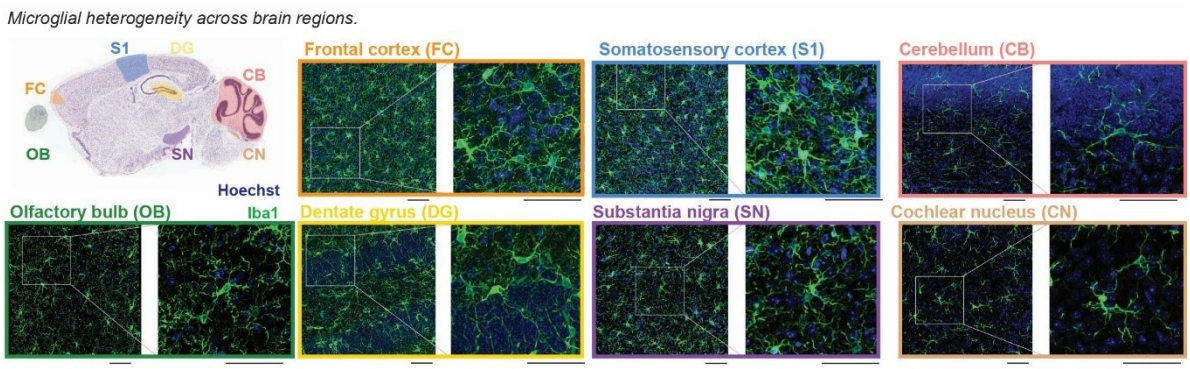

Fig. 10. Microglial morphology in adult healthy brains. Sagittal view of the murine brain (Image credit: Allen Institute) with annotated brain regions: olfactory bulb (OB), frontal cortex (FC), dentate gyrus (DG), somatosensory cortex (S1), substantia nigra (SN), cochlear nucleus (CN), and cerebellum (CB). Next, confocal images of immunostained microglia (Iba1, green) and cell nuclei (Hoechst, blue) from adult C57BL/6J mice with zoom-in. Scale bar: 50 µm.

When we utilized morphometrics that are commonly used in the field of microglial morphology [123,144,184], we found non-significant differences across these brain regions with the exception of $(CB \text{ and } CN)_{mg}$ (**Fig. 11**).

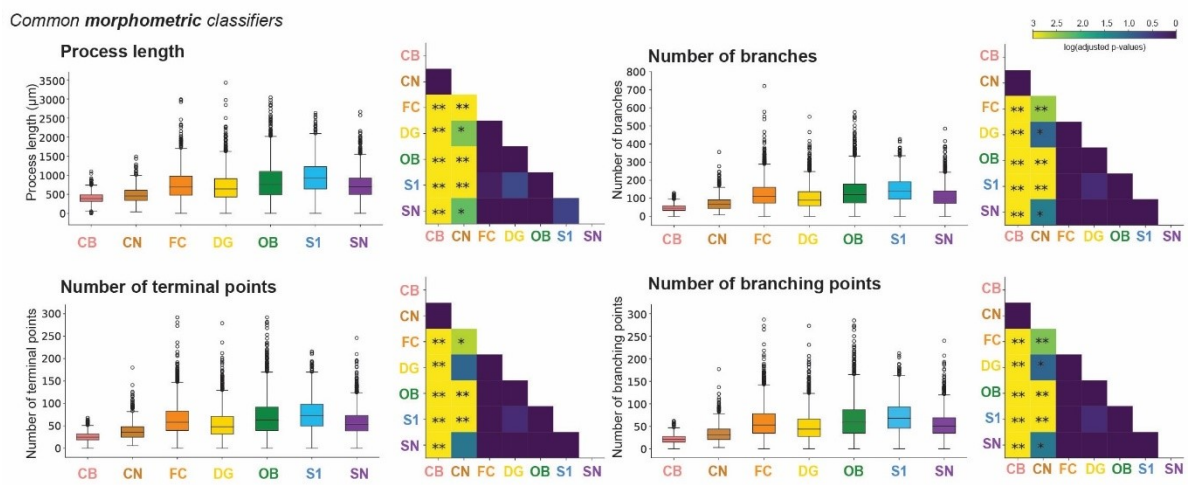

Fig. 11. Classic morphometry analysis of microglial morphology in adult healthy brains. Box plots for the following morphometric features: process length, number of branches, and terminal and branching points for traced adult C57BL/6J microglia across different brain regions color-coded: CB (cerebellum, n=299), CN (cochlear nucleus, n=498), FC (frontal cortex, n=926), DG (dentate gyrus, n=902), OB (olfactory bulb, n=796), S1 (somatosensory cortex, n=719), SN (substantia nigra, n=1050) from at least six animals. Next, matrices with color-coded p-values for the pairwise comparison of each morphometric (see also **Ext. Data Table 2**). * $p < 0.05$, ** $p < 0.01$.

We therefore applied the topological morphology descriptor (TMD) [138,150] for which each 3D skeleton was represented as a rooted tree with the microglial soma in the center, processes (edges), branching points (nodes), and process terminals (terminal points, **Fig. 12**, i). The TMD converts the tree as a persistence barcode, where each bar represents the persistent process lifetime in terms of the radial distance from the soma (**Fig. 12**, ii) [138,149]. Every bar is then collapsed into a single point in the persistence diagram summarizing the process's lifetime, which is then converted into a persistence image using Gaussian kernels [185] (**Fig. 12**, iii). The branching complexity is spatially represented by process length proportional to the distance from the diagonal (**Fig. 12**, iv).

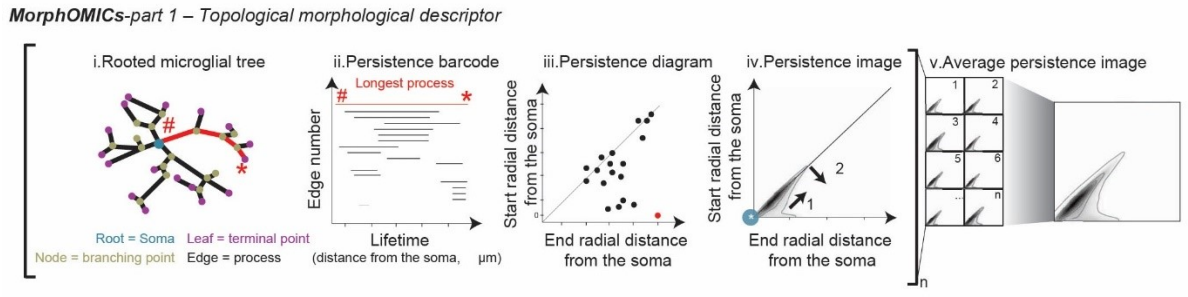

***Fig. 12. TMD approach* C:** Schematic of MorphOMICs pipeline covering topological morphology descriptor (TMD) with a mock microglia skeleton and plots. Red: longest process with start (#) and end (*) as an example. Each traced microglia is converted into a rooted tree (i), and from there into a persistence barcode (ii), a persistence diagram (iii, with each bar collapsed to a point), and a persistence image (iv) with grey-scaled process density in 2D-space. Blue spot: soma location. Arrow 1: distance from the soma. Arrow 2: Length of processes, which increases the further away from the diagonal. Each persistence image (n) is summarized to an average persistence image of a condition.

An example of this conversion with a representative microglial morphology is shown in **Fig. 13.**

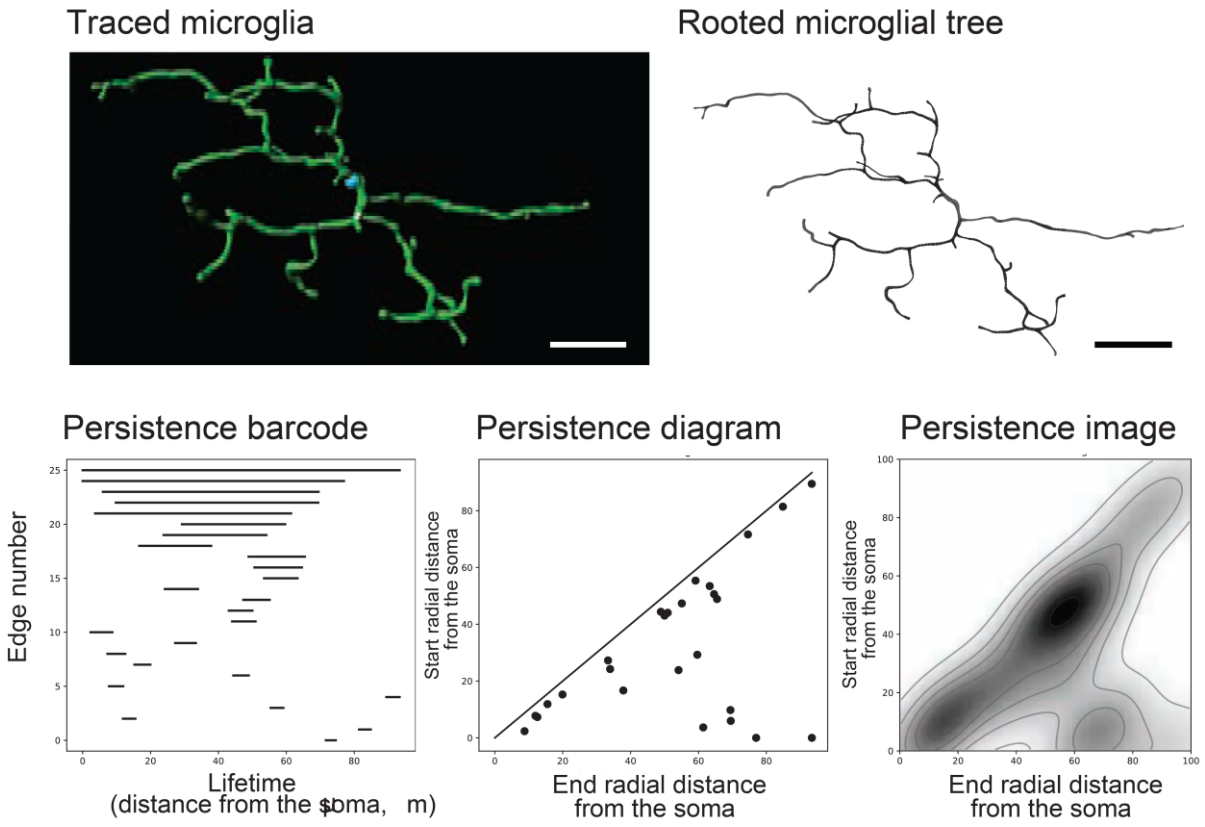

Fig. 13. ***Example of a 3D-traced microglia and its conversion to a persistence image.*** Top: left, Imaris-traced skeleton of a microglia. Scale bar: 10µm. Right, formatted rooted microglia tree, which is used for the persistence plots. Bottom: persistence barcode (left), persistence diagram (middle), and persistence image (right) exactly matching the rooted tree. Number of animals: see Supplementary Table 5. Points situated close in the UMAP space indicate similar bootstrapped persistence image however, the point's actual position is irrelevant.

To quantify the differences between microglial morphologies across brain regions, we computed the pairwise TMD distance between the average persistence images [138]. While average persistence images did not differ strongly (**Fig. 14A**), hierarchical clustering suggested groups with $(FC, OB, SN)_{mg}$ and $(S1, DG)_{mg}$ with CN_{mg} and CB_{mg} segregated (**Fig. 14B**).

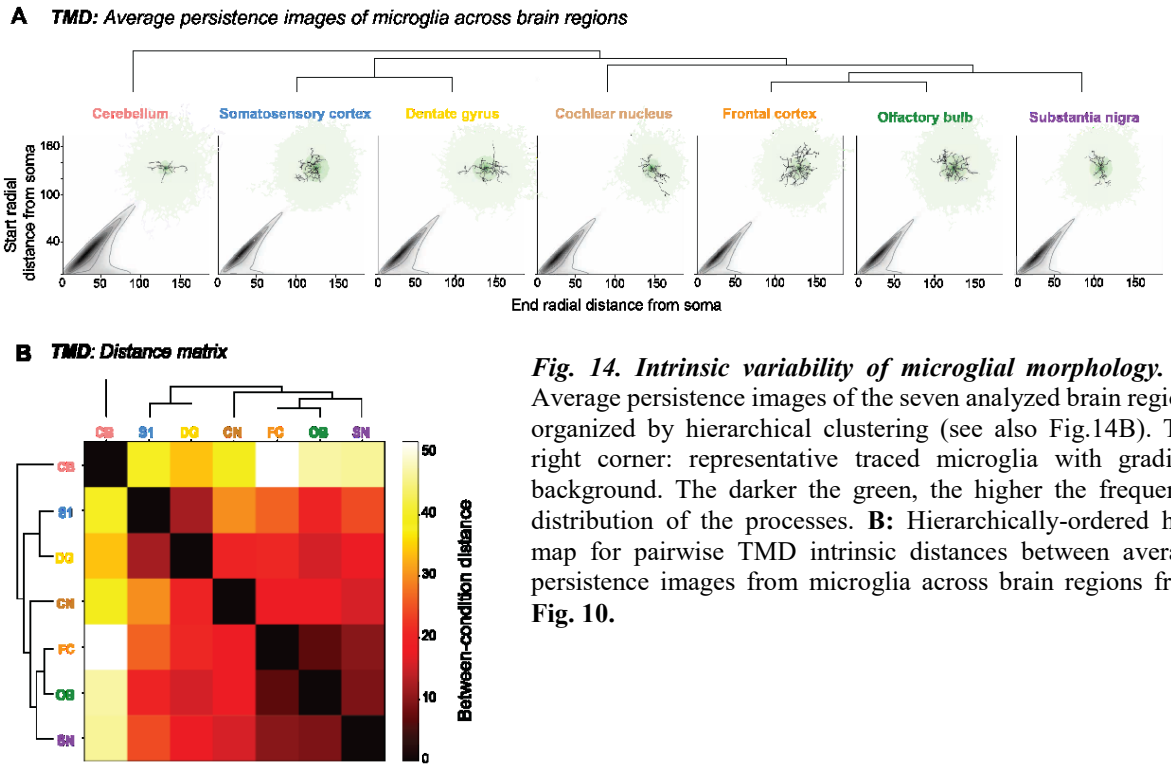

Fig. 14. Intrinsic variability of microglial morphology. **A:** Average persistence images of the seven analyzed brain regions organized by hierarchical clustering (see also Fig.14B). Top right corner: representative traced microglia with gradient background. The darker the green, the higher the frequency distribution of the processes. **B:** Hierarchically-ordered heat map for pairwise TMD intrinsic distances between average persistence images from microglia across brain regions from **Fig. 10.**

When we looked at the individual persistence images, we found a wide variance between the individual microglia within a brain region that made it challenging to distinguish regional phenotypes (**Fig. 15A**). We note that this dispersion is not driven by an animal-based batch effect (**Fig. 15B**).

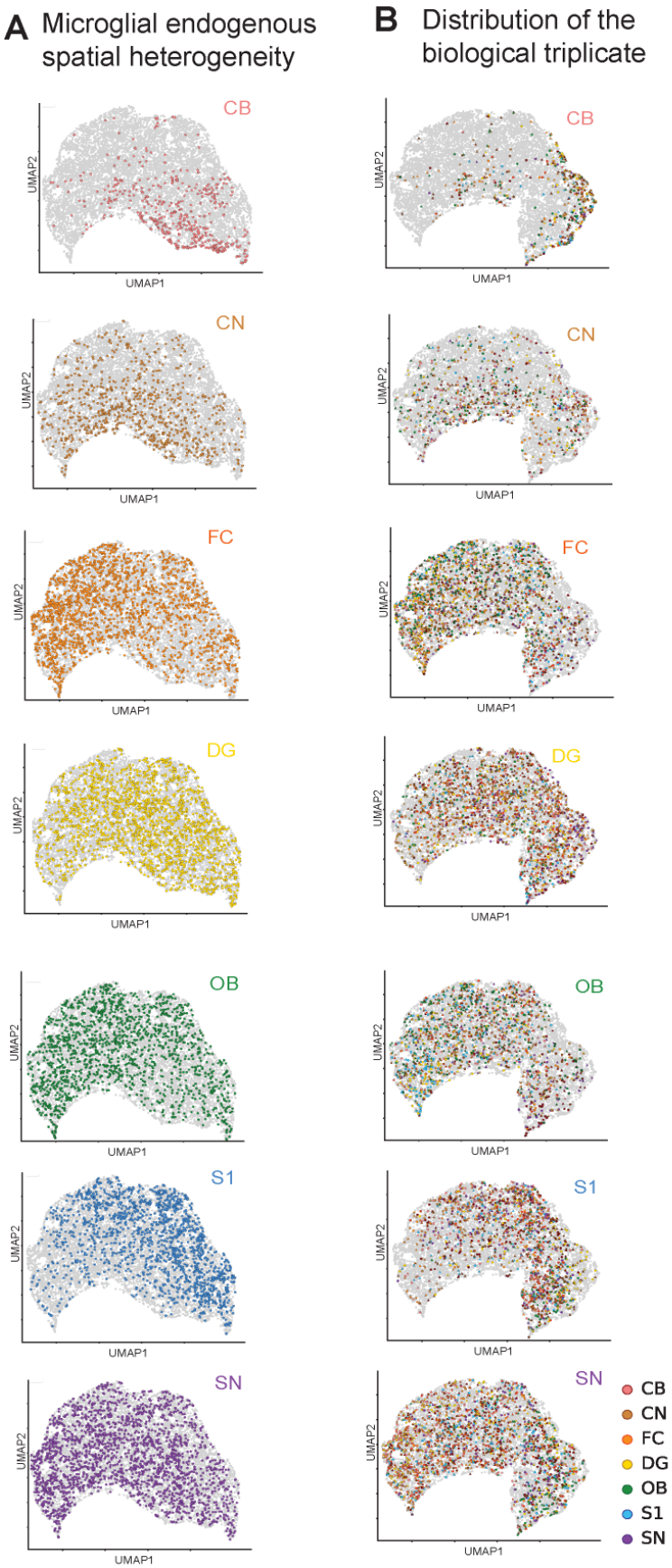

Fig. 15. Microglial variability among regions and animals. **A-B:** UMAP plots of the entire microglial population size (grey) with color-highlighted brain regions (**A**) or animals (**B**). Each dot represents a single persistence image. (**B**) Triangle and circle for females and males, respectively. Each animal is color-coded.

To overcome this intrinsic variability within a microglial population, we developed MorphOMICs, which combines TMD with subsampling of persistence images, dimensionality reduction, and data visualization strategies. Bootstrapping randomly draws, without replacement, a user-defined number of unique persistence images (x) from a microglial population pool (n) and iteratively generates bootstrapped persistence images (**Fig. 16A**). To display these bootstrapped persistence images for each brain region, we applied the nonlinear dimensionality reduction technique UMAP (Uniform Manifold Approximation and Projection, **Fig. 16B**), which converts the high-dimensional persistence images into a reduced 2D representation while preserving their global structure [158].

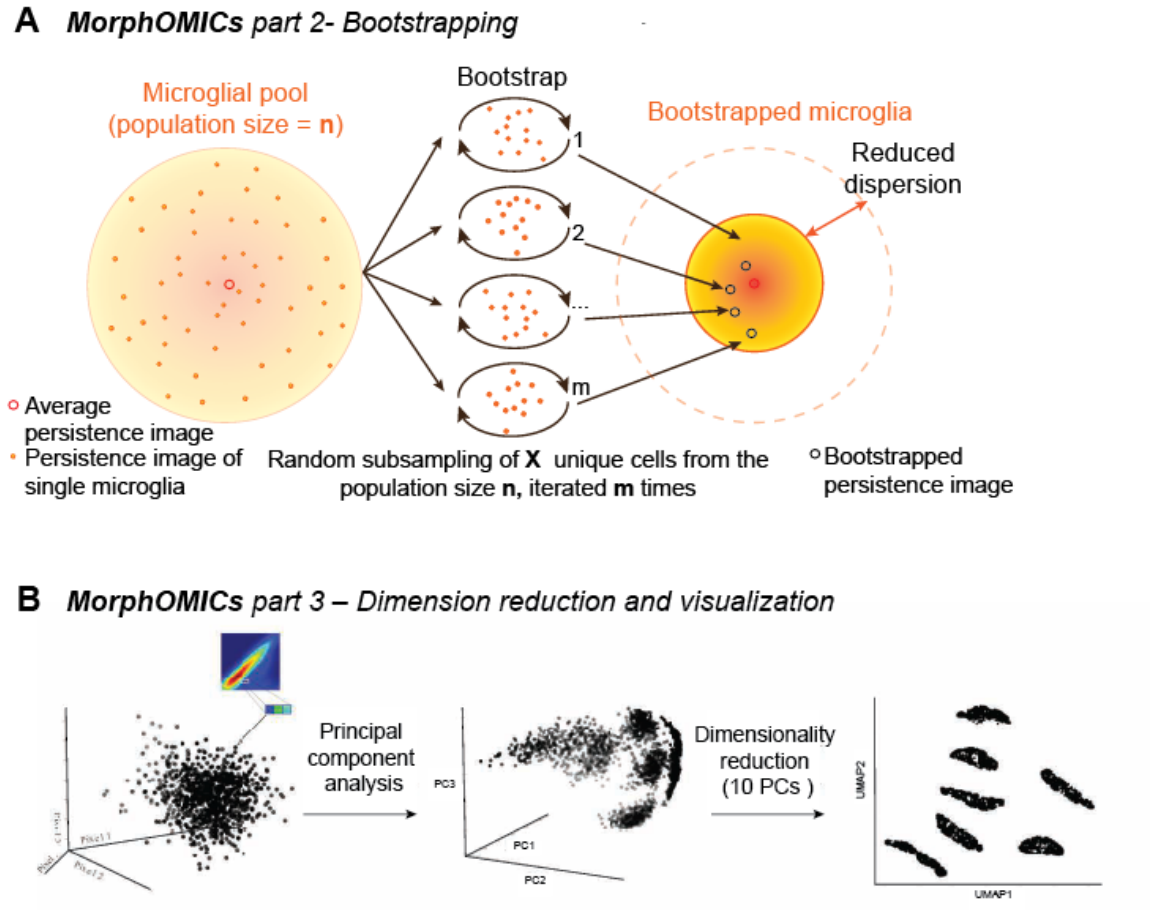

Fig. 16. MorphOMICs approach and intrinsic variability of microglial morphology. **A:** Schematic of MorphOMICs pipeline covering dimension reduction and data visualization with Uniform Manifold Approximation and Projection (UMAP). Left: each persistence image is pixelated, and each pixel represents a dimension. Middle: reducing dimensions with principal component (PC) analysis. Right: further dimensionality reduction based on the first ten PCs. **B:** UMAP plot of MorphOMICs-analyzed adult microglia, color-coded for each brain region. Each dot represents a bootstrapped persistence image. Data for each brain region from at least six animals, both sexes together. Note that points situated close in the UMAP space indicate similar bootstrapped persistence image however, the point's actual position is irrelevant.

While local distances are presumably better preserved in UMAP compared to tSNE [186], the point's actual position in the reduced space is irrelevant. After controlling for the bootstrapped to microglial population pool size ratio (**Ext. Data Fig. 1-5**, **Supplementary Text**), we applied MorphOMICs to our 3D-microglia library. The UMAP plot exhibited a spatial separation similar to that of the hierarchical clustering of the average persistence images (**Fig. 14A**), with CB_{mg} separated from the other brain regions and $(FC, OB, SN)_{mg}$ occupying a well-defined area in the UMAP space (**Fig. 17**).

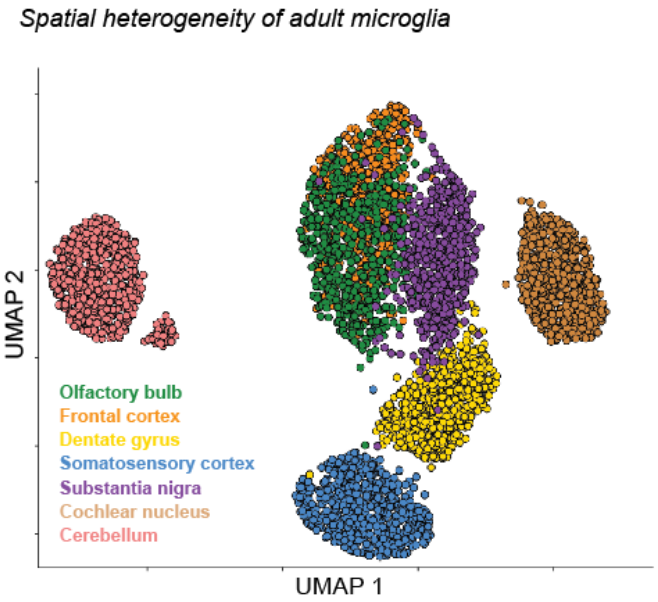

Fig. 17. Microglial heterogeneity in adult brain regions. UMAP plot of MorphOMICs-analyzed adult microglia, color-coded for each brain region. Each dot represents a bootstrapped persistence image. Data for each brain region from at least six animals, both sexes together. Note that points situated close in the UMAP space indicate similar bootstrapped persistence image however, the point's actual position is irrelevant.

However, MorphOMICs further revealed that OB_{mg} and FC_{mg} are intermingled, while DG_{mg} and $S1_{mg}$ formed distinct clusters. Importantly, these cluster segregations were stable even if we changed UMAP's hyperparameters (**Ext. Data Fig. 6A**) or when we applied tSNE visualization instead (**Ext. Data Fig. 6B**). Finally, we also confirmed with stable ranks [162,163] that the persistence barcodes maintained the region-specific phenotypes (**Ext. Data Fig. 6C**). When we applied a support vector machine algorithm to the stable ranks, the resulting classification accuracy confirmed the separation between brain regions in the UMAP space (**Ext. Data Fig. 7A**). As a note, while the position of CN_{mg} varies with the choice of hyperparameters, its relative position to the other brain regions, especially DG_{mg} and SN_{mg} remain consistent. Thus, we suspect that more complex morphological relationships between brain regions can exist as exhibited by CN_{mg}.

An alternative morphological simplification that is commonly performed in the microglia literature is Sholl analysis, which calculates the number of processes that intersect concentric

spheres centered on the soma with a user-defined radius [121]. When we applied Sholl analysis, we could not recapitulate the spatial segregation captured by MorphOMICs (**Ext. Data Fig. 7B**). Even if we applied bootstrapping to Sholl curves, we could only dissect the regional heterogeneity for CB_{mg} and CN_{mg} (**Ext. Data Fig. 7C**). Importantly, the clusters became less distinct by increasing the Sholl step size radius confirming the superiority of our MorphOMICs algorithm. Overall, these data indicate that adult brain regions have well-defined microglia morphological phenotypes, which MorphOMICs reliably uncovers.

4.2 Region-dependent, sexually dimorphic microglial phenotype

Next, we were interested in the extent of microglial sexual dimorphism across brain regions, which is only partially understood [90,187,188]. We applied MorphOMICs to our library, and compared males and females within the UMAP space (**Fig. 18A-B**).

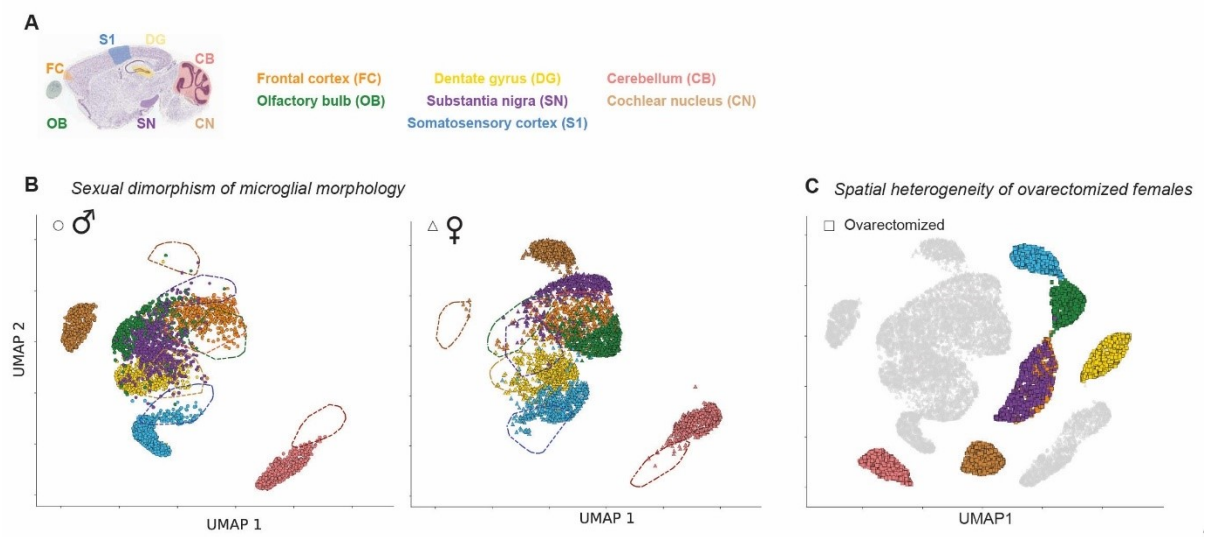

Fig. 18. MorphOMICs identifies sexually-dimorphic microglial morphology in healthy adults, which is influenced by circulating estrogens. **A**: Sagittal view of analyzed brain regions: olfactory bulb (OB), frontal cortex (FC), dentate gyrus (DG), somatosensory cortex (S1), substantia nigra (SN), cochlear nucleus (CN), and cerebellum (CB). **B-C**: MorphOMICs-analyzed microglia in male, female, and ovarectomized adult mice. (**B**) UMAP plot for each brain region color-coded for males (left) or females (right) with dashed lines vice versa as reference. Each dot represents a bootstrapped persistence image. (**C**) UMAP plot of ovarectomized females. Ovariectomized brain regions are highlighted. Grey: the non-ovarectomized counterpart as reference.

As before, each brain region occupied a unique cluster in the plot, where CB_{mg} and CN_{mg} were most divergent. Strikingly, most brain regions separated female and male microglia, with CB_{mg}, CN_{mg}, OB_{mg}, SN_{mg}, and $S1_{mg}$ forming close but spatially separated clusters. In contrast, ♂/♀DG_{mg} and FC_{mg} highly overlapped, suggesting rather minor morphological differences between the sexes. Interestingly, compared to **Fig. 17** the $(FC, OB)_{mg}$ cluster broke up: ♂FC_{mg} and ♂OB_{mg} formed spatially separated clusters, whereas ♀$(FC, OB)_{mg}$ were intermingled.

These morphological differences could depend on the microglia density. When we determined the number of microglia for each brain region and sex, we found that only CN_{mg} and OB_{mg} showed a significant sexual dimorphism (**Fig. 19 A-B**), which is also reflected in the strongest separation within the UMAP space (**Fig. 18 B**). In contrast, microglia density does not explain the sexually-dimorphic signature in CB_{mg} and SN_{mg} suggesting that density does not fully capture the dimorphic phenotype.

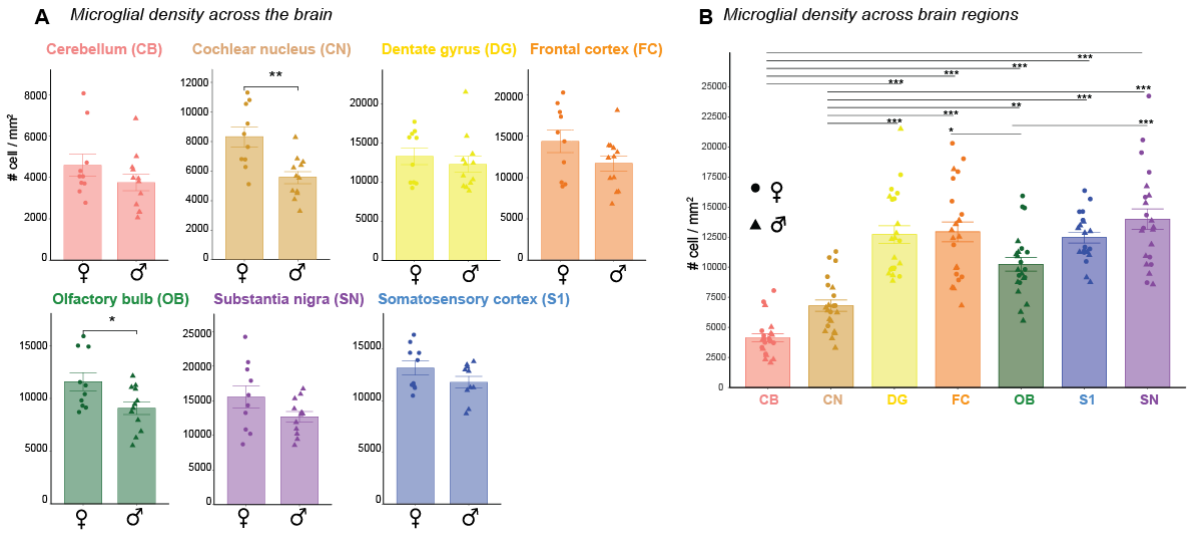

Fig. 19. Microglial densities across brain regions in adult mice. **A-B:** Bar plot of microglial density distribution for each brain regions in C57BL/6J female and male adults. Data are presented as mean number of cells per mm2 ± SD. After determining normal distribution of the features with Shapiro-Wilk test, (**A**) sex averages for microglia from each region were compared with two-sided t-test. Each dot represents one animal. CNmg(n♀= 10, n♂= 12): t = 3.504, df = 15.1, p-value = 0.00312. Obmg(n♀= 10, n♂= 12): t = 2.401, df = 16.864, p-value = 0.0282. CBmg(n♀= 10, n♂= 12): t = 1.2564, df = 17.327, p-value = 0.2257. FCmg(n♀= 10, n♂= 12): t = 1.6236, df = 16.275, p-value = 0.1237. SNmg(n♀= 10, n♂= 12): t = 1.6261, df = 12.901, p-value = 0.1281. DGmg(n♀= 10, n♂= 12): t = 0.68892, df = 19.669, p-value = 0.4989. S1mg(n♀= 10, n♂= 12) t = 1.5618, df = 17.518, p-value = 0.1362. . SD: standard deviation. * $p < 0.05$, ** $p < 0.01$. (**B**) Analysis of variance (ANOVA) on densities yielded significant variation among conditions, $F = 17.98$, $p < .001$. $F = 33.35$, $p < .001$. Tukey post hoc test was computed for pairwise comparisons. (CN-CB)p.adj= 0.0523543; (DG-CB)p.adj= 0.0000000; (FC-CB)p.adj= 0.0000000; (OB-CB)p.adj= 0.0000000; (S1-CB)p.adj= 0.0000000; (SN-CB)p.adj= 0.0000000; (DG-CN)p.adj= 0.0000000; (FC-CN)p.adj= 0.0000000; (OB-CN)p.adj= 0.0036669; (S1-CN)p.adj= 0.0000002; (SN-CN)p.adj= 0.0000000; (FC-DG)p.adj= 0.9999824; (OB-DG)p.adj= 0.0898840; (S1-DG)p.adj= 0.9999557; (SN-DG)p.adj= 0.7953985; (OB-FC)p.adj= 0.0474778; (S1-FC)p.adj= 0.9985099; (SN-FC)p.adj= 0.9051447; (S1-OB)p.adj= 0.1998237; (SN-OB)p.adj= 0.0009832; (SN-S1)p.adj= 0.643197. Each dot represents one animal with symbols for female (circle) and male (triangle). Number of animals per region= 22.

To determine whether this sex-specific phenotypic differences are hormone-dependent, we expanded our library to include microglia from adult female mice that we ovariectomized at P20 (♀$_{ov}$, **Fig. 20**) before they start the estrous cycle and enter puberty [189]. We found that the ♀$_{ov}FC_{mg}$ cluster no longer intermingled with ♀$_{ov}OB_{mg}$ in ovariectomized females but instead

fused with ♀$_{ov}$SN$_{mg}$ (**Fig. 18C**). This is surprising, as in non-ovariectomized mice, ♀SN$_{mg}$ was close to but distinct from the intermingled ♀(FC, OB)$_{mg}$. When we compared non-ovariectomized to ovariectomized females, we found that in the UMAP space ovariectomized females formed distinct clusters, spatially separated from their non-ovariectomized counterparts and did not resemble any hints of masculinization (**Fig. 18B-C**). These results demonstrate the existence of brain-region-specific, sexually dimorphic phenotype, and that interfering with estrogen production before puberty affects microglial heterogeneity in adulthood.

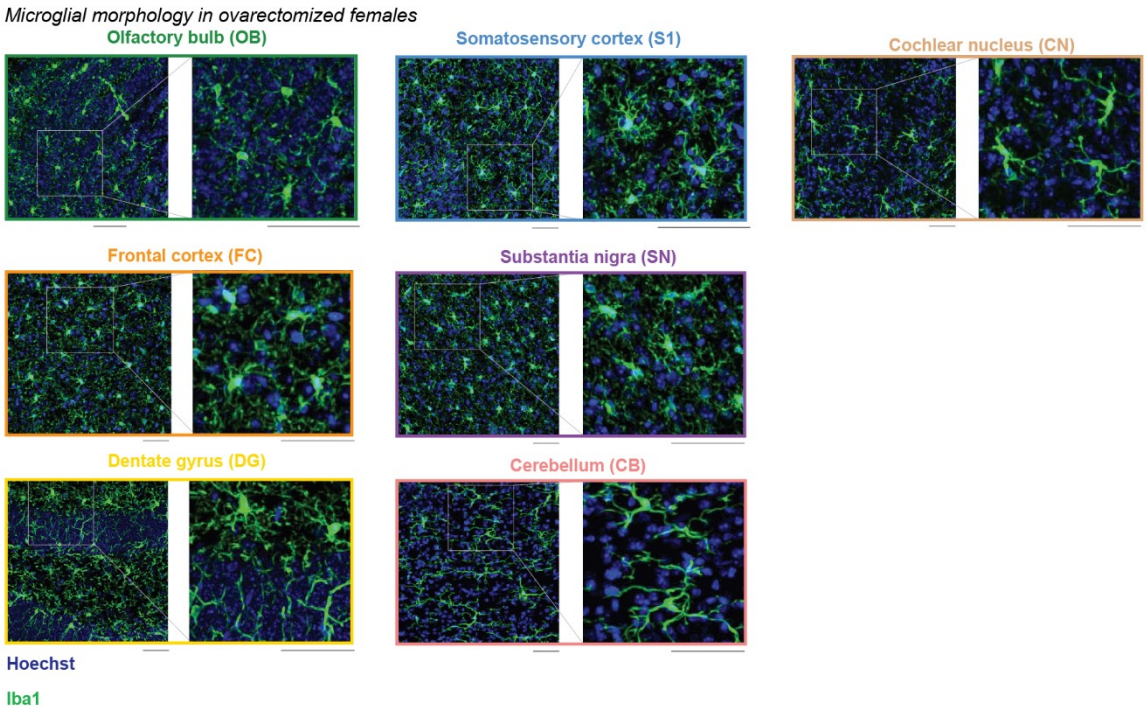

Fig. 20. ***Microglial morphology in ovarectomized females.*** *Confocal images of immunostained microglia (Iba1, green) and cell nuclei (Hoechst, blue) from ovariectomized C57BL/6J adult mice for each brain region with zoom-in. Scale bar: 50 µm. SD: standard deviation.*

4.3 Sexual dimorphism affects microglial morphology during development

Microglia originate in the yolk sac and infiltrate the nervous system early during embryonic development [1]. After microglia occupy a brain region, their morphology gradually becomes more branched during postnatal neuronal circuit refinement (**Fig. 21A**) [190]. To determine whether microglial heterogeneity and dimorphic phenotype already exist within the first postnatal weeks and before the onset of puberty, we sampled microglia from all seven brain regions at postnatal days 7, 15, and 22 and included them into our library (**Fig. 21B**).

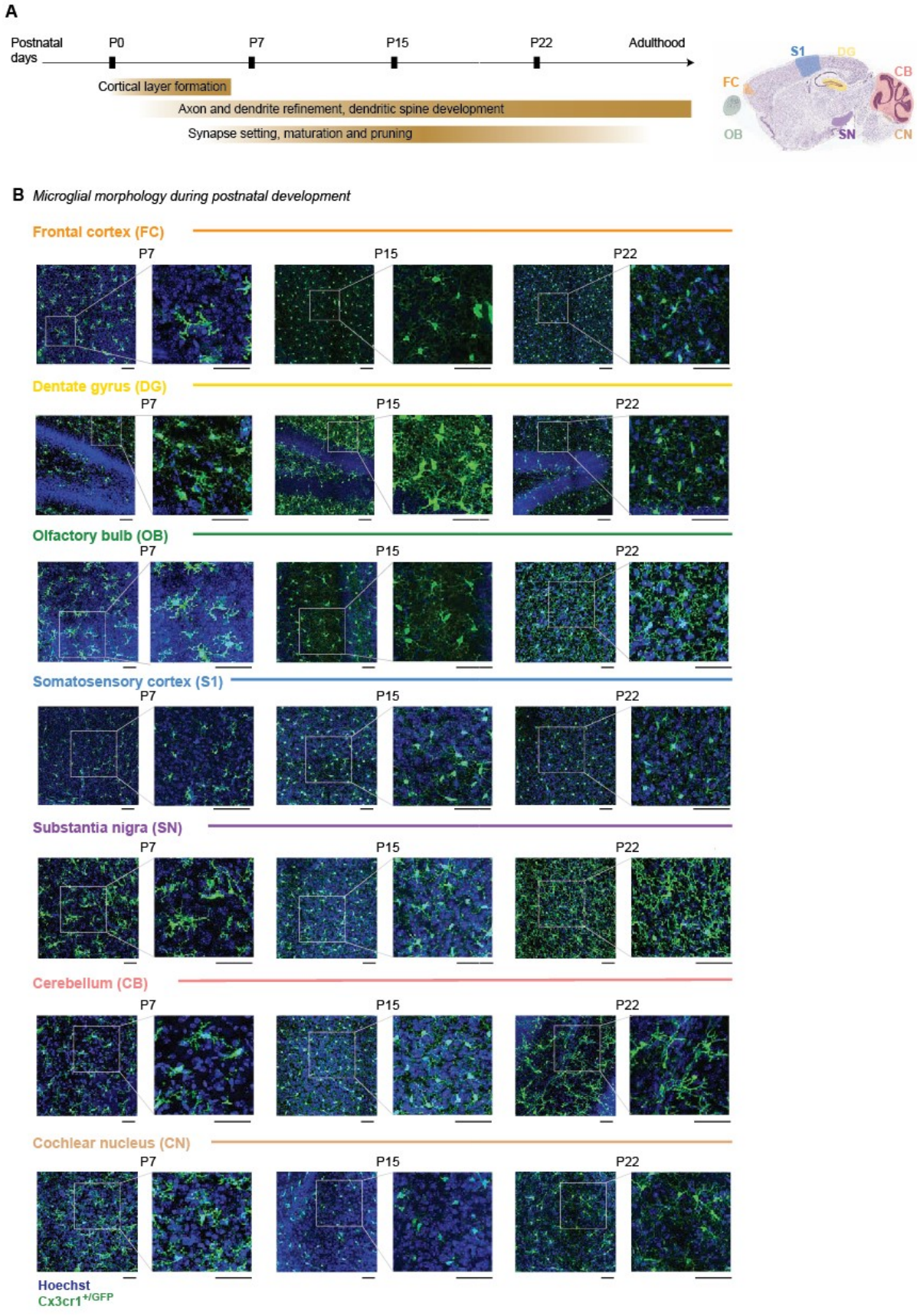
A
Postnatal days
P0
P7
P15
P22
Adulthood
Cortical layer formation
Axon and dendrite refinement, dendritic spine development
Synapse setting, maturation and pruning
S1
DG
CB
FC
OB
SN
CN
B Microglial morphology during postnatal development
Frontal cortex (FC)
Dentate gyrus (DG)
Olfactory bulb (OB)
Somatosensory cortex (S1)
Substantia nigra (SN)
Cerebellum (CB)
Cochlear nucleus (CN)
P7
P15
P22
Hoechst
Cx3cr1+/GFP

Fig. 21. Microglial phenotypes during postnatal development. **A:** Timeline of postnatal (P) brain development with highlighted events. Next: sagittal view of analyzed brain regions: olfactory bulb (OB), frontal cortex (FC), dentate gyrus (DG), somatosensory cortex (S1), substantia nigra (SN), cochlear nucleus (CN) and cerebellum (CB). **B:** Confocal images of GFP^{+} microglia (green) and cell nuclei (Hoechst, blue) from $Cx3cr1^{+/GFP}$ mice at P7, P15, and P22 for each brain region with zoom-in. Scale bar: 50 µm.

Then, we applied MorphOMICs and highlighted in the UMAP plots either each brain region (**Fig. 22A**) or the developmental time point (**Fig. 22B**). In all seven brain regions, no postnatal time points overlapped with the adult microglia (**Fig. 22A**), reflecting their morphological heterogeneity during development. When we analyzed each developmental time point individually, we found that at P7, all brain regions are distinct but occupy the same cluster, which shifted to a different cluster at P15 (**Fig. 22B**). Interestingly, CN_{mg} and DG_{mg} segregated and remained distinct from the other brain regions at P15 and P22, with CB_{mg} joining them at P22. Between P22 and adulthood, the clusters diverged to their adult microglial heterogeneity.

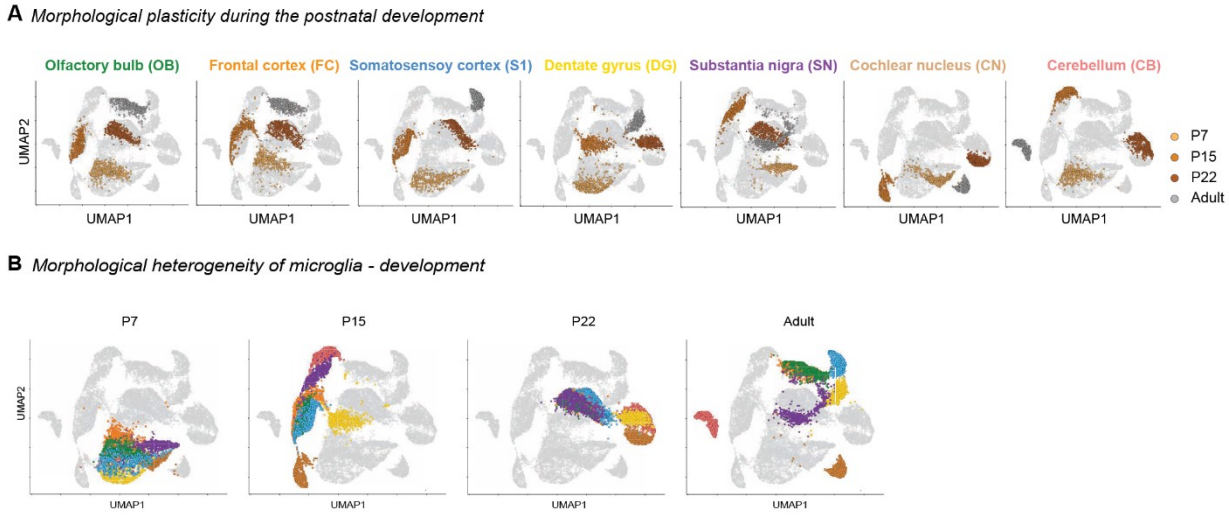

Fig. 22. Microglial phenotypic spectrum during postnatal development. **A-B:** UMAP plots of MorphOMICs-analyzed microglia across seven brain regions in Cx3cr1-$GFP^{+/-}$ mice at P7, P15, P22, and adults (**A**); and color-coded brain regions for both sexes (**B**)

Next, we investigated whether sexual dimorphism affects the microglial phenotypic spectrum during development. To do this, we applied MorphOMICs to males and females separately (**Fig. 23** and **Fig.24**). Surprisingly, we found that the clusters shown in **Fig. 22B** split, leading to well-defined male and female clusters for each brain region at P7 (**Fig. 23**).

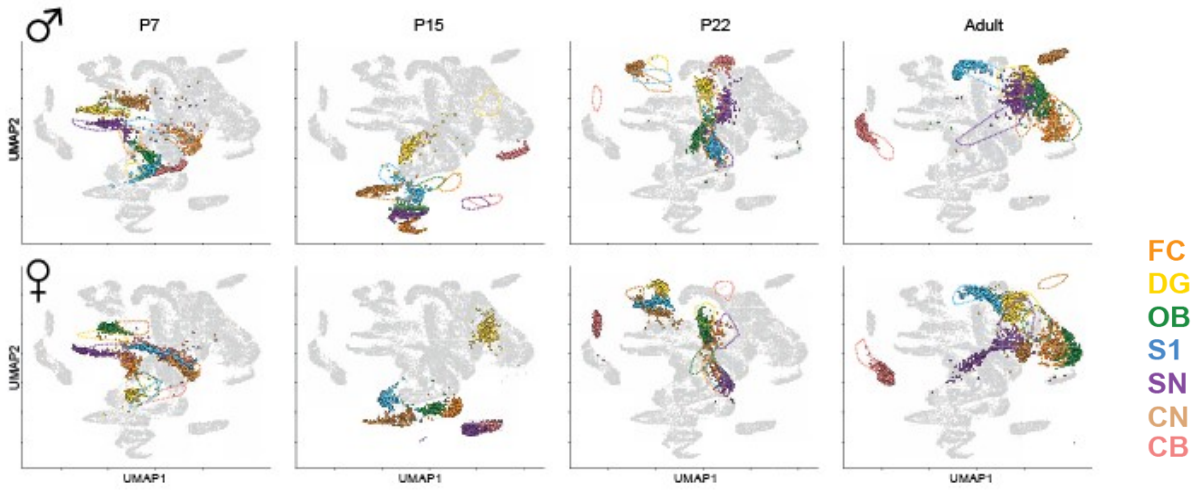

Fig. 23. Microglial sexual dimorphism during postnatal development. UMAP plots of MorphOMICs-analyzed microglia across seven brain regions in Cx3cr1-GFP$^{+/-}$ mice at P7, P15, P22, and adults for each sex independently with dashed lines vice versa as reference for each developmental time point. Each dot represents a bootstrapped persistence image.

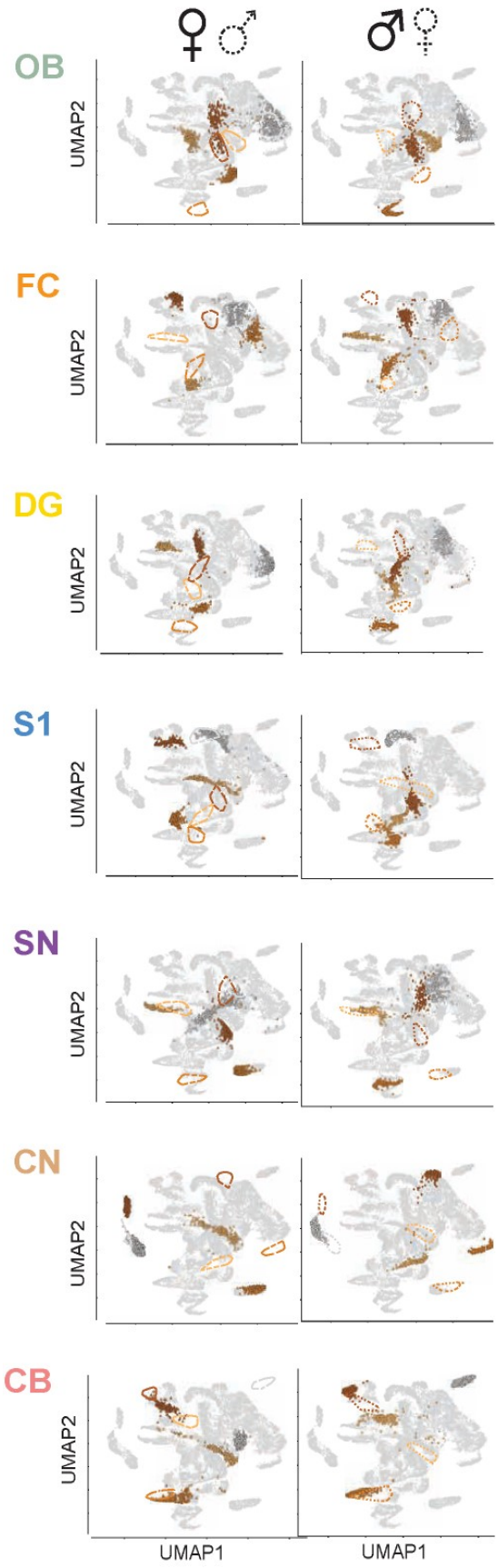

With brain maturation, ♀/♂ clusters in DG_{mg}, FC_{mg}, and $S1_{mg}$ converged, while those in CB_{mg}, CN_{mg}, OB_{mg}, and SN_{mg} remained distinct. To follow this sexual dimorphism along the developmental trajectory, we ordered the bootstrapped persistence images with the Palantir algorithm [159], which uses principles from graph theory and Markov processes to infer a pseudo-temporal trajectory (**Fig. 25**). In the Palantir space, nearby points indicate similar persistence images, thereby assuming a gradual transition in their morphologies, and the continuous sequence of points define a trajectory. The developmental trajectories were similar between brain regions, with P7 and P22 clusters being the furthest from and the closest to the adult,respectively. In contrast, P15 shifted laterally from the P7-P22 trajectory and occupied the outermost position in nearly all the brain regions, indicating a unique microglial context-dependent response that coincides with neuronal circuit synapse refinement [191–193].

Fig. 24. Microglial sexual dimorphism during postnatal development. UMAP plots of MorphOMICs-analyzed microglia for females (left) and males (right) at P7, P15, P22, and adults. Separate UMAP for each brain region and sex. Each dot represents a bootstrapped persistence image. Each dot represents a bootstrapped persistence image

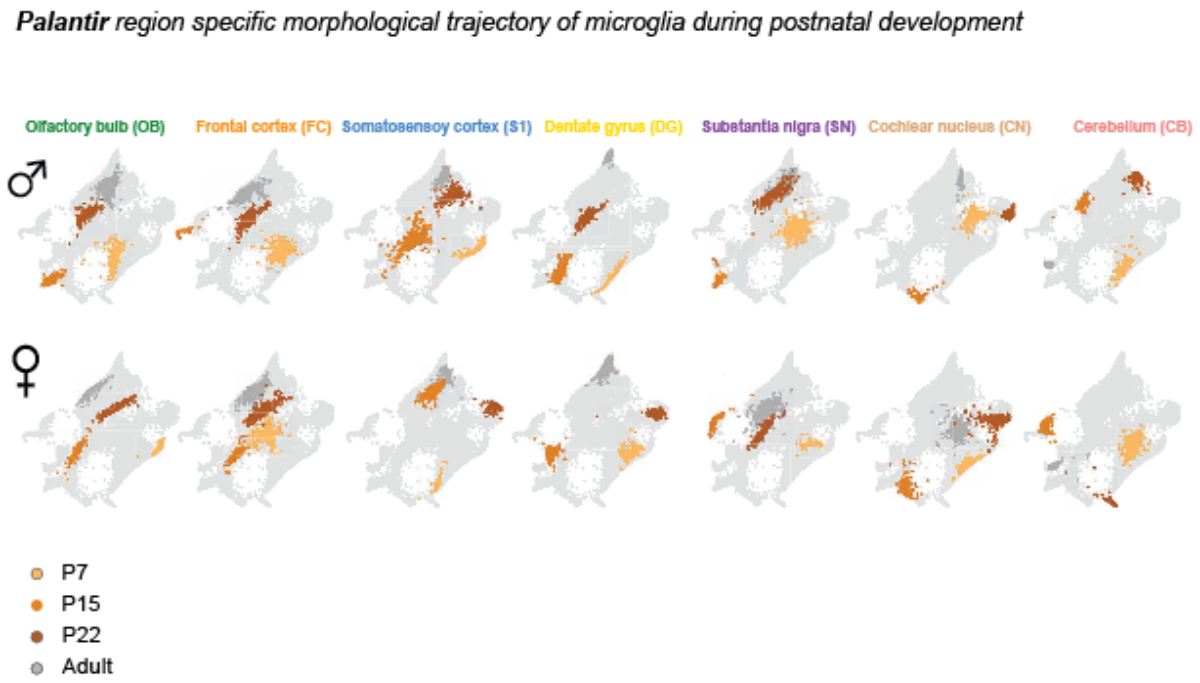

Fig. 25. Microglial sexual dimorphism during postnatal development. Palantir reconstruction of microglia morphological trajectory from **Fig.23** with highlighted P7, P15, P22, and adults for each brain region. Nearby points indicate similar persistence images. Each dot represents a bootstrapped persistence image.

4.4 Link between morphology and response in the 5xFAD context

Synaptic loss combined with amyloid plaque deposition are common signs of Alzheimer's disease, with the neocortex and the hippocampus being the most affected brain regions [194,195]. Microglial morphology alters during the progression of Alzheimer's disease [196,197] but the disease phenotype of microglia in directly- and indirectly-affected brain regions, as well as the impact on the sexual dimorphism, is not entirely understood [198–200]. To address this, we expanded our microglia with 3D-traced microglial morphologies in the 5xFAD mouse model (**Fig. 26**), which recapitulates a familial form of Alzheimer's disease [201], for all seven brain regions.

Fig. 26. 5xFAD model of familiar Alzheimer's neurodegeneration. Sagittal view of analyzed brain regions with color-code: olfactory bulb (OB), frontal cortex (FC), dentate gyrus (DG), somatosensory cortex (S1), substantia nigra (SN), cochlear nucleus (CN) and cerebellum (CB). Next: timeline of degeneration events in 5xFAD transgenic mouse model.

We focused on animals that were three and six months old ($5xFAD_{3m}$ and $5xFAD_{6m}$, respectively, **Fig. 27A**) because amyloid plaques occur first in the deep cortical layers at three months, followed by the hippocampus, coinciding with spine loss and memory deficits around 6 months [201]. As anticipated, microglia in the $5xFAD_{3m}$ group exhibited a disease phenotype in which all brain regions were distinguishable from controls. The $5xFAD_{6m}$ group formed a "disease-associated cluster" in the UMAP space, with the exception of CB_{mg} (**Fig. 28**). $S1_{mg}$, FC_{mg}, and DG_{mg} already occupied this disease-associated cluster in $5xFAD_{3m}$. To obtain insights which part of the microglia branching tree adapts during disease progression, we identified the representative bootstrap persistence image closest to the average for both control and $5xFAD_{6m}$, and then subtract them.

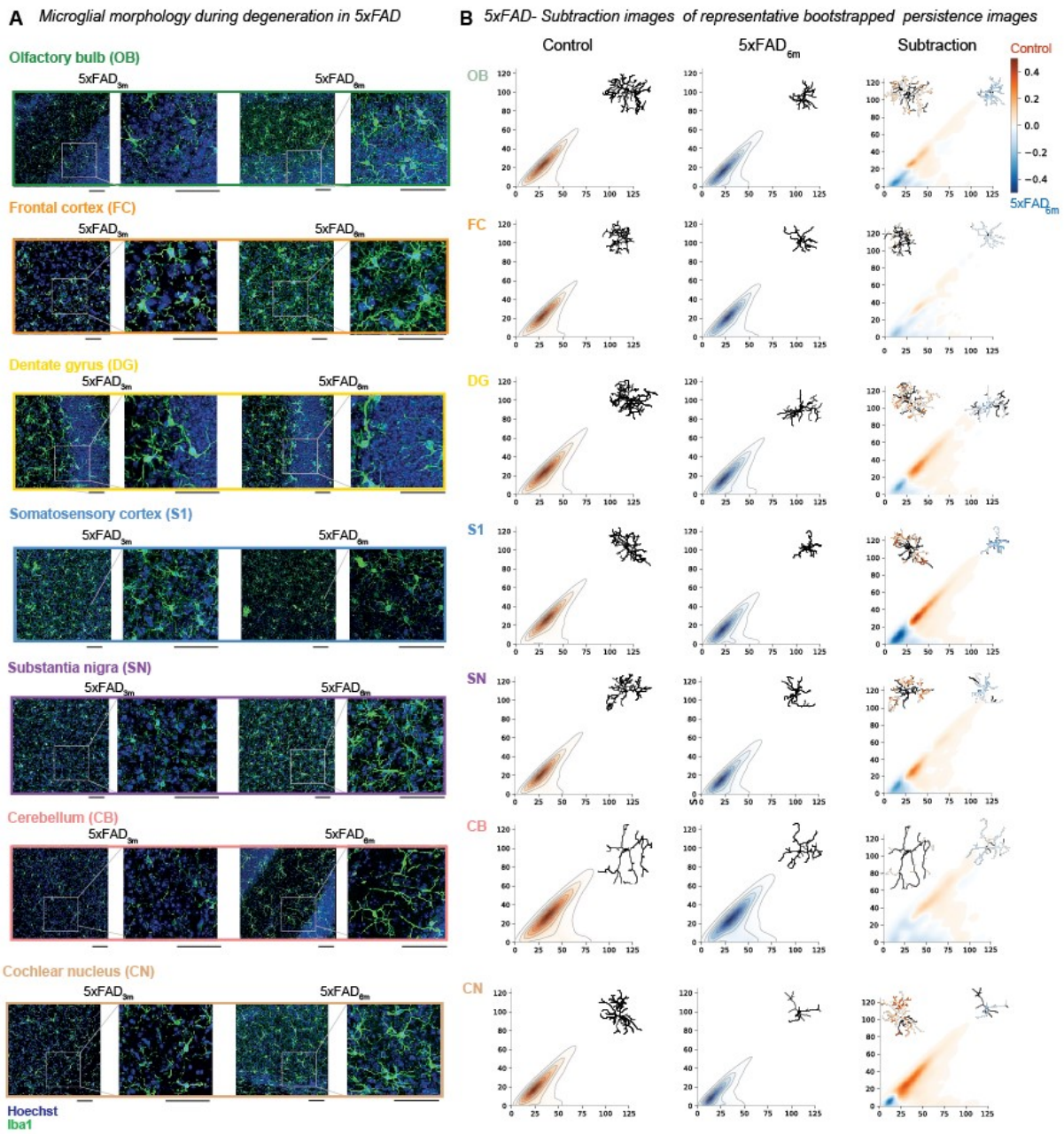

Fig. 27. Microglial morphology in the 5xFAD model of familiar Alzheimer's neurodegeneration. **A:** Confocal images showing immunostained microglia (Iba1, green) and cell nuclei (Hoechst, blue) from the analyzed brain regions in $5xFAD_{3m}$ and $5xFAD_{6m}$ (3 and 6 months, respectively) with zoom-in. Scale bar: 50 µm. **B:** Subtraction images with highlighted overrepresented processes on the representative microglia from Controls and $5xFAD_{6m}$.

Overall, the subtraction plots and the corresponding representative morphology indicate increased primary and loss of high-level branches in $5xFAD_{6m}$ compared to control (**Fig. 27B**). This effect was less pronounced in the FC_{mg} and CB_{mg} suggesting a brain-region selective microglia reactivity that might adapt in a targeted way.

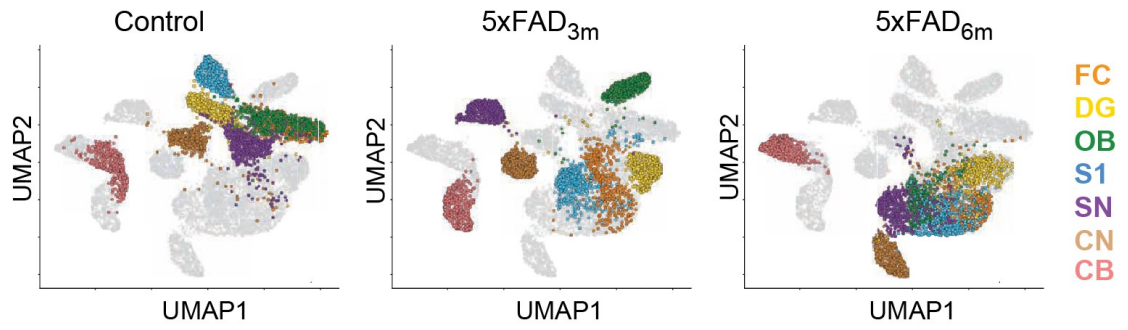

Fig. 28. Microglia phenotypic spectrum in the 5xFAD model. UMAP plots of MorphOMICs-analyzed microglia across seven brain regions (color-coded) for control, 5xFAD$_{3m}$ (3 months), and 5xFAD$_{6m}$ (6 months) with both sexes. Each degeneration time point is highlighted in a separate UMAP. Each dot represents a bootstrapped persistence image.

Next, we included the sex of the microglia in our MorphOMICs analysis. Microglia demonstrated higher morphological heterogeneity in 5xFAD$_{6m}$, with males partially overlapping and females spreading into clusters distinct from controls (**Fig. 29A**). When we applied Palantir to identify sex-dependent disease trajectories, we observed sexual dimorphism (**Fig. 29B**), especially in one of the first affected brain region, S1.

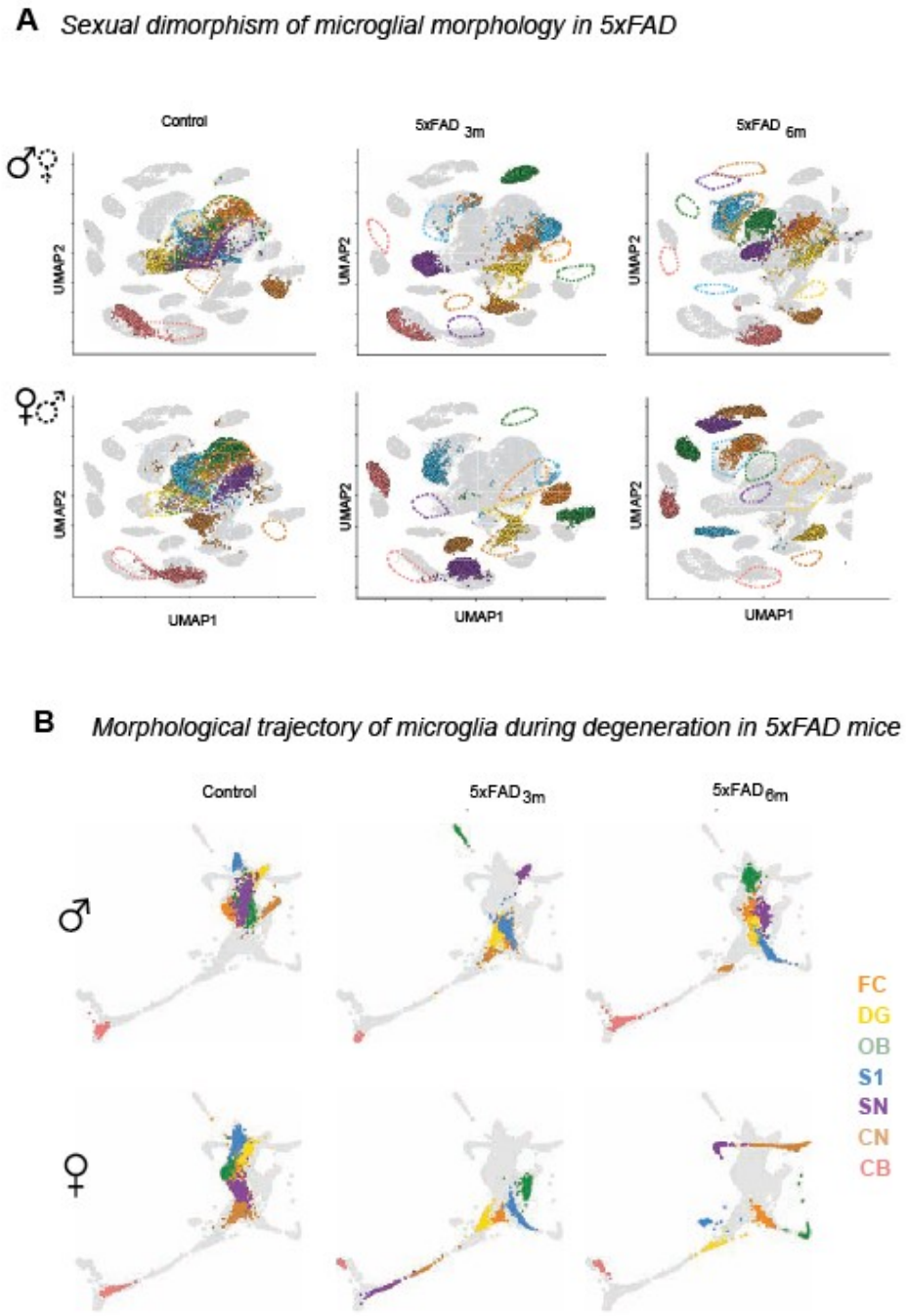

Fig. 29. Microglia phenotypic spectrum in 5xFAD transgenic model of neurodegeneration is sexually dimorphic. **A**: UMAP plots of MorphOMICs-analyzed microglia across seven brain regions (color-coded) for control, 5xFAD3m (3 months), and 5xFAD6m (6 months) separated for each sex. Each degeneration time point is highlighted in a separate UMAP. Each dot represents a bootstrapped persistence image. **B:** Palantir reconstruction of microglial morphological trajectory in males (top) and females (bottom). Each time-point highlighted in a separate Palantir plot.

♀$S1_{mg}$ seem to precede ♂$S1_{mg}$: ♀$S1_{mg}$ clusters already overlapped in $5xFAD_{3m}$ with the trajectory that males reach only at 6 months (**Fig. 30**).

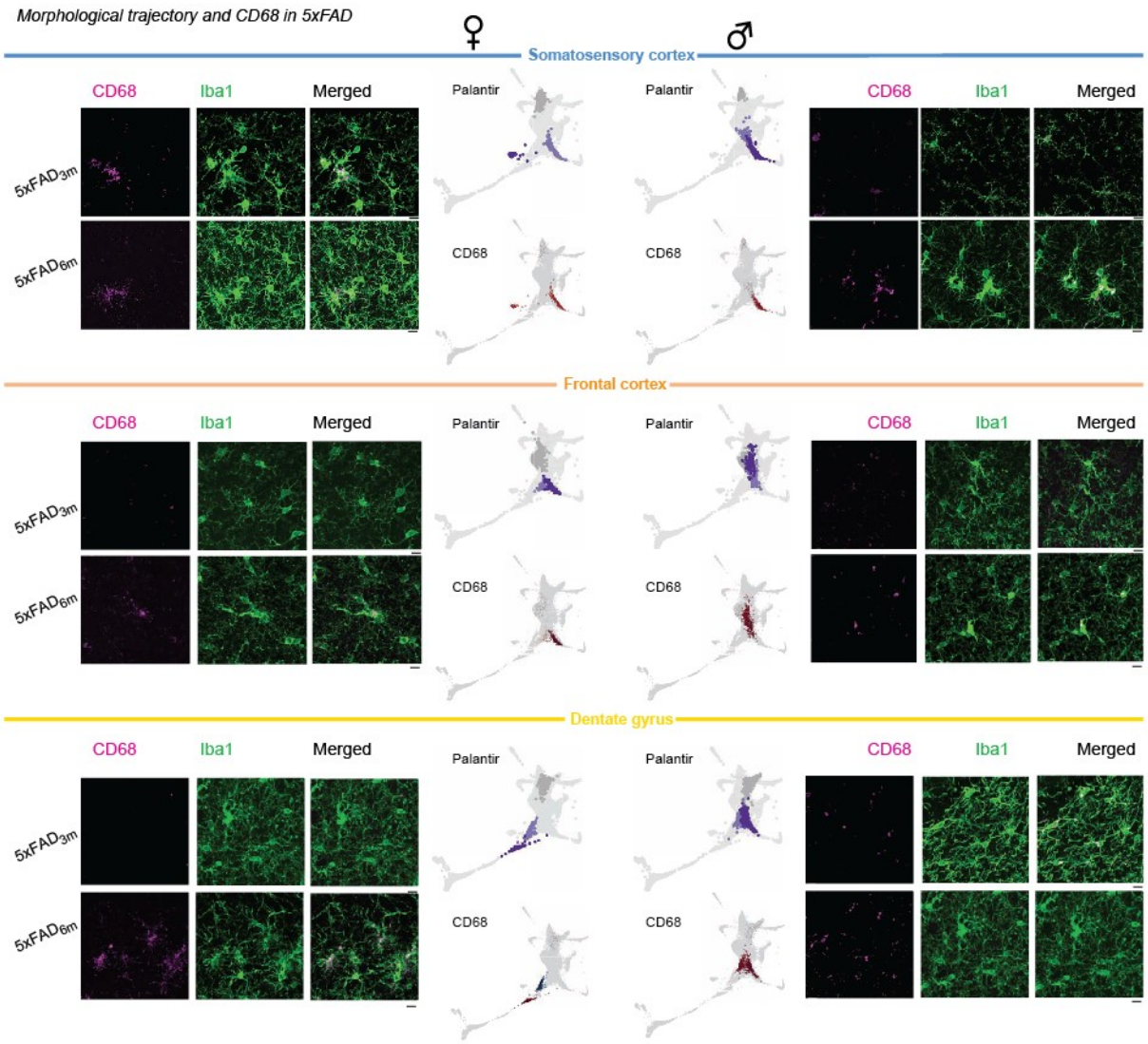

Fig. 30. Microglia morphological trajectory in 5xFAD model of neurodegeneration is sexually dimorphic. Representative confocal images of immunostained microglia (Iba1, green) and lysosome (CD68, magenta), followed by Palantir reconstruction of microglial trajectory (top) with corresponding color-coded average CD68 fold change (bottom) across 3 animals from females (left side) and males (right side) for 5xFAD3m and 5xFAD6m in S1, FC, and DG. Scale bar: 10 µm. Fold change: < 0 blue; > 0 red..

Such a difference was less obvious for FC_{mg} and DG_{mg}, which is likely influenced by the limited number of selected time points over the course of the pathology. Despite this, DG_{mg} and ♀FC_{mg} display a phenotypic spectrum along the disease trajectory. To link microglial phenotype to their reactivity, we performed immunostaining for the endosomal-lysosomal marker CD68 [202]. We then computed the fold-change compared to the control CD68 volume within $Iba1^+$-cells and overlaid the CD68 fold-change on the Palantir trajectory (**Fig. 30**). In ♀$S1_{mg}$, CD68 increased already at 3 months while this only occurred in ♂$S1_{mg}$ at 6 months, confirming that the shift along the morphological spectrum happens earlier in females. For the other brain regions, this effect was less obvious. We also applied Palantir trajectories to the other brain regions, since plaque deposition has been reported in the olfactory bulb and brainstem [203]. We

found a strong sexual dimorphism in microglial morphology in these brain regions, with less-obvious trajectory changes (**Ext. Data Fig. 8**). CB_{mg} was the only exception, remaining mainly unaffected in 5xFAD mice, which is consistent with previous literature [201]. Overall, the 5xFAD data indicate that the link between microglial disease phenotype and reactivity state depends on the brain region.

4.5 Early shift of microglial morphology in female CK-p25 mice

An alternative model with faster onset and disease progression is the CK-p25 model for sporadic Alzheimer-like degeneration [151,153,204]. Upon doxycycline withdrawal, p25 expression is induced in $CamKII^{+}$ forebrain neurons resulting in neurotoxic activity of the cyclin-dependent kinase Cdk6 [205]. Within two weeks, CK-p25 mice develop progressive neuronal and synaptic loss, forebrain atrophy, aberrant amyloid-precursor protein processing, hyper-phosphorylation of tau [151,152], and at later stages neurofibrillary tangle-like pathology [151,152] (**Fig. 31**).

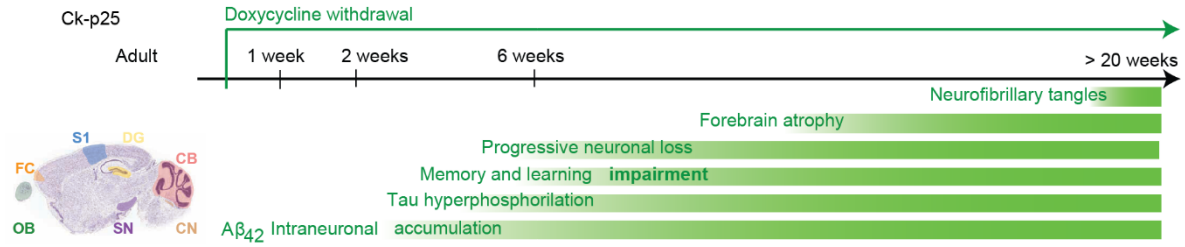

Fig. 31. CK-p25 model of sporadic neurodegeneration. Sagittal view of analyzed brain regions with color-code: olfactory bulb (OB), frontal cortex (FC), dentate gyrus (DG), somatosensory cortex (S1), substantia nigra (SN), cochlear nucleus (CN) and cerebellum (CB). Next: timeline of degeneration events upon doxycycline withdrawal in the CK-p25 transgenic mouse model.

We reconstructed microglial morphologies from CK-p25 mice at 1, 2, and 6 weeks ($CK\text{-}p25_{1w}$, $CK\text{-}p25_{2w}$, $CK\text{-}p25_{6w}$, respectively, **Fig. 32A-B**), included them to our library, and applied MorphOMICs. Similar to 5xFAD, all seven brain regions started to segregate from the control at 1 week and occupied a disease-associated cluster in $CK\text{-}p25_{6w}$, with CB_{mg} and CN_{mg} staying distinct (**Fig. 32C**). FC_{mg} reached this cluster already at 2 weeks, while OB_{mg}, DG_{mg}, $S1_{mg}$, and SN_{mg} only at 6 weeks. When we obtained the subtraction plots between control and $CK\text{-}p25_{6w}$, we found that microglia in $CK\text{-}p25_{6w}$ have lost their high-level branches and their primary branches were overrepresented compared to control suggesting a reactive phenotype (**Fig.**

32C). In contrast, CB_{mg} only showed a mild response likely due an indirect effect, as CaMKII is not expressed in the cerebellum. CN_{mg} morphology was mostly unaffected.

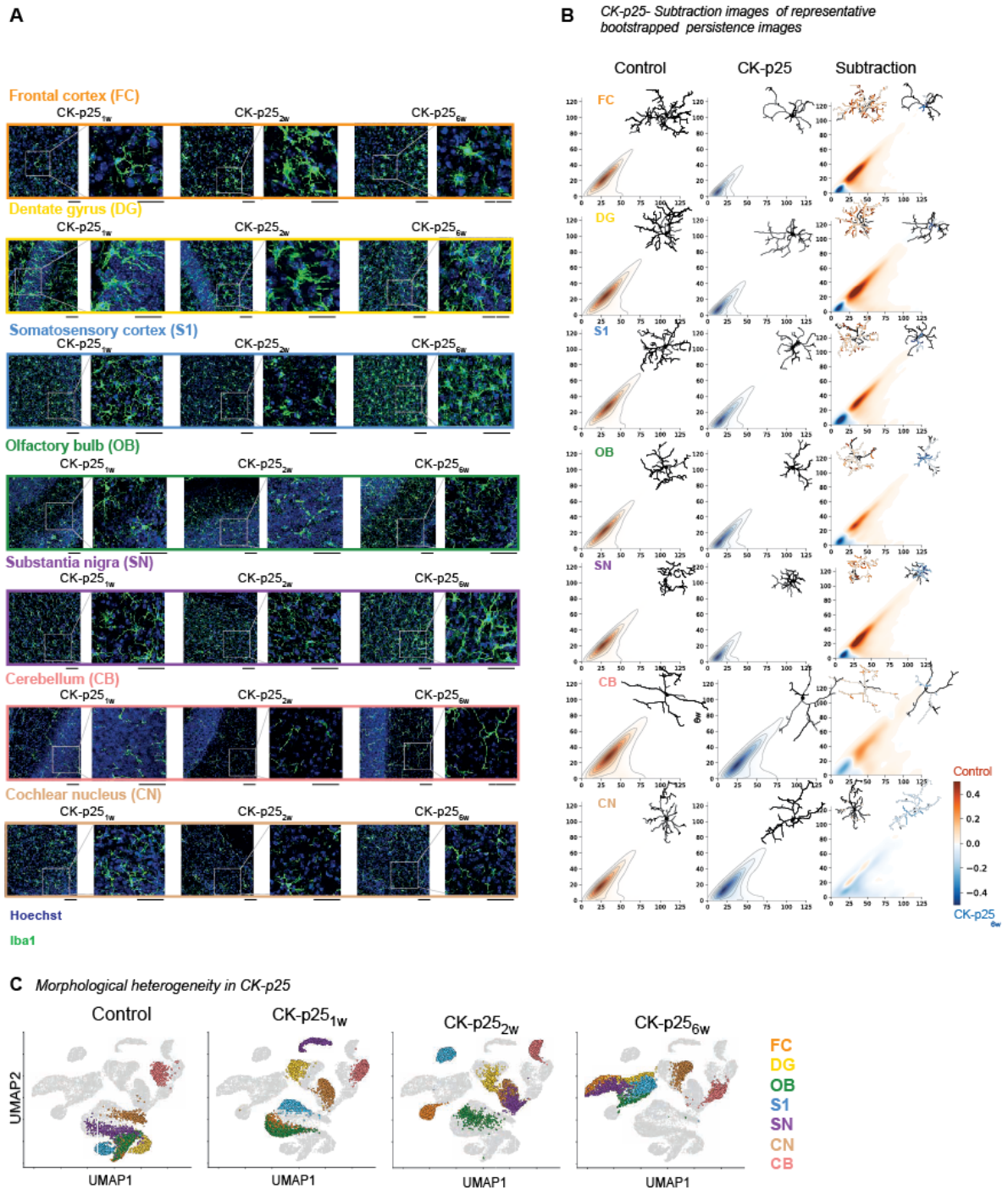

Fig. 32. Microglia phenotypic spectrum in the CK-p25 model of sporadic neurodegeneration. **A:** Confocal images showing stained microglia (Iba1, green) and cell nuclei (Hoechst, blue) from analyzed brain regions and $CK\text{-}p25_{1w}$, $CK\text{-}p25_{2w}$, $CK\text{-}p25_{6w}$ mice (1-, 2- and 6-weeks after doxycycline withdrawal) with zoom-in. Scale bar: 50 µm. **B:** Representative persistence images corresponding to each cluster centroid from © with color-coded process density. Top right corner, representative traced microglia. Subtraction image with highlighted overrepresented processes on the representative microglia. **C:** UMAP plots displaying microglial morphological heterogeneity in adult control mice and CK-p25 mice 1, 2 and 6 weeks after doxycycline withdrawal across all

the analyzed brain regions for both sexes. Each dot represents a bootstrapped persistence image, and each UMAP highlights a distinct degeneration time point.

Next, we applied MorphOMICs to the CK-p25 dataset separated by sex. We found that ♀(SN, FC, OB, DG, and S1)$_{mg}$ reached the disease cluster at 6 weeks, while in males, ♂DG$_{mg}$ and ♂S1$_{mg}$ stayed distinct (**Fig. 33A**). Similarly, Palantir displayed a trajectory arm, on which microglial morphology from later disease stages accumulated (**Fig. 33B**).

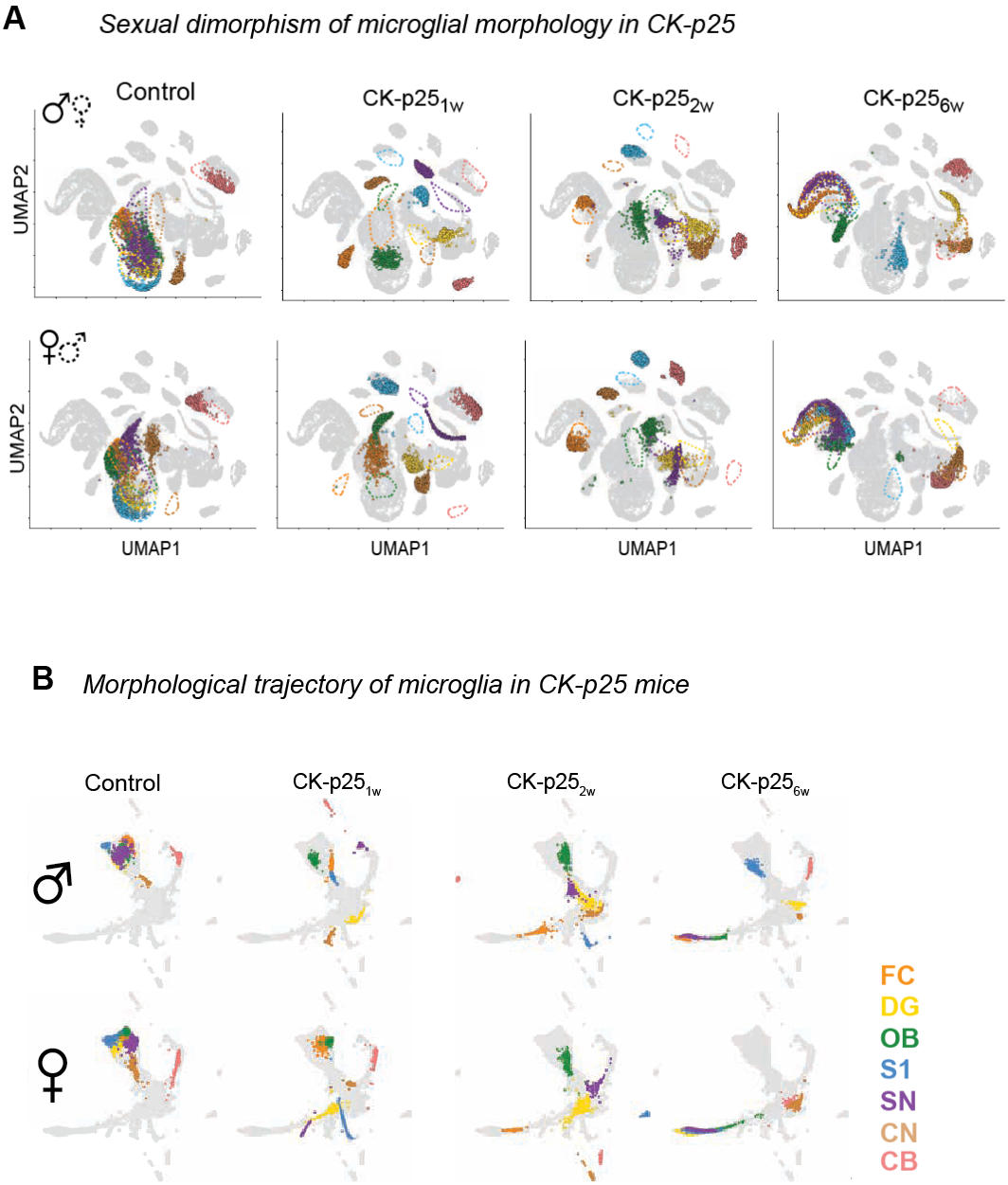

Fig. 33. Microglial phenotype in CK-p25 model of neurodegeneration is sexually dimorphic. **A:** UMAP plots displaying microglial morphological heterogeneity in adult control mice and CK-p25 mice 1, 2 and 6 weeks after doxycycline withdrawal across all the analyzed brain regions for each sex separated. Each dot represents a bootstrapped persistence image, and each UMAP highlights a distinct degeneration time point. **B:** Palantir

reconstruction of microglial morphological trajectory in males (top) and females (bottom) in control and CK-p25 mice. Each disease time-point highlighted in a separate Palantir plot.

Neither CN_{mg} nor CB_{mg} reached this disease-associated arm as expected, due to the low expression of CaMKII in these brain regions [206]. Comparison of the sex-specific Palantir projections also showed that ♀FC_{mg} preceded ♂FC_{mg} in CK-$p25_{2w}$ (**Fig. 34**). We replicated the same dynamics with Monocle, an alternative algorithm which uses reverse graph embedding to infer a pseudo-time trajectory (**Ext. Data Fig. 9A**) [207].

When we overlaid the CD68 fold-change compared to control adults over the Palantir FC_{mg} trajectory, we found that the CD68 fold-change gradually increased (**Fig. 34**) suggesting a CD68 dynamics that is different from morphological adaptations. Indeed, morphological changes did not correspond to CD68 in ♀DG_{mg} and ♀$S1_{mg}$ at 6 weeks: the morphology reached the disease-associated arm but without increased CD68 fold change. Instead, ♂DG_{mg} and ♀DG_{mg} showed their highest CD68 fold change at 2 weeks and occupied a similar cluster in the Palantir space (**Fig. 34**). Together, this suggests that the microglial response might be associated with the transient effect of p25 expression, which has been shown to enhance long-term potentiation and improve hippocampus-dependent memory, before inducing neurodegeneration, gliosis, and severe cognitive decline at 6 weeks [153]. For those brain regions that were less affected, dimorphic microglial phenotype was less pronounced (**Ext. Data Fig. 9B**). In both sexes, SN_{mg} and OB_{mg} in CK-$p25_{6w}$ reached the disease-associated arm, whereas in CB_{mg} and CN_{mg}, neither sex nor disease progression influenced morphology (**Ext. Data Fig. 9C**). Overall, the CK-p25 model exhibited strong dimorphic phenotype spectrum in favor of females, which precede their male counterparts in a brain-region-specific manner.

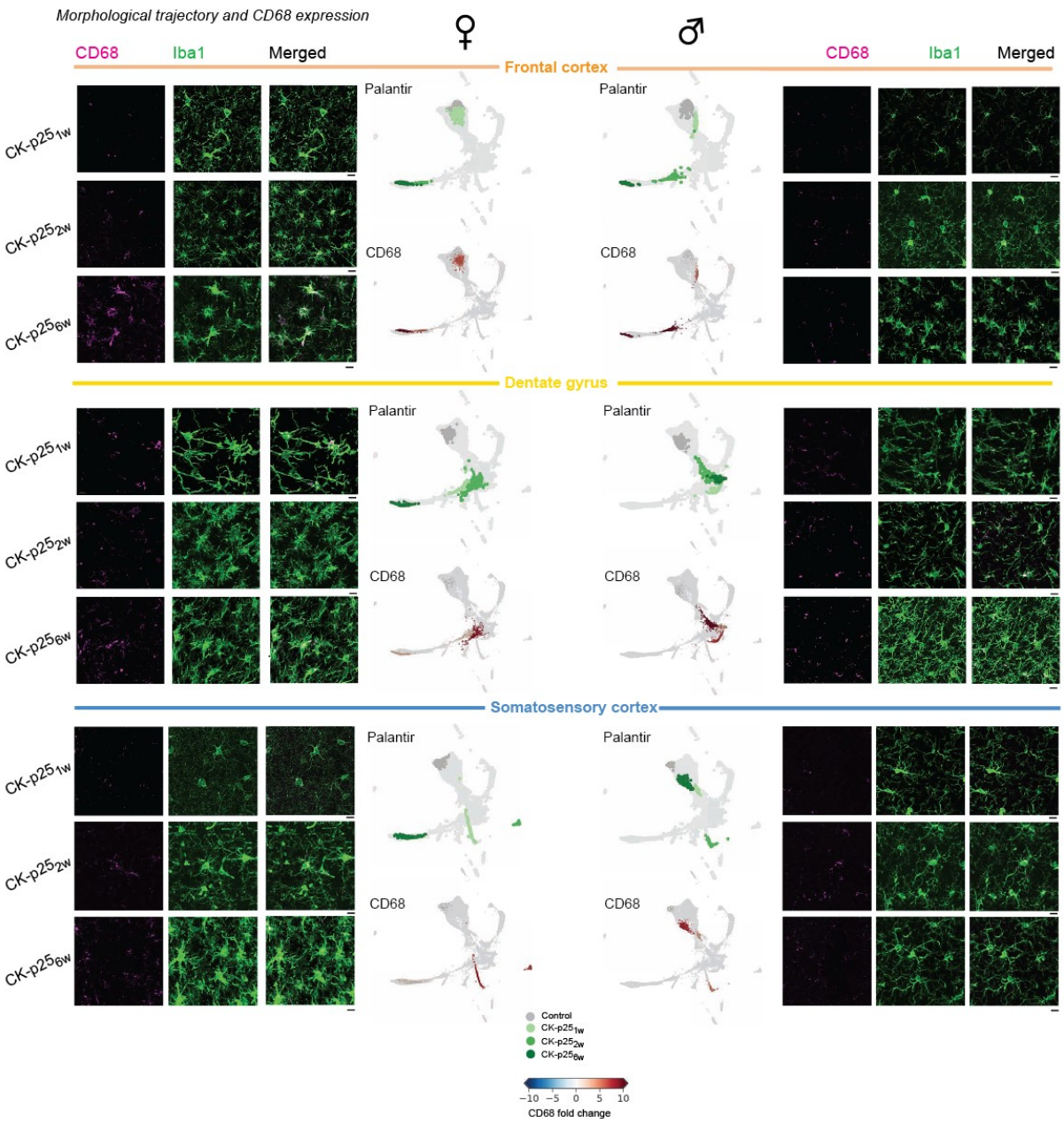

Fig. 34. Microglia morphological trajectory of females in CK-p25 model of neurodegeneration exhibit an earlier morphological shift than in males. Representative confocal images of immunostained microglia (Iba1, green) and lysosome (CD68, magenta) in CK-p25 mice 1, 2, and 6 weeks after doxycycline withdrawal in S1, FC, and DG. Scale bar: 10 µm. Palantir reconstruction of microglial trajectory (top) with corresponding color-coded average CD68 fold change (bottom) across 3 animals. Females: left. Males: right. Fold change: < 0 blue; > 0 red.

4.6 Morphological information extraction with MorphOMICs

So far, we established both an adult sexual dimorphic microglia phenotype and a morphological spectrum during development and degeneration for seven brain regions. To further exemplify the superior role of MorphOMICs over morphological feature selection, we applied common classifiers to the CK-p25 FC_{mg} dataset. Neither performing pairwise statistical comparisons of time points with common classifiers (**Fig. 35A**) nor applying bootstrapping approaches to an

extended set of non-interdependent morphometric quantities (**Fig. 35B**) replicated the sexually dimorphic control-to-disease spectrum from **Fig. 34**.

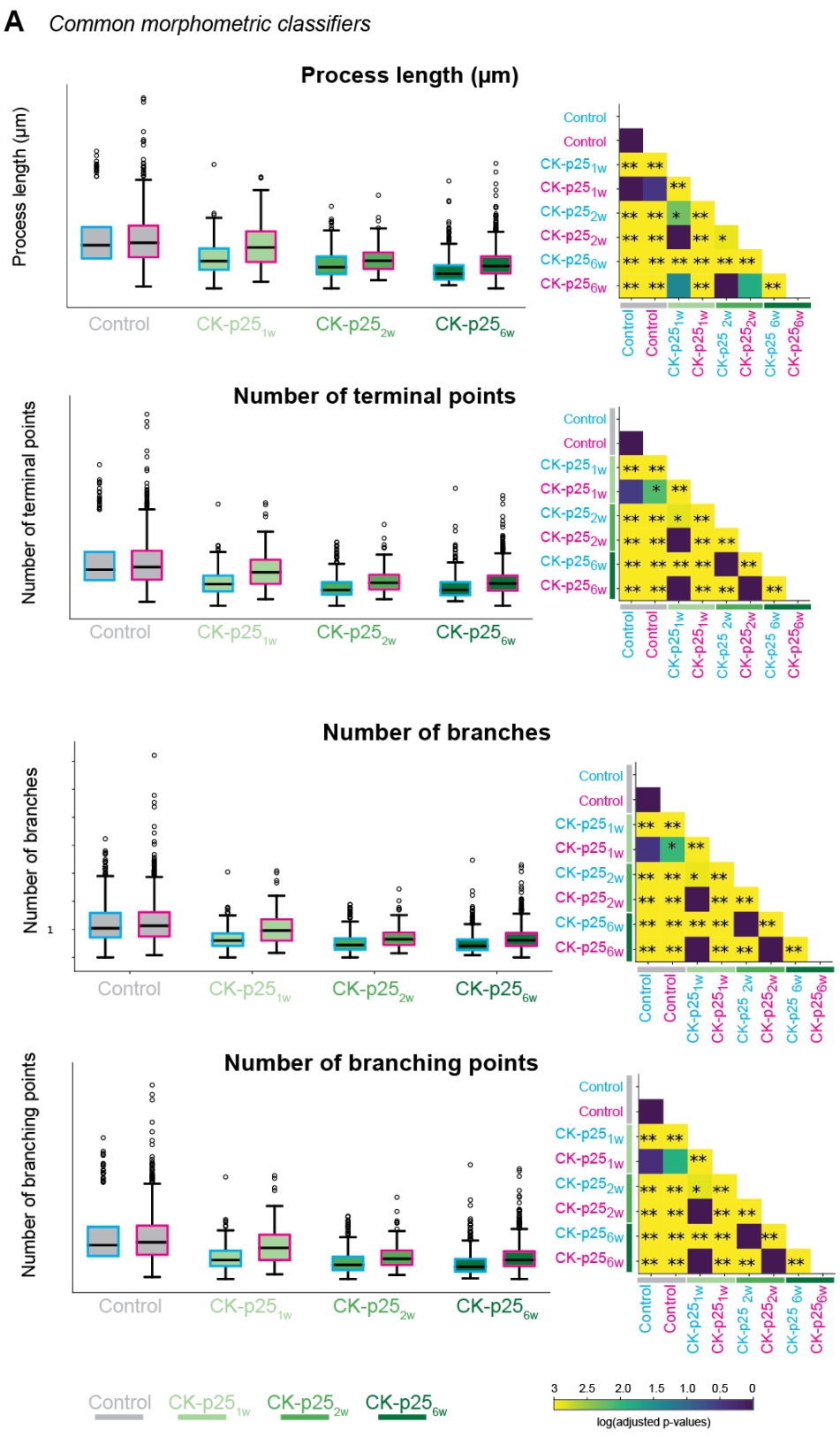

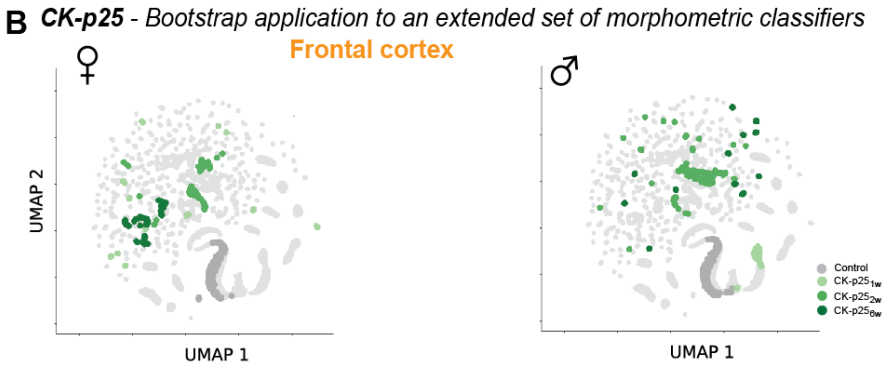

Fig. 35 . Classical morphometrics do not recapitulate sexual dimorphism in CK-p25 mice. **A:** Box plots for the selected features process length, number of branches, terminal- and branching points of control ($n_{♀}$= 926, $n_{♂}$= 894), and CK-p25$_{1w}$ ($n_{♀}$= 219, $n_{♂}$= 194), CK-p25$_{2w}$ ($n_{♀}$= 264, $n_{♂}$= 492), CK-p25$_{6w}$ ($n_{♀}$= 858, $n_{♂}$= 462) mice (1-, 2- and 6-weeks after doxycycline withdrawal, respectively) in the frontal cortex (FC). Next: matrices showing color-coded p-values for the pairwise comparison of each morphometric. * $p < 0.05$, ** $p < 0.01$. **B:** Bootstrapped and UMAP representations of an extended set of morphological classifiers (see **Ext. Data Table 4**) applied to females (left) and males (right) in, CK-p25 (**B**) Each dot represents an averaged extended set of morphometric classifiers across 30 microglia that form the bootstrap population.

Similarly, we observed the same information loss for FC_{mg} in the 5xFAD model and during development (**Fig. 36A-B**) although microglia from adult brain regions segregate (**Fig. 36C**), suggesting that MorphOMICs preserves certain intrinsic properties of the reconstructed tree after dimensionality reduction.

To identify which properties are potentially relevant, we looked at the most variable pixels across CK-p25 FC_{mg} and the control bootstrapped persistence images (**Fig. 36D**).

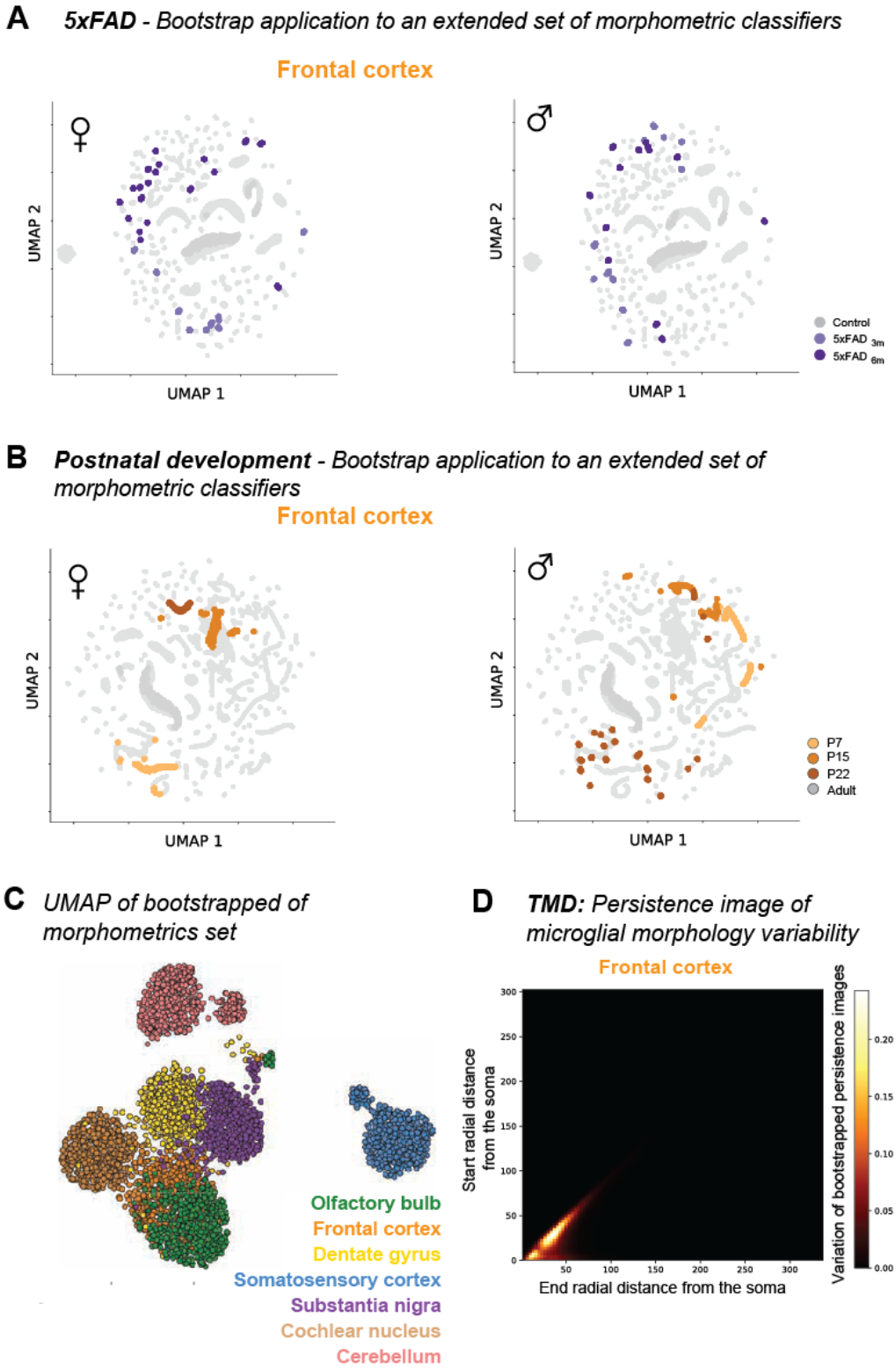

Fig. 36. Classical morphometrics do not recapitulate sexual dimorphism from in 5xFAD and development **A:** Bootstrapped and UMAP representations of an extended set of morphological classifiers (see **Ext. Data Table 4**) applied to females (left) and males (right) in 5xFAD (**A**) and developmental time points (**B**) with highlighted frontal cortex (calculation without cochlear nucleus and cerebellum for simplicity). Each dot represents an averaged extended set of morphometric classifiers across 30 microglia that form the bootstrap population. **C:** Morphometric UMAP of the bootstrapped comprehensive 27 morphometrics set showing regional heterogeneity of microglia in adult healthy mice. Brain regions are color-coded. **D**: Heat-map of the bootstrapped persistence

images pixel-wise standard variation across control and CK-p25 conditions of the frontal cortex. Black: no variation. White: high variation.

We found the highest variability along the diagonal and close to origin of the persistence diagram corresponding to short branches and branches close to the soma (see also **Fig. 12**, iv). We therefore decided to zoom-in on the short and the long persistence bars, filtered them out separately, and repeated our MorphOMICs analysis (**Fig. 37A-D**). Using this method, we saw those bars corresponding to primary processes, sufficed to capture the sexually dimorphic phenotypes along the disease trajectory that we have previous seen (**Fig. 37C**). Interestingly, when we focused only on the short bars, reflecting short terminal processes, we found that males aggregated across all time points in a corner, whereas the females gradually adapted (**Fig. 37D**). These results suggest that persistence barcodes highlight different phenomena, and therefore both short and long bars are essential for the understanding of morphology.

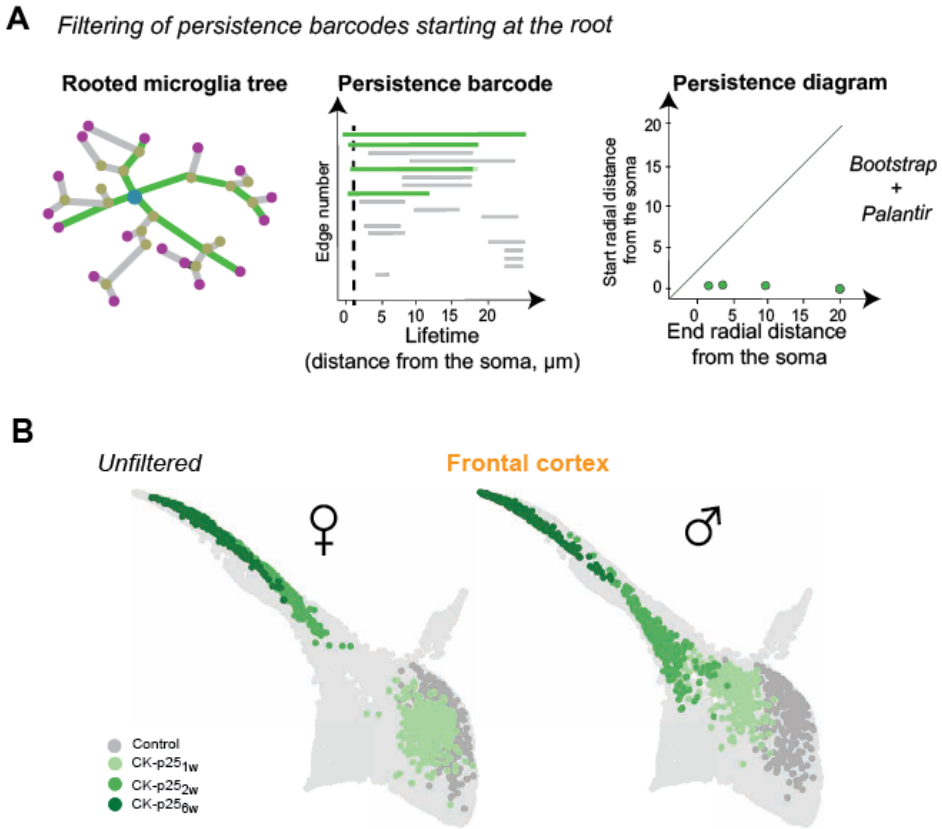

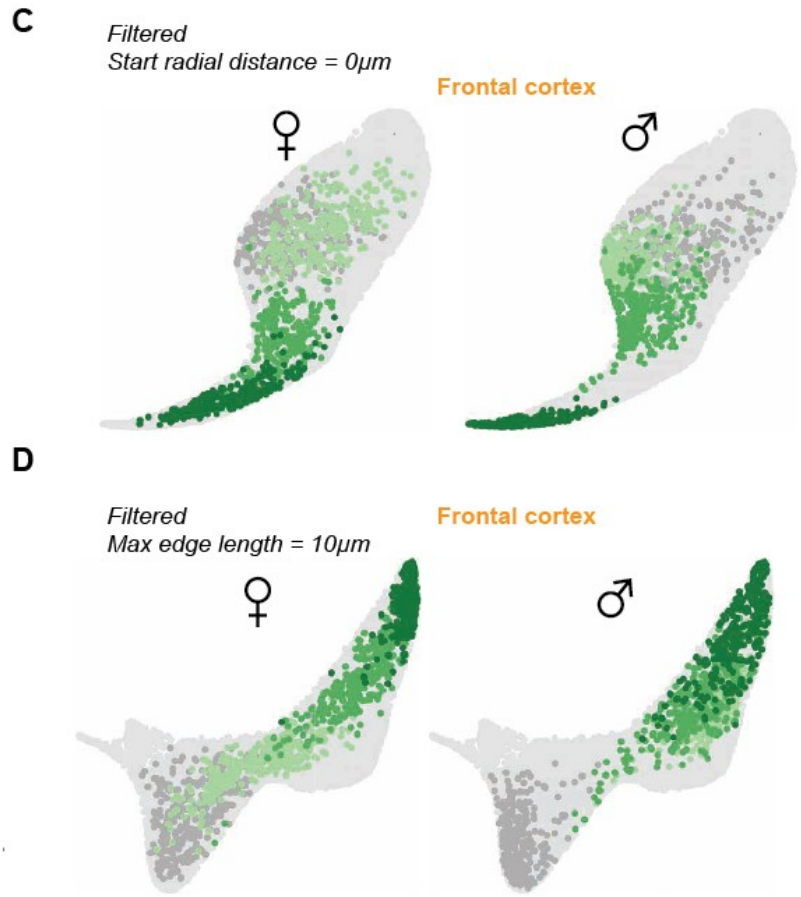

Fig. 37. MorphOMICs applied to primary processes reiterates sexual dimorphism in CK-p25 mice. **A:** Schematic for filtering persistence barcodes with MorphOMICs. Starting from microglial rooted tree, only bars are selected that are born at 0 µm independent of their length (representing likely primary branches, green), and are converted into a persistence diagram. **B-D**: Palantir trajectory of all brain region (without cochlear nucleus and cerebellum for simplicity) from control and CK-p25 condition with highlighted FC microglia trajectory for females (left) and males (right) with (**B**) unfiltered or filtered bars (**C**: start radial distance from the soma: 0 µm, **D**: maximum bar length: 10µm).

4.7 Atlas of context- and cue-dependent microglial phenotypes

Until now, we have treated microglial morphology separately for development and disease. Since both conditions induce a shift along the morphological spectrum, we were interested in how these conditions integrate along the pseudo-temporal trajectory to form a microglia reactivity spectrum. To achieve this, we performed MorphOMICs for each brain region and sex separately, including all developmental and disease points and extracted the trajectory with Palantir (**Fig. 38, Fig. 39**, **Ext. Data Fig. 10A-B**). We first focused on the female reactivity spectra for FC_{mg} and DG_{mg} (**Fig. 38**). In ♀FC_{mg}, P7, P15, P22, 5xFAD_{3m}, and 5xFAD_{6m} groups aligned together reaching out towards the CK-$p25_{2w}$ and CK-$p25_{6w}$ groups, which extends away from all the other conditions, forming a disease-associated arm. Interestingly, ♀DG_{mg}

mimicked a similar spectrum but with both 5xFAD and early CK-p25 forming a cluster distant from the P15 and the control, and the P7 group reaching out towards CK-p25$_{6w}$. In both regions, microglia in 5xFAD$_{6m}$ never reach the disease-associated arm suggesting a milder environmental condition compared to the late stages of CK-p25 neurodegeneration.

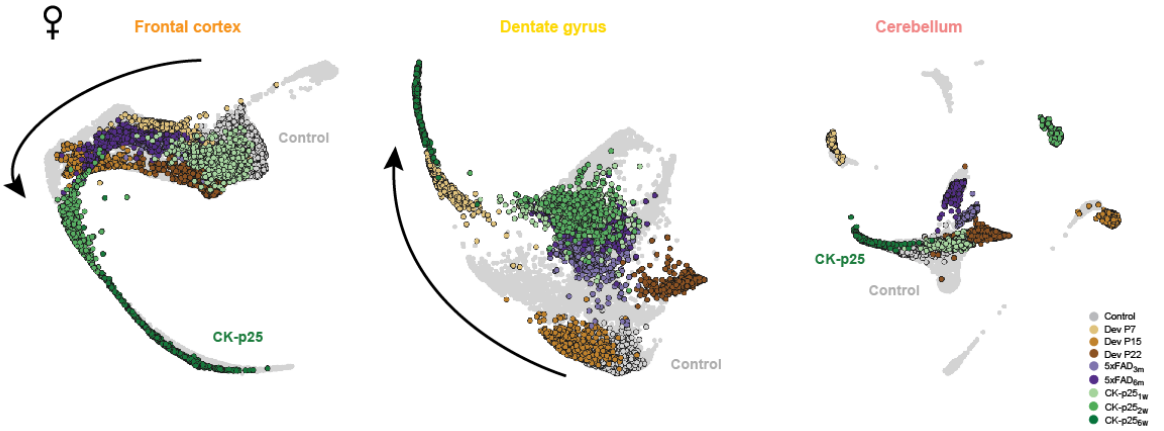

Fig. 38. ***Reactivity spectrum in females FC, DG and CB***. Palantir reconstructions calculated independently for each brain region for the conditions: control, P7, P15, P22, CK-p25$_{1w}$ (1-week), CK-p25$_{2w}$ (2 weeks), CK-p25$_{6w}$ (6 weeks), 5xFAD$_{3m}$ (3 months), and 5xFAD$_{6m}$ (6 months) and both sexes. Microglial trajectory highlighted for females. Black arrow: control-to-disease spectrum

In males, disease phenotypes evolved more slowly than in females, with only ♂FC$_{mg}$ reaching the disease-associated arm at CK-p25$_{6w}$ (**Fig. 39**). Like in females, we observed both 5xFAD groups close to the control together with P15, followed by intermingled P7, P22, CK-p25$_{1w}$. In ♂DG, microglial morphologies from P7 and CK-p25$_{1w}$ clustered together, segregating from the rest of the conditions. Overall, ♂DG$_{mg}$ displayed a similar phenotypic spectrum compared to ♂FC$_{mg}$ for both 5xFAD groups, shifting towards the CK-p25$_{2w}$-CK-p25$_{6w}$ cluster. In the CB, both ♀ and ♂ CB$_{mg}$, do not show any clear trajectory progression. Whereas the disease clusters mostly intermingle with the control suggesting only a minor response to the disease environment, the developmental time points were distinct to the control (**Fig. 38, Fig. 39**). Overall, our data show that microglia display a spectrum of phenotypes, with developmental time-points occupying distinct parts of the trajectory in a brain-region-dependent manner.

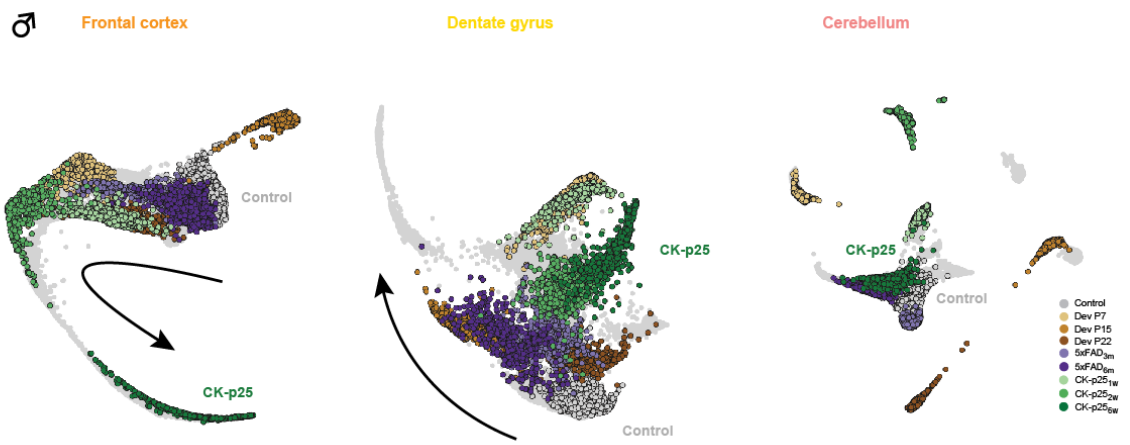

Fig. 39. Reactivity spectrum in males FC, DG and CB. Palantir reconstructions calculated independently for each brain region for the conditions: control, P7, P15, P22, CK-p25$_{1w}$ (1-week), CK-p25$_{2w}$ (2 weeks), CK-p25$_{6w}$ (6 weeks), 5xFAD$_{3m}$ (3 months), and 5xFAD$_{6m}$ (6 months) and both sexes. Microglial trajectory highlighted for males. Black arrow: control-to-disease spectrum.

4.8 Morpho-functional relationship after repeated ketamine

We have built a comprehensive library of 3D-traced microglia that in combination with MorphOMICs resolved a reactivity spectrum that can serve as a reference atlas for future addition of microglial morphologies (**Ext. Data Fig. 10C**). To demonstrate the utility of such an atlas, we focused on S1 and used linear regression to estimate the location of the Palantir coordinates within a larger atlas with 2000 bootstrapped persistence images per condition (**Ext. Data Fig. 10D**). As a first proof-of-concept, we generated new sets of bootstrapped images in all conditions and successfully mapped them to their corresponding clusters (**Fig. 40A**).

Next, we have recently shown a microglia-mediated extracellular matrix remodeling upon repeated exposure with anesthetic ketamine [117]. Such treatment results in a dose-dependent microglia-mediated loss of the perineuronal net (PNN) in the S1 and induces changes in plasticity [117]. However, we were not able to resolve morphological changes by eye (**Fig. 40C**). Thus, we 3D-traced microglia in S1 of adult C57BL/6J mice after 1×, 2×, 3× KXA treatment as well as after 3-days, 1-week, and 2-weeks recovery after the 3× KXA exposure, applied MorphOMICs, and mapped their positions on the S1 reference atlas (**Fig. 40A**). Consistent with our previously reported dosage-dependent effect, 1× KXA did not lead to morphological adaptation, while with each additional dosage the microglial morphology gradually connected to the reactivity spectrum. In parallel, CD68 expression further upregulated with each additional dosage (**Fig. 40B-C**). This shows that MorphOMICs provides the fundaments for a morphology-function relationship, which could not be uncovered otherwise. Remarkably,

MorphOMICs provides also a readout of microglial morphology adaptations following withdrawal after 3× KXA, which we have shown to reinstate PNN [117]. First, the morphology regresses towards the control phenotype after 3-days recovery (**Fig. 40A**). Then, the microglial morphology separates on a trajectory, which diverges from the control and the KXA-treated ones suggesting a recovery-associated microglial phenotype.

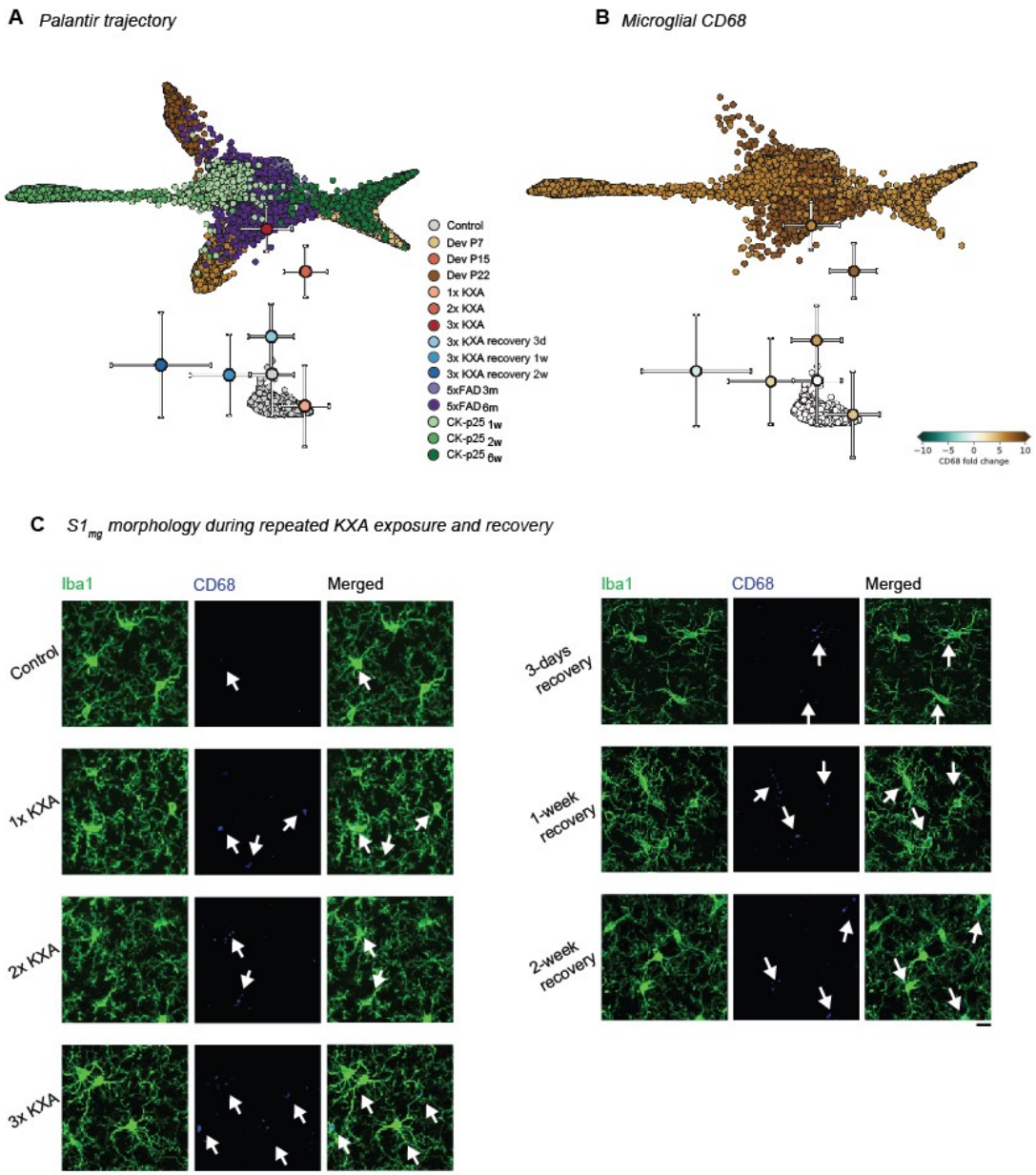

Fig. 40. MorphOMICs applied to KXA treated microglia. **A**: Palantir reconstruction of microglia morphological trajectory in primary somatosensory cortex (S1) from adult control, P7, P15, P22, 5xFAD$_{3m}$ (3 months), 5xFAD$_{6m}$ (6 months), CK-p25$_{1w}$ (1-week), CK-p25$_{2w}$ (2-weeks), CK-p25$_{6w}$ (6-weeks), 1×, 2×, 3× KXA (ketamine-xylazine-acepromazine), and 3× KXA recovery after 3-days (3d), 1-week (1w), 2-weeks (2w). Centroids indicating the mean position of mapped points in a given condition with the corresponding standard deviations. **B**: Corresponding color-coded average CD68 fold change across 3 animals. Fold change: blue < 0; brown > 0. **C**: Representative confocal images of immunostained microglia (Iba1, green) and endosomal-lysosomal CD68 (blue) from control, 1×, 2×, 3× KXA (ketamine-xylazine-acepromazine), and 3× KXA recovery after 3-days (3d), 1-

week (1w), 2-weeks (2w) from the primary somatosensory (S1). Arrow, CD68 inside of microglia. Scale bar: 10 µm.

To gain insights on the morphological changes, we subtracted the control bootstrapped persistence image with the 2-week recovery (**Fig. 41**). The recovery-associated microglia displayed more short processes closer to but not emanating from the soma, pointing towards a hyper-ramification. Overall, the combination of our reference atlas and MorphOMICs allows to obtain first insights into microglial morphology and their functional response.

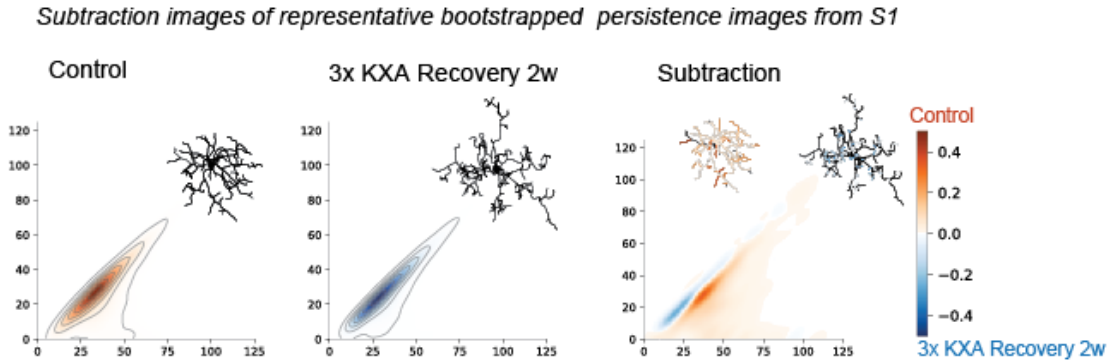

Fig. 41. MorphOMICs applied to KXA treated microglia. Representative persistence images corresponding to control and 3× KXA_{2w} centroid from (**Fig. 40A**) with color-coded process density. Top right corner, representative traced microglia. Subtraction image with highlighted overrepresented processes on the representative microglia.

5 Conclusions

In this study, we analyzed heterogeneity and sexual dimorphism of microglia morphology across seven brain regions from a total of 41,872 cells through development, disease, and under repeated anesthetic ketamine exposure and recovery (**Ext. Data Table 1**). To establish a reference atlas of morphological phenotypes, we developed and applied the MorphOMICs pipeline, which extracts the information of the entire reconstructed microglial tree in a minimally biased way, combined with variability reduction and data visualization.

MorphOMICs takes advantage of applied topology and preserves the intrinsic properties of the reconstructed morphological tree avoiding feature-selection-derived biases. Contrary, classical morphometric classifiers include only user-selected features and it has been an open debate which classifier reliably describes the morphological phenotype of microglia. Recent studies have explored the options of alternative machine learning paradigms to identify phenotypic differences, however, they rely on *a priori* labelled datasets and/or morphological feature selection [128,131,145]. MorphOMICs is independent of such assumptions. Furthermore, we

demonstrate that commonly-used morphometrics like process length, number of branches, terminal points or branching points failed to recapitulate subtle morphological changes, which separate populations (**Fig. 11**, **35A**). Due to interdependency of these parameters, we expanded the list to 27 diverse classifiers (**Ext. Data Table 4**) [208] and applied bootstrap and dimensionality reduction, but even these parameters were insufficient to resolve differences in microglia morphology in CK-p25 (**Fig. 37B**), 5xFAD (**Fig. 36A**), or postnatal development (**Fig. 36B**). Similarly, Sholl curves could not fully recapitulate the spatial heterogeneity, and the radius step size influences the readout (**Ext. Data Fig. 7B-C**). Interestingly, we found that both long primary- and short terminal processes contain information that contribute to the microglial spectrum (**Fig. 37A-D**) emphasizing the importance of retaining as many features as possible. Classical morphometrics and Sholl curves are suboptimal for this.

Brain region-specific single-cell transcriptome analysis have pointed towards microglial functional heterogeneity [68,69,209], but morphological differences have so far been difficult to identify. MorphOMICs revealed that microglia in an adult brain exhibit regional heterogeneity (**Fig. 17**) that exists already in early postnatal development (**Fig. 22B**) and diminishes during degeneration (**Fig. 28**, **32C**). Although microglia display a phenotypic spectrum (**Fig. 38, Fig. 39**), they respond to diseases in a brain region-dependent manner. Moreover, we confirmed that a sex-specific phenotype exists, which has long been debated [90,187]. This effect is rather mild during adulthood (**Fig. 18B**) but prominent during development (**Fig. 23**) and degeneration (**Fig. 29A**, **33A**). Both degeneration models showed a sexually dimorphic microglial response, which was pronounced in the immediately affected brain regions. Females showed an earlier shift along the morphological spectrum compared to males. This supports studies that have suggested a sex-dependent difference in Alzheimer's disease progression [198–200] and points to females having a higher risk of developing dementia [210,211].

Estrogens have been shown to be involved in the masculinization of the brain [187,212,213], and microglia are suspected of playing a role in this process [187,212]. Surprisingly in the ovariectomized females, microglia are distinct from their non-ovariectomized counterparts and the brain regions intermingled differently (**Fig. 18C**). Whereas ♀FC_{mg} and ♀OB_{mg} occupied a similar cluster in control adults, ♀$_{ov}FC_{mg}$ were distinct from ♀$_{ov}OB_{mg}$ and highly intermingled with ♀$_{ov}SN_{mg}$ (**Fig. 18C**), suggesting that the impact of estrogens on microglial morphology is complex. Overall, MorphOMICs links the previously reported sexually dimorphic microglial

transcriptome in the healthy brain [84,85,89,214] and in degeneration models [91,96,100,215–217] with a distinct morphological phenotype.

We showed that MorphOMICs detects microglial morphological changes at high resolution in several physiological conditions deviating from adult controls. For example, microglia shifted at P15 from the P7/P22 trajectory across all brain regions (**Fig. 25**). This is the time of circuit refinement, where microglia have frequently been shown to participate in synaptic pruning [192,193,218,219]. Another synapse-associated pattern occurred in the DG_{mg} of CK-$p25_{2w}$ (**Fig. 34**). Unexpectedly, we found here the highest CD68 fold change and not within the CK-$p25_{6w}$, where we have observed the most distinct morphological shift from the control. This discrepancy might be associated with previously observed transient p25 expression [153]. In general, we could associate CD68 upregulation with a diverse phenotype and has to be evaluated in a sex-, brain-region-, and context-dependent manner.

MorphOMICs provides the fundaments to track subtle morphological changes that can be important indicators of local environmental changes and interference with the neuronal network. Whereas we have not found any obvious changes in the microglia morphology upon repeated anesthetic ketamine or the recovery (**Fig. 40C**), MorphOMICs overcomes the ambiguity and strongly predicts a microglia response based on our reference atlas (**Fig. 40A**) that can be investigated in a targeted manner. MorphOMICs provides an advanced strategy for systematically comparing microglial populations across different brain regions and conditions: this could be expanded infinitely. Future studies will focus on identifying informative regions of a persistence barcode, which provides a perspective for morphological analysis of lower-resolution images, such as *in vivo* microglial imaging for potential non-invasive diagnostic applications. Stable ranks would provide a mathematically robust approach to address this question, as we have shown that standard stable ranks of the TMD captured the microglial phenotypes (**Ext. Data Fig. 6C**, **11A**) as well as the persistence images of the microglial TMD (**Fig. 17**). A critical point to consider is the number of cells that are needed for MorphOMICs. While we identified a suitable bootstrap size in **Ext. Data Fig. 4**, the condition-specific variability in microglial morphology needs to be systematically assessed to determine the minimum cell number before MorphOMICs can be reliably applied.

1. Supplementary text

Computational assessment of bootstrapping methods in MorphOMICs

1. Single-condition case

Microglia are highly dynamic [220], a feature which is inherent to their function. Under homeostatic conditions, microglia survey their local environment for insults and anomalies. This intrinsic variability challenges the topological analysis of microglial morphology as we observed in the corresponding persistence images of single microglia (**Fig. 12**). This variability can mask heterogeneity between microglial populations from different biological conditions *e.g.*, brain region, sex, and development and disease time point (**Ext. Data Fig. 1**).

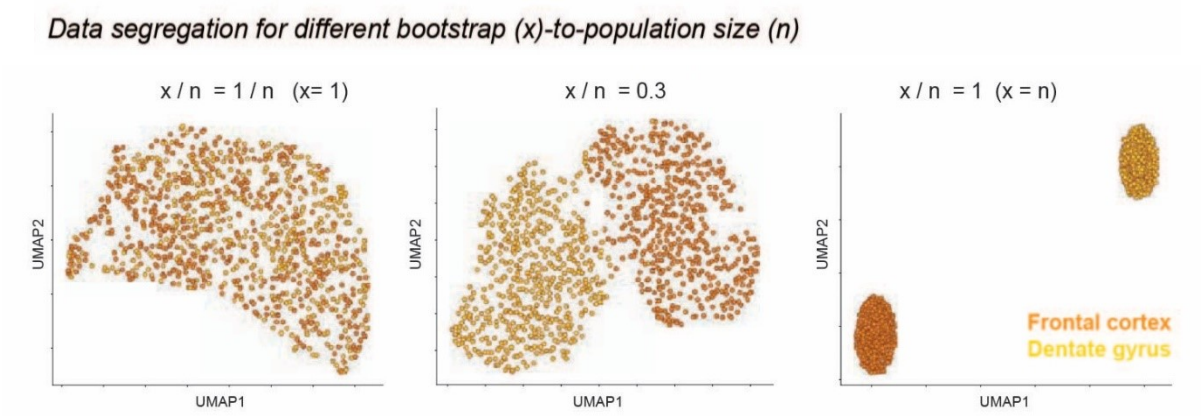

Extended Data Figure 1. Details about the MorphOMICs paradigm. UMAP plots of MorphOMICs-analyzed microglia for frontal cortex (orange) and dentate gyrus (yellow) for different bootstrap-to-population size ratios. Left: x=1, allows no segregation. Middle: x/n=0.3. Right: x/n=1 causes accentuation.

To overcome this intrinsic variability within microglial populations, we use bootstrapping methods. Bootstrapping is a statistical method that combines random resampling and permutation. It is commonly used to calculate standard errors, to construct confidence intervals, and to perform hypothesis testing for numerous types of sample statistics. In our case, we used bootstrapping to randomly pool together a pre-determined number of microglia within a condition, called the bootstrap size, to reduce the dispersion. This allowed us to construct a bootstrapped persistence image of this microglial sub-population. By averaging out the highly variable portions of the persistence images, we retain the topological signatures that may separate different conditions. Moreover, bootstrapping makes it possible to create as many bootstrapped persistence images as desired.

The pixels of the persistence image span a high-dimensional space. The bootstrapped persistence images form a point cloud in this high-dimensional space with the average persistence image in the center (**Ext. Data. Fig. 2**). Thus, the spread of this cloud allows us to

assess the variability within a microglial population. Intuitively, the bootstrap size affects this point cloud size. To construct the bootstrapped persistence images with just a single microglia will give us the largest cloud as it reflects the full size of the population's dispersion. On the other hand, when the bootstrapped persistence image is constructed using all of the microglia, the cloud collapses to a single point as there is no difference between the bootstrapped persistence images and the average persistence image.

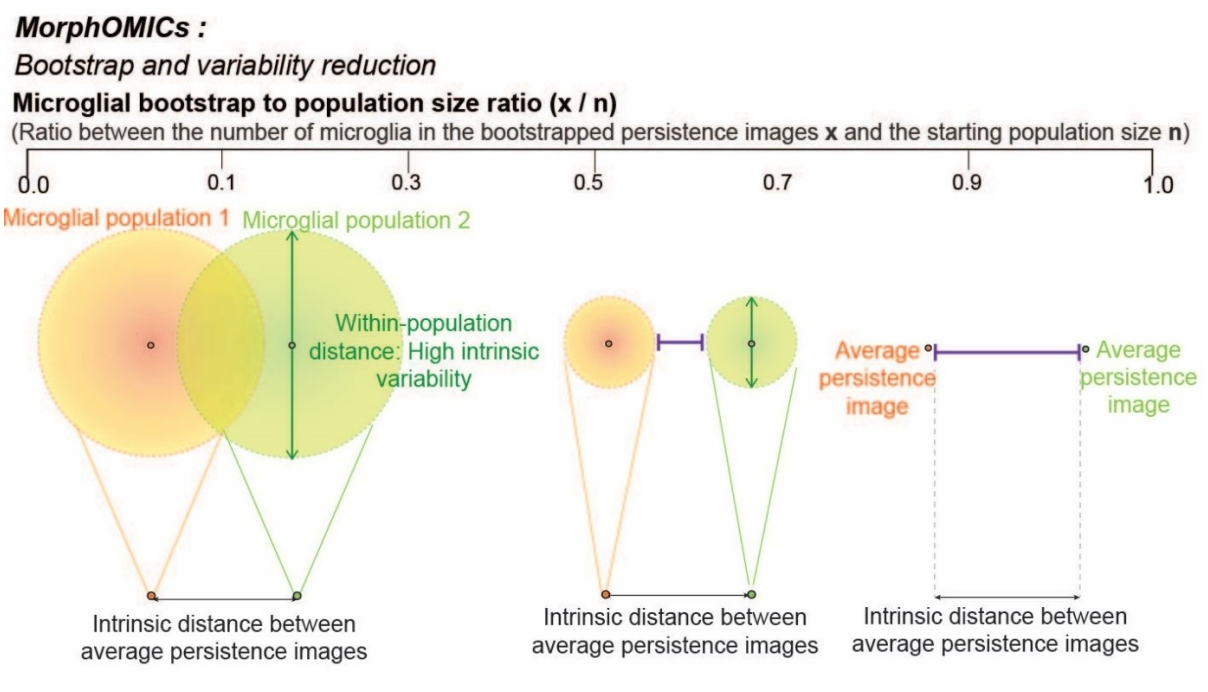

Extended Data Figure 2. Details about the MorphOMICs paradigm. Schematic of the bootstrapping effects on the distance between tree structures from the same population (within-population distance, green arrows) and two distinct populations (distance between average persistence images, purple lines). Increase of bootstrap-to-population size ratio (x/n) reduces within-population distance and increases distance between average persistence images.

To systematically understand the effect of the bootstrap size on the structure of the point cloud formed by the bootstrapped persistence images, we considered a population composed of a high number of traced microglia, namely the microglia of the adult, healthy dentate gyrus. This allowed us to span a range of sizes for the starting population from which we performed the bootstrapping. As we observed no animal-specific batch effects (**Fig. 15B**), we selected four mice with the highest number of tracings, and grouped them into two artificial groups (A and B) so that the number of single cells were similar in each group ($N_A = 223, N_B = 231$). Despite coming from the same brain region, these two groups have a non-zero TMD distance ($d = 10.64$) which we call the TMD intrinsic distance. This intrinsic distance arises due to small but accumulated variations in the persistence images. To account for the effect of unequal starting population sizes between the groups, we randomly selected $n = 200$ traced microglia

from each group to form the starting population. We then drew single microglia from these groups to create a set of bootstrapped persistence images, which we call bootstrap samples A and B. Note that the TMD intrinsic distance remains the same, regardless of the bootstrap size (**Ext. Data. Fig. 2**).

To characterize the point cloud formed by the bootstrapped persistence images, we calculated the within-condition distance which is the average TMD distance between two persistence images within the same bootstrap sample. We want to stress here that the two conditions A and B are artificial: the bootstrap persistence images in bootstrap samples A and B come from the same brain region. We observed that reducing the bootstrap size compacted the point cloud and subsequently reduced the within-condition distance within the bootstrap sample (**Ext. Data. Fig. 3**). At a certain bootstrap-to-starting population size ratio where $N_A = N_B = 200$ the within-condition distance becomes smaller than the TMD intrinsic distance. This implies that the between-condition distances, *i.e.* the TMD distance between persistence images across different bootstrap samples, increases causing a forced separation between two groups from the same condition.

Thus, it is imperative to select a bootstrap size which reduces the dispersion of the bootstrap samples without artificially separating samples that share topological signatures. One way to address the latter condition is to determine whether the bootstrap samples A and B cluster separately under a given bootstrap size. To test this, we performed a complete-linkage hierarchical clustering with the TMD distance as the metric. We imposed a cut-off which results in two clusters, ω_1 andω_2. We then defined a mixing entropy of the resulting clusters $\Omega = \{\omega_1, \omega_2\}$ which measures the discrimination between bootstrap samples and is calculated as

where $H[\omega] = \frac{N_A(\omega)}{N_\omega}\log_2\frac{N_A(\omega)}{N_\omega} - \left(1 - \frac{N_A(\omega)}{N_\omega}\right)\log_2\left(1 - \frac{N_A(\omega)}{N_\omega}\right)$ is the entropy of clusterω, $N_A(\omega)$ is the number of bootstrapped persistence images in bootstrap sample A located in cluster ω and $N = N_{\omega_1} + N_{\omega_2}$ is the total number of bootstrapped persistence images in the point cloud. To understand this mixing entropy, we considered both extreme situations. The first case is when bootstrap samples A and B overlap and the point cloud is highly dispersed: this results in a big cluster with all persistence images aggregated except for one. The latter is

the last bootstrap persistence image to be clustered in the dendrogram, and the mixing entropy is close to 1. On the other hand, when the point cloud dispersion was small enough for bootstrap samples A and B to segregate, the clustering resulted in separate clusters for samples A and B, and the mixing entropy is zero. Note, the latter emerges whenever we force the separation between two similar-condition groups.

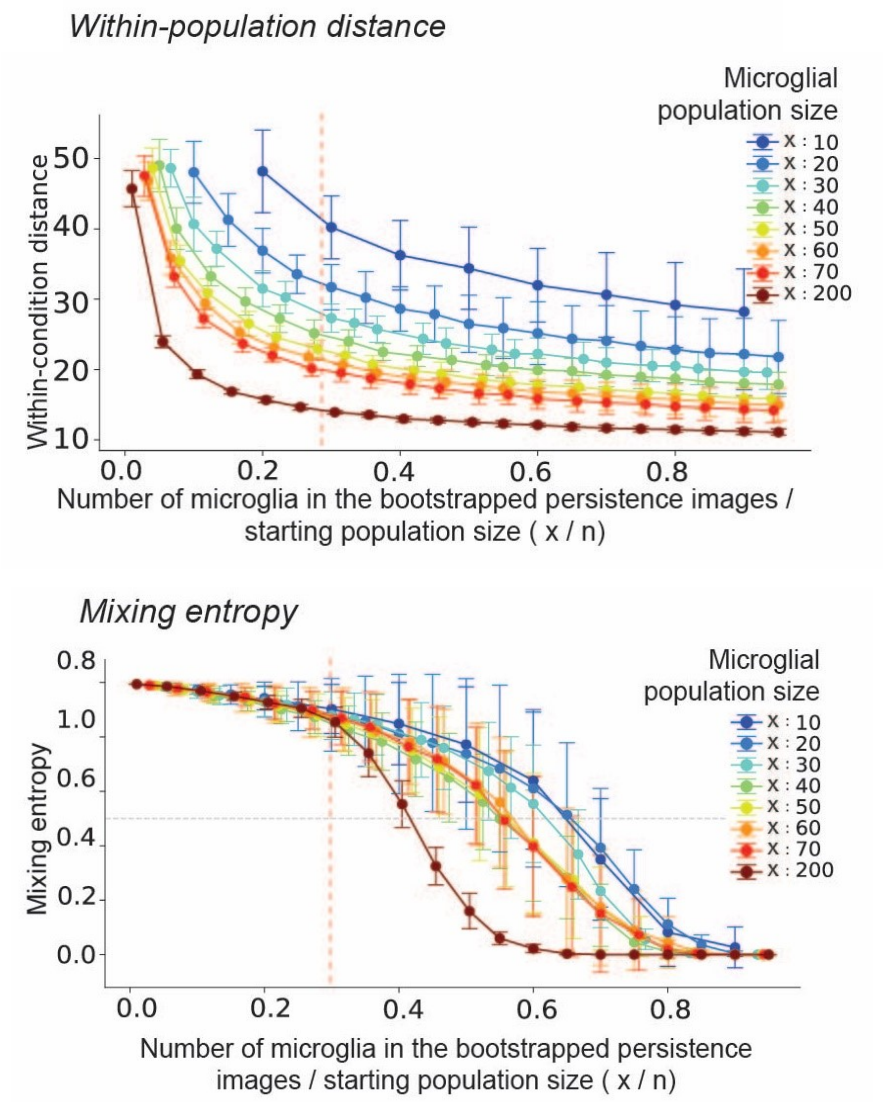

Extended Data Figure 3. Details about the MorphOMICs paradigm. Line plot ± SD displays how within-population distance (top) and mixing entropy (bottom) decrease with enhanced bootstrap-to-population size ratio (x/n). An empirical threshold of 0.3 was selected (red dashed line).

If we also consider the situation between the two extreme situations, the mixing entropy decreases with increasing bootstrap-to-starting population size ratio (**Ext. Data. Fig. 3**). We observed that the mixing entropy remained close to 1 for a range of small ratios and then dropped to zero, depending on the starting population size. This behavior allows us to define

an optimal bootstrap size which maximizes the trade-off between the intrinsic variability of the bootstrap samples and the indistinguishability of samples coming from the same conditions. By dividing the mixing entropy with the within-condition distance, we found a peak close to a bootstrap size that is 30% of the starting population size (**Ext. Data. Fig. 4**).

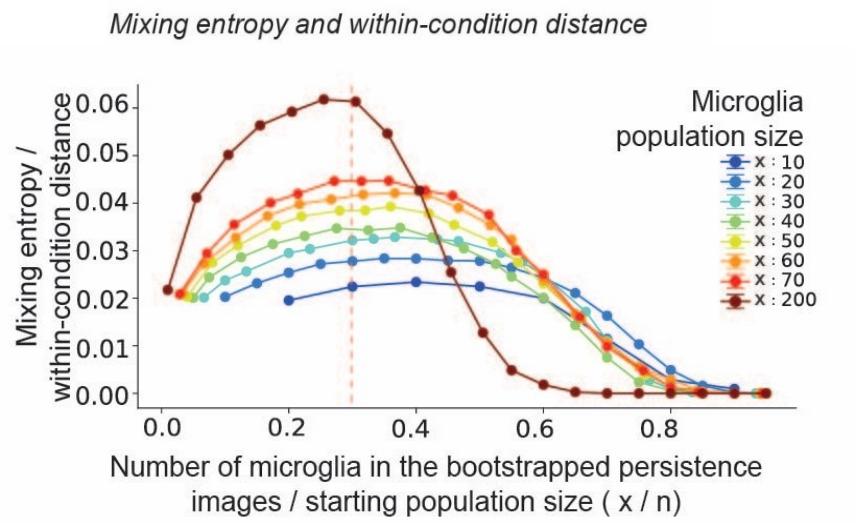

Extended Data Figure 4. Details about the MorphOMICs paradigm. Line plot ± SD displays how the ratio between mixing entropy and within-condition distance varies by enhancing the bootstrap-to-population size ratio (x/n).

Furthermore, we assessed the effect of low starting population sizes on both the within-condition distances and mixing entropy. Thus, we randomly selected $n = \{10, 20, 30, 40, 50, 60, 70, 80\}$ microglia from each group and performed the bootstrapping over the resulting starting populations. We found that both within-condition distance and mixing entropy decreased as a function of the bootstrap size, but dependent on the starting population size (**Ext. Data. Fig. 3**). Interestingly, when we divided the mixing entropy by the within-condition distance, we observed that there was no longer a well-defined optimal bootstrap size (**Ext. Data. Fig. 4**), and that the optimal ratio is a range of parameters which is larger for samples with a low starting population size.

2. Multiple-condition case: sexual dimorphism in the frontal cortex and dentate gyrus

In the analyses above, we only considered the situation where two groups come from the same condition, such as microglia from the adult male dentate gyrus. Here, we look at a situation where we have multiple conditions which not only exhibit spatial but also sexual heterogeneity.

We focused on microglial populations coming from the healthy, adult frontal cortex (FC) and the dentate gyrus (DG) where we see a microglial signature and a region-dependent sexual dimorphism. Thus, we took 75 microglia from the four male and four female mice with the highest number of traced microglia in the frontal cortex and dentate gyrus. To investigate the

effect of having unequal proportions of male and female microglia in the sample, we created starting populations with size $N = 200$ where the male-to-female microglia ratio, $r = \{0.0, 0.1, 0.2, \ldots, 0.8, 0.9, 1.0\}$ was fixed. For each brain region and male-to-female ratio, we constructed bootstrap samples with bootstrap-to-starting population size ratio at 0.1, 0.3, 0.5, 0.7, and 0.9. As there are multiple conditions, we looked at the 2D UMAP representations for each bootstrap size using the same parameters in the main text.

We observed that at 0.1 size ratio, the difference in the morphological signature between FC and DG microglia is already apparent (**Ext. Data. Fig. 5**), and that within a brain region cluster, the pure male and female samples are located at opposite ends. These ends in the DG_{mg} cluster tend to come closer together than those of the FC_{mg}. Note that these observations are captured when the bootstrap-to-starting population size ratio is at 0.3.

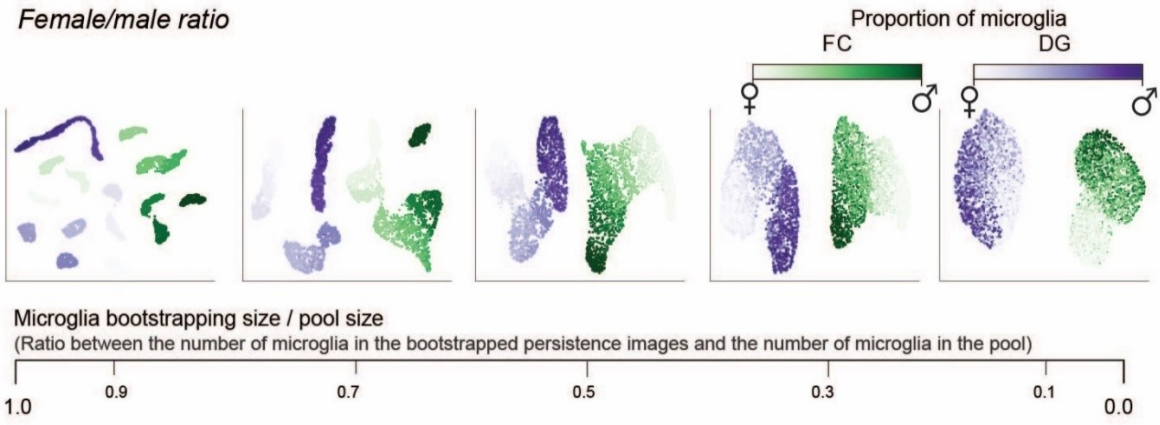

Extended Data Figure 5. Details about the MorphOMICs paradigm. **E:** UMAP plots of MorphOMICs-analyzed microglia for frontal cortex (green) and dentate gyrus (purple) for different bootstrap-to-population size ratios and varying male-to-female ratios within the population size.

Finally, we observed that as the bootstrap size increased, samples with different male-to-female size ratios broke apart, suggesting a forced separation between different conditions. However, the rate at which the different conditions became more distinct was not uniform. Indeed, we saw that the male-dominated samples in the DG_{mg} still form a cluster at bootstrap-to-starting population size ratio 0.9, which implies that $♂DG_{mg}$ have "stronger" and less variable microglial signatures than their female counterparts. This suggests that spanning a range of size ratios can uncover information on the intrinsic variability.

1. Extended Data material

Extended Data Figure 6

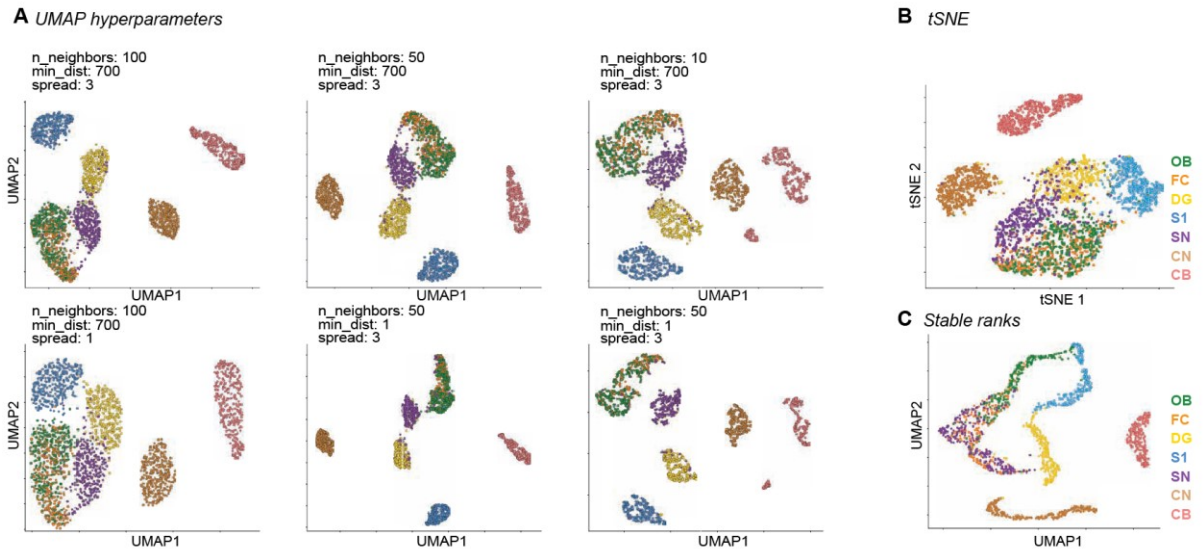

Extended Data Figure 6. Details about the MorphOMICs paradigm. A: UMAP plots of MorphOMICs-analyzed microglial morphology across seven brain regions as shown for **Fig. 17** with examples of tested hyperparameters for number of neighbors (n_neighbors), minimum distance (min_dist), and spread. Olfactory bulb (OB), frontal cortex (FC), dentate gyrus (DG), somatosensory cortex (S1), substantia nigra (SN), cochlear nucleus (CN), and cerebellum (CB). **B:** tSNE plot of MorphOMICs-analyzed microglia across seven brain regions as shown in **Fig. 17**. **C:** UMAP plots of stable ranks representation of microglial morphology (see Methods: Stable Ranks) across seven brain regions. SD: standard deviation.

Extended Data Figure 7

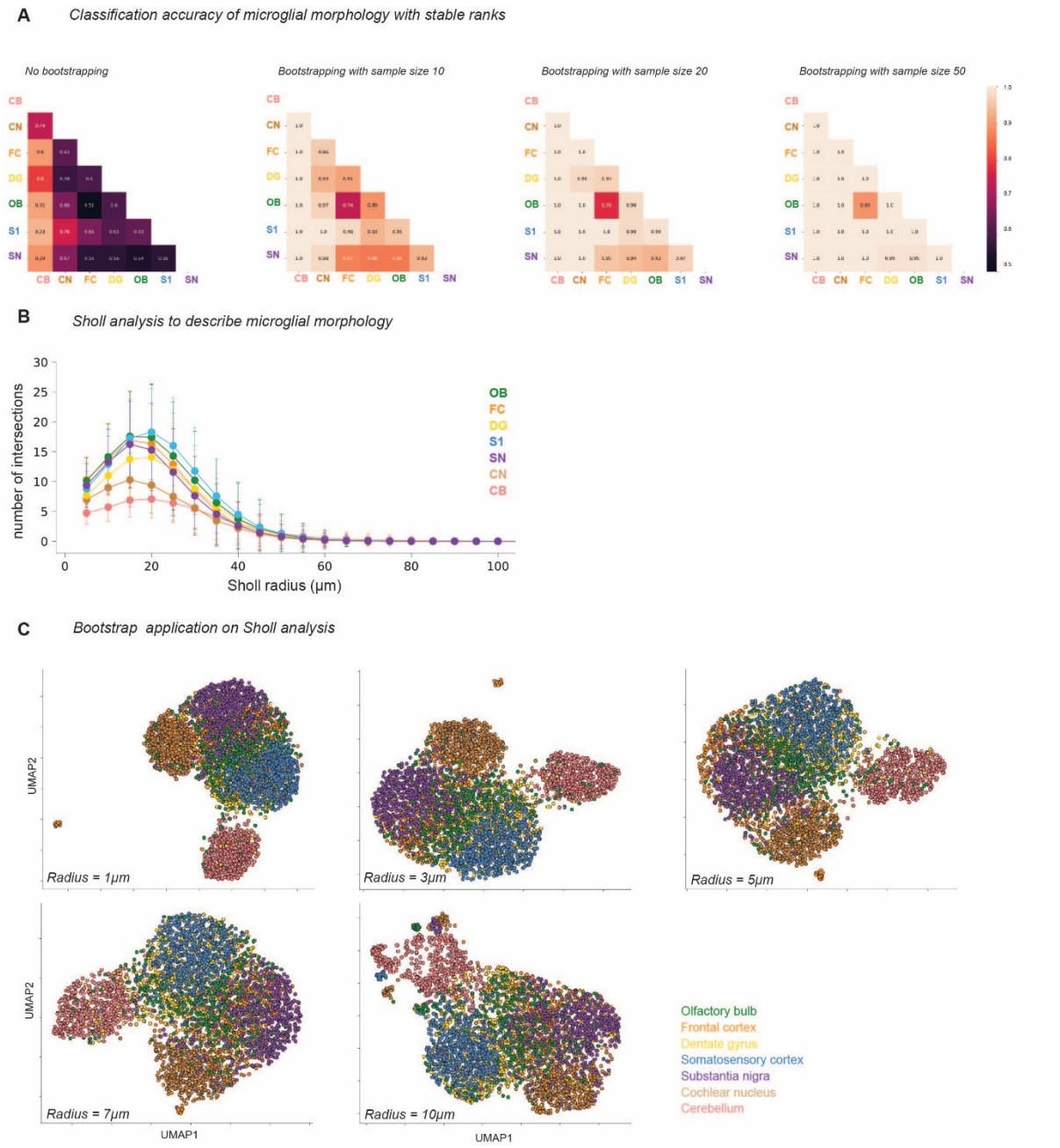

Extended Data Figure 7. Classification accuracy of microglial morphology and bootstrap application on Sholl analysis. A: Heat-map of classification accuracy between pairs of brain regions using stable ranks for different bootstrap sizes. Numbers indicates the percentage of microglia correctly assigned in the classification task, averaged over 10 repeated cross-validations. 1, perfect assignment; 0.5 random assignment. **B:** Sholl curves for each brain region showing the average number of processes ± SD that intersect with a series of concentric Sholl spheres centered on the soma and spaced at 5 µm. **C:** Bootstrapped and UMAP visualized Sholl-analyzed microglia, color-coded for each brain region. Each dot represents a bootstrapped Sholl analysis. Each plot has a set radius step size (1, 3, 5, 7, 10 µm). Olfactory bulb (OB), frontal cortex (FC), dentate gyrus (DG), somatosensory cortex (S1), substantia nigra (SN), cochlear nucleus (CN), and cerebellum (CB). SD: standard deviation.

Extended Data Figure 8

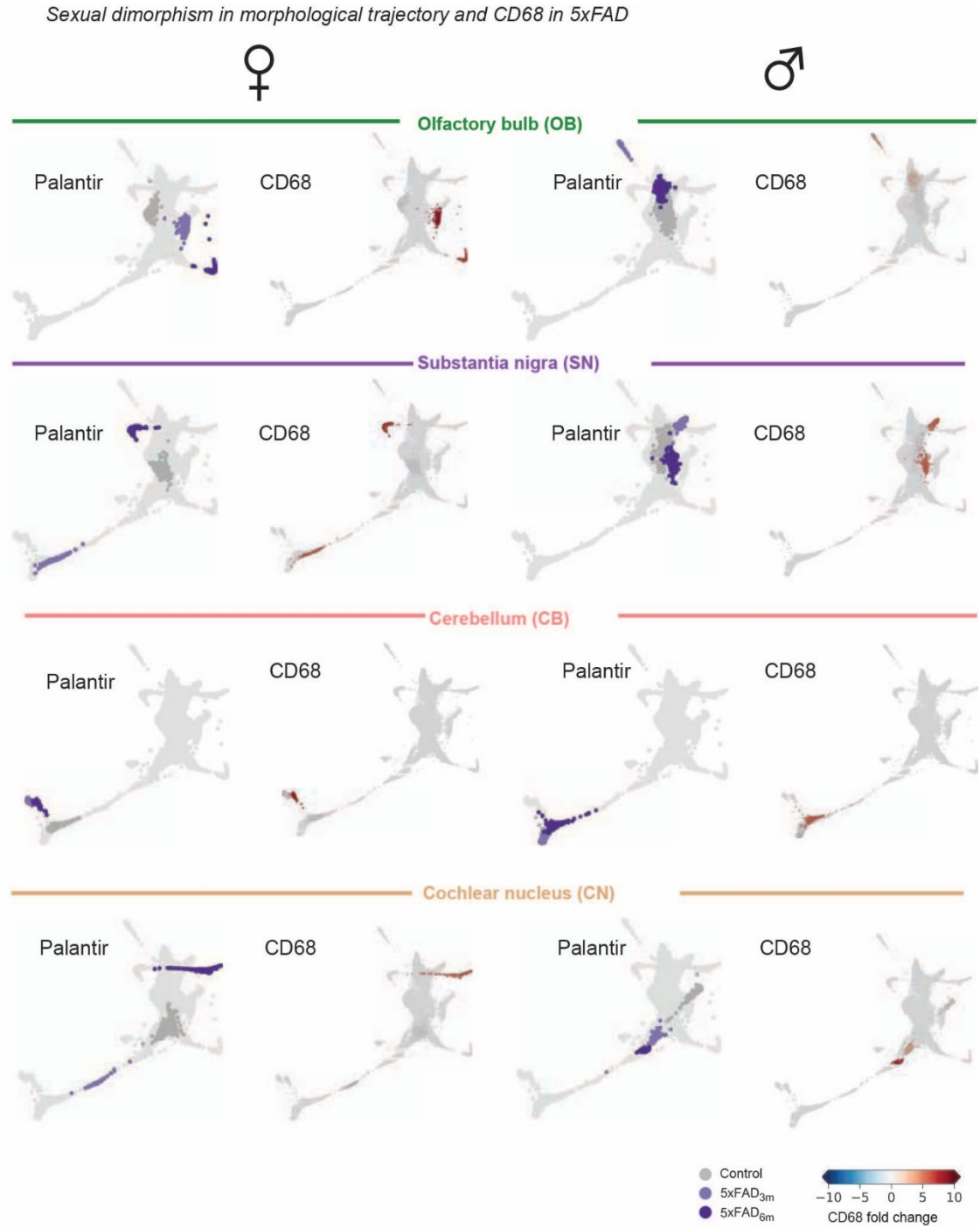

Extended Data Figure 8. Sexually dimorphic microglia phenotype in 5xFAD. **B:** Palantir reconstruction of microglial trajectory with corresponding color-coded CD68 fold change next to it for females (left) and males (right) in control adult, 5xFAD$_{3m}$, and 5xFAD$_{6m}$ of OB, SN, CN, and CB. Fold change: blue < 0; red > 0. Olfactory bulb (OB), frontal cortex (FC), dentate gyrus (DG), somatosensory cortex (S1), substantia nigra (SN), cochlear nucleus (CN), and cerebellum (CB).

Extended Data Figure 9

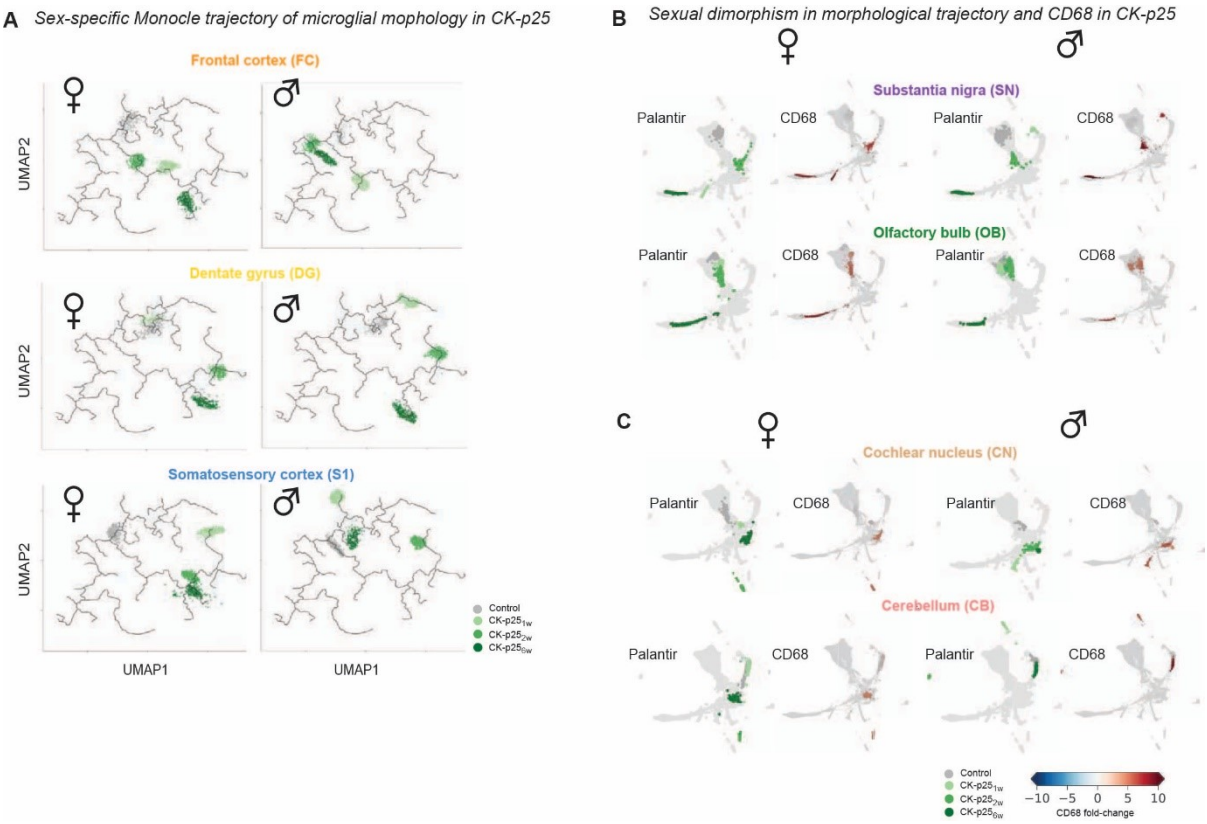

Extended Data Figure 9. Sexually dimorphic microglial phenotype in CK-p25. A: Monocle reconstruction of microglia trajectory of females (left) and males (right) in control, adult and CK-p25 mice FC, DG, and S1. **B-C:** Palantir reconstruction of microglia trajectory and corresponding color-coded CD68 fold-change of females (left) and males (right) for SN, OB (**C**) and CN, CB (**D**). Fold change: blue < 0; red > 0.

Extended Data Figure 10

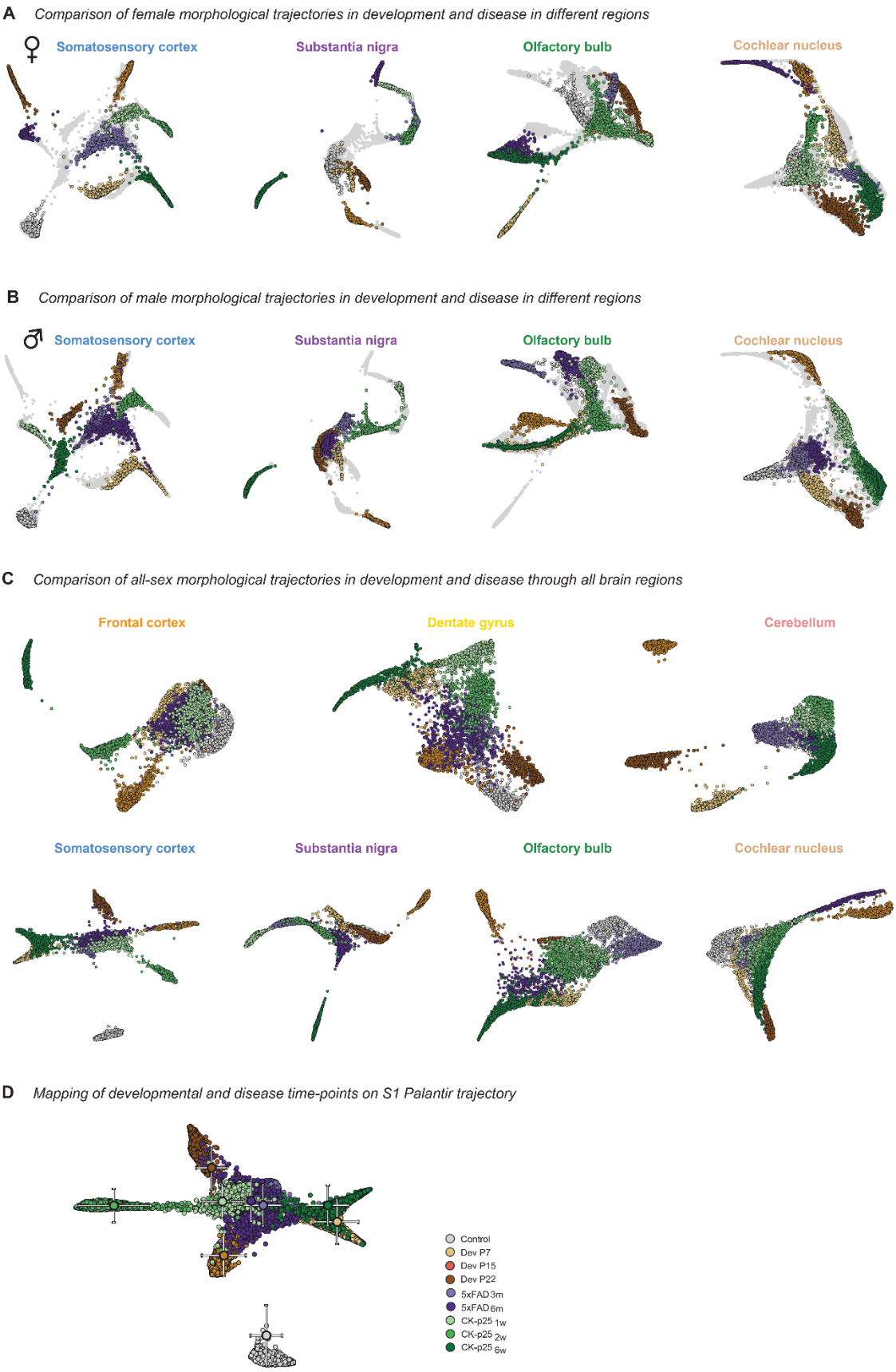

Extended Data Figure 10. Integration of development and disease phenotypes into microglial reactivity

spectrum in secondarily affected brain regions. A-B: Palantir reconstructions of microglia trajectory in females (**A**) and males (**B**) for S1, SN, OB, and CN in control, P7, P15, P22, CK-p25$_{1w}$ (1-week), CK-p25$_{2w}$ (2 weeks), CK-p25$_{6w}$ (6 weeks), 5xFAD$_{3m}$ (3 months), and 5xFAD$_{6m}$ (6 months) conditions. Each brain region is highlighted in a separate Palantir plot. **C-D:** Reference atlas for each brain region represented as Palantir reconstruction containing both sexes. **D:** Mapping of S1 microglial morphology on Palantir trajectory. Centroids indicating the mean position of mapped points in a given condition with the corresponding standard deviations.

6 MorphOMICs dissects sex-dependent microglia morphology in the retina

6.1 Introduction

The retina is a highly specialized neuronal tissue responsible for processing incoming light information into visual signals [221]. It originates as an outgrowth of the embryonic diencephalon in the developing brain [222] and outlines a well-defined brain region (**Fig. 42**). The retina is compartmentalized in three nuclear layers: the outer nuclear layer (ONL) with the light-sensing photoreceptors; the inner nuclear layer (INL) that contains horizontal-, bipolar-, and amacrine-cells that process the incoming light information; and the ganglion cell layer (GCL), which takes the information and outputs it to visual processing brain regions such as the lateral geniculate and the superior colliculus [223,224]. The cell types connect in two distinct synaptic layers: the outer plexiform layer (OPL), where photoreceptors make contacts with cells in the INL, and the inner plexiform layers (IPL) that forms synapses between cells in the INL and GCL. The retina contains also two types of inhibitory cell classes: the horizontal cells and the diverse amacrine cell class that modulate signal transmission in the OPL and IPL, respectively. Similar to other brain regions, glial cells populate these neuronal network. The most abundant glial cell type in the retina is the Müller glia, which spans through the entire retina and is involved in trophic and anti-oxidative support of photoreceptors [225]. Astrocytes are mostly localized in the neuronal fiber layer below the GCL [226]. Microglia comprise approximately 0.2% of the retinal adult cell population [227]. In physiological conditions, they mostly occupy the OPL and the IPL.

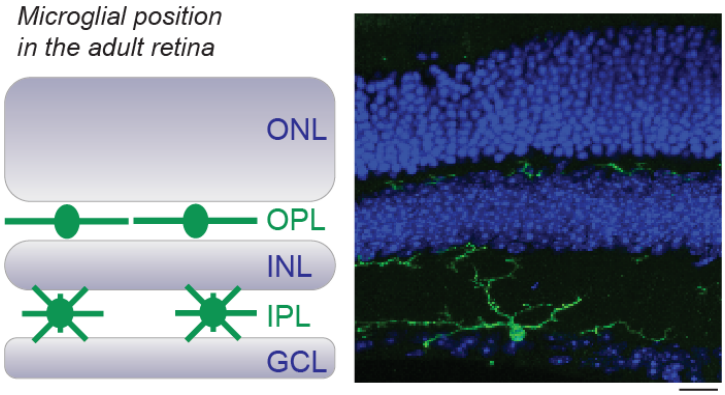

Fig. 42. Side-view of the retina. Left: schematic. Right: confocal image of vibratome section through the mouse retina immunostained for microglia (Iba1, green) and the nuclei-dye Hoechst (blue). ONL, outer nuclear layer. OPL, outer plexiform layer. INL, inner nuclear layer. IPL, inner plexiform layer. GCL, ganglion cell layer. Scale bar: 20 µm.

6.2 Microglia in their niches

The OPL and IPL exposes the microglia to different local microenvironments that influence their function [13] (**Fig. 43**). As an example, in physiological conditions IPL_{mg} depend on IL-34 to a much greater extent than OPL_{mg} for their survival, as IL-34 depletion selectively reduces IPL_{mg} [228]. During pathologies, microglial show spatial dependent response, e.g. leads an optic nerve injury to a predominant reactivity in microglia in the IPL (IPL_{mg}) whereas photoreceptor degeneration strongly affects microglia in the OPL (OPL_{mg}) [229,230]. Microglial diversity in OPL and IPL provides a clear example of microglial heterogeneity within one brain region.

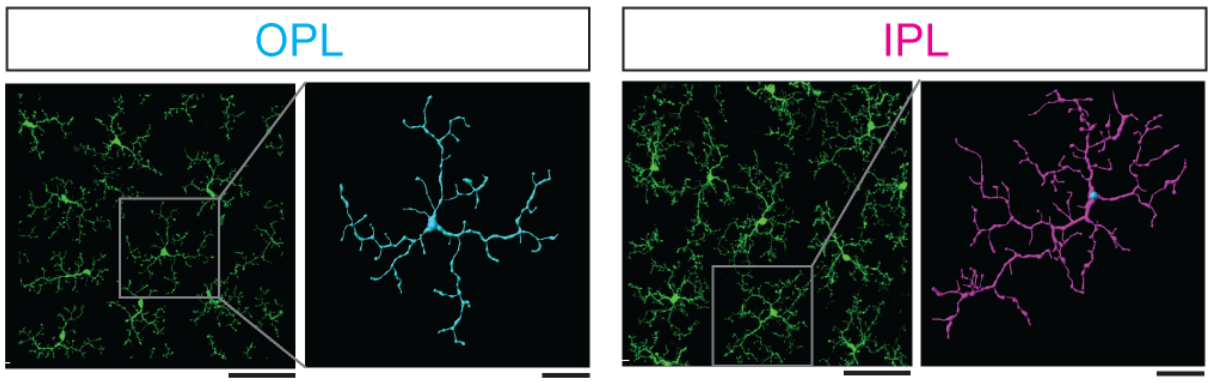

Fig. 43. Microglia in OPL and IPL. Confocal images of whole-mount retinas of adult $Cx3cr1^{+/GFP}$ mice immunostained for GFP (microglia, green). Image cropped to show either OPL (left) or IPL (right). Scale bar: 50 µm. Next, zoom-in of filament reconstructed microglia of either OPL (cyan) or IPL (magenta). Scale bar: 20 µm.

In the following sections, I am providing an overview of the current knowledge about retinal microglia with a focus on their role during development, in healthy adult, in a genetic model of photoreceptor degeneration and after optic nerve injury.

6.3 Microglia sculpt the developing retina

Microglia colonize the developing mouse retina before birth from E11.5 onwards [229,231]. They infiltrate in two waves: The first wave takes place embryonically and precedes vascularization.

Microglia migrate through the vitreous and non-neuronal ciliary regions following a vitreal-to-scleral direction [229]. The second wave occurs around birth, when microglia infiltrate through the optic disc and the forming retinal blood vessels [227,229]. Immediately after birth, microglial cells are mostly seen in the GCL and IPL, where they contact the immature synaptic contacts [227]. Then, they migrate and colonize the OPL as soon as neuronal migration establishes the ONL structure [232]. During the postnatal retinal development, microglia refine synapses, prune weak connections, target and remove apoptotic cells [233]. In the first two postnatal weeks, microglia display altered density, morphology and increased phagocytic function compared to adult. Microglia density peaks postnatally with the second migration wave and then gradually decreases from P7 onwards reaching a stable number by P30 when synapse maturation is completed [229]. Microglia regulate neuronal differentiation during retinal development as microglia ablation with PLX-5622 delays neurogenesis and neural differentiation [234], and selective CSF1R KO causes a transient increase in ganglion cell number [235]. Morphologically, microglia exhibit an immature morphology with short and thick processes, resembling an amoeboid-like morphology. After microglial cells reach a plexiform layer, they progressively ramify. This morphology remains stable in the absence of any detrimental stimuli [227].

6.4 Microglia maintain retinal functionality in adults

After retinal development at P30, microglia are a self-sustaining population with low basal turn-over rate [228,236]. Microglial homeostasis is tightly regulated by constitutive signals, which arise from surrounding neurons and are sensed through microglia-specific receptors like CSF1R and CX3CR1 [237]. The CSF1R pathway is necessary for microglial survival [238], while neuronal CX3CL1 signaling regulates the physiological state of retinal microglia via CX3CR1. Loss of CX3CR1 in microglia causes aberrant microglial activation and responses in retinal injury models [239–241]. Although a lot is known about microglia response to environmental insults, microglial function in healthy adulthood has not been completely understood [242]. Long term depletion of retinal microglia lead to a progressive functional deterioration in light response suggesting that microglia are required to maintain synaptic function and integrity also in the mature retina [243].

6.5 Microglia respond to different models of retinal degeneration

Retinal degeneration has severe impacts on vision as losing the light-sensing photoreceptors or the ganglion cells, both processing the light information for the brain, leads to blindness. Several models have been developed to recapitulate the disease onset and progression from the neuronal perspective. One model focuses on *retinitis pigmentosa*, a hereditary eye disease causing photoreceptor degeneration. In human, this disease typically starts with the loss of night vision in adolescence, side vision in young adulthood, and central vision in later life because of progressive loss of rod photoreceptor cells [244]. Another common model focuses on optic neuropathy. Glaucoma is an umbrella term of progressive optic neuropathies characterized by degeneration of retinal ganglion cells and optic nerve lesions, often linked to increased ocular pressure [245]. Optic nerve mechanical lesion recapitulates part of this phenotype and is therefore a widely used model to study these pathologies [246].

Both disease models have in common the loss of visual function and microglial reactivity, yet rd10 mostly target photoreceptor and ONC primarily damages RGCs [246,247]. The diverse degeneration models available provide the opportunity to evaluate microglia layer-specific morphological differences.

6.5.1 Photoreceptor degeneration with the rd10 mouse model

The CXBl-Pde6brd10/J mice line (rd10) describes a model for *retinitis pigmentosa*. These mice carry a missense point mutation in Pde6b, which encodes for cGMP phosphodiesterase 6B. This enzyme is involved in the photo transduction cascade of rod photoreceptors [248–251]. After 2-3 weeks postnatal, rod photoreceptors in rd10 mice start to degenerate with a peak in death and subsequent thinning of ONL at around P25. This is followed by a secondary degeneration in the INL primarily affecting bipolar cells (**Fig. 44**) [247]. Rd10 is considered a mild model of neurodegeneration since a scattered population of aberrant cones persists for up to 9 months of age together with some light response [247].

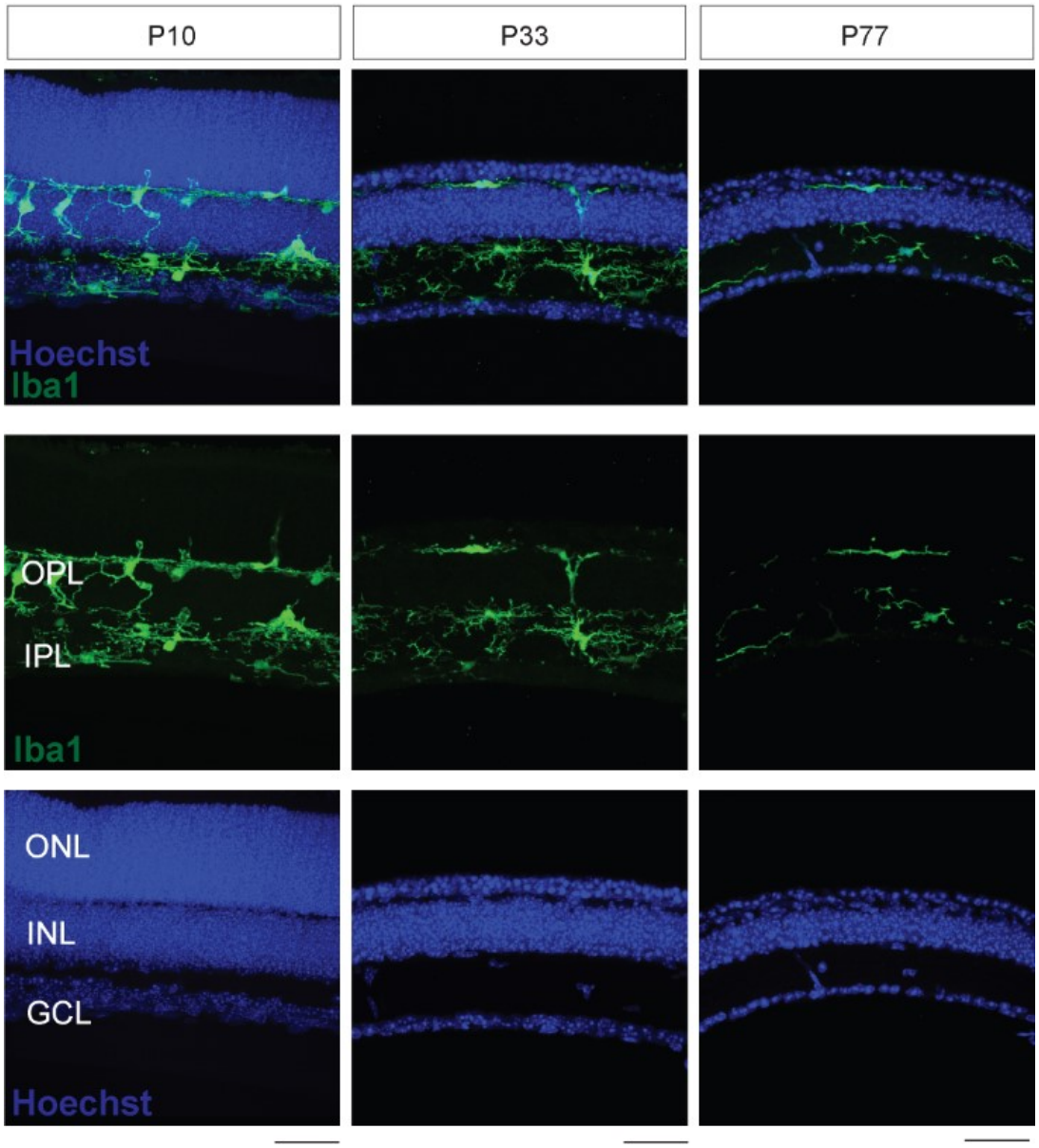

Fig. 44. Rd10 degeneration. Confocal images of retinal vibratome sections in rd10 mice at different postnatal (P) days. Green: microglia immunostained with Iba1. Blue: nuclei-dye Hoechst. Scale bar: 30 µm.

The retina is functionally mature from ~P30 [252]. Thus, the peak of the photoreceptor degeneration does not overlap with the retinal maturation. During rd10 degeneration onset, degenerating rod photoreceptors recruit microglia through neuronal apoptotic signals like CX3CL1 and CCL2 [253,254]. Recruited microglia migrate to ONL where they phagocytose degenerating neurons and clean debris. This occurs in both mouse and humans [255]. During the process of phagocytosis, progressively lose their fine branches [247].

Microglial response in rd10 model of degeneration has both a protective and a toxic effect: Microglia exert neuroprotective effects via the CX3CL1/CX3CR1 pathway as suppression of this pathway increases vulnerability in the Rd10 model [240]. On the other hand, pharmacological inhibition of microglial activation or their depletion reduces photoreceptor apoptosis [255]. Overall, microglia are key contributors in rd10 neuronal degeneration, which makes them potential therapeutic targets.

6.5.2 Retinal ganglion cell degeneration with the ONC model

Optic nerve crush (ONC) is a well-established axonal injury model [256]. During ONC, axonal projections of RGC in the optic nerve are mechanically injured, without affecting the dura nor the blood vessel integrity [257] (**Fig. 45**). This induces retinal ganglion cell apoptosis and massive microglial response in the IPL [246,258]. Microglia peak response to the RGC apoptosis is around 5 days post crush [259]. Following the lesion, microglia associate to injured nerves and use them to migrate into the retina [260].

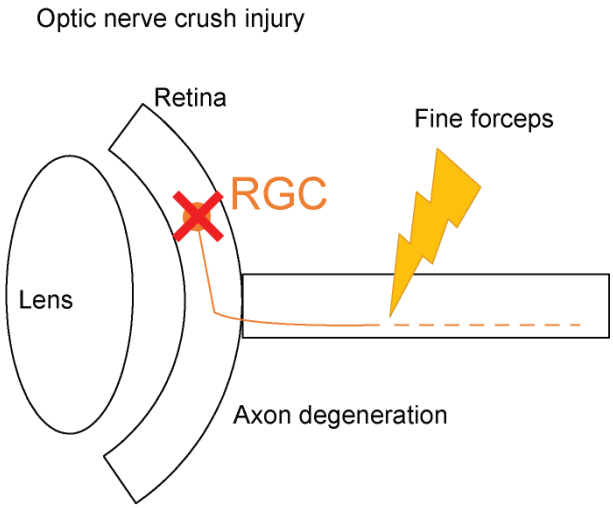

Fig. 45. ONC. *Schematic of the optic nerve crush (ONC) with a retinal ganglion cell (RGC) in orange. Fine forceps are used to apply pressure in the optic nerve causing axon degeneration and RGC loss.*

6.5.3 Morphological analysis of microglia in the retina

Morphological adaptations of microglia may inform on how microglia interact and influence retinal circuits. However, due to the lack of strategies to resolve the microglia morphological complexities, this read-out has not been extensively followed up. Only few studies specifically focused on retinal microglial shape. For example Ash and colleagues developed an automated segmentation algorithm to analyze retinal microglial morphology in a model of retinal degeneration [133], while in another work retinal microglia was classified into five morphological classes with a machine-learning approach and tracked their distribution over aging [136].

After successfully assessing microglial heterogeneity across different brain regions, we asked whether MorphOMICs also reliably detects differences within the retina. This would be interesting as the retina is an easily accessible brain region and tracking of microglial changes could help early diagnostics of many neurodegenerative diseases like PD, AD and MD. These diseases display retinal abnormalities before symptoms onsets with microglia as early responders [261]. Furthermore, we can further get insights about microglial morphology adaptations within a defined brain tissue in a layer-dependent manner that compromises a defined neuronal microenvironment.

7 Material and methods

Animals. Mice of both sexes and ages (4–17 weeks) were used. Founder animals were purchased from The Jackson Laboratory for the Pde6brd10/rd10 (004297) strain. All mice were backcrossed to the C57BL6/J background for at least 10 generations. Mice were housed in groups of three to five on a standard 12 h light/12 h dark cycle, and all experiments were performed during the light cycle. Food and water were provided ad libitum.

Retina collection. Following cervical dislocation and decapitation, eyes were enucleated with curved forceps. Retinas were rapidly dissected in 1× phosphate-buffered saline (PBS) and transferred to 4% (w/v) paraformaldehyde (Sigma-Aldrich, P6148-1KG) for 30 min fixation. After 3× wash in 1× PBS, retinas were placed overnight at 4°C in 30% (w/v) sucrose (Sigma-Aldrich, 84097-1KG)/PBS. After three freeze-thaw cycles on dry ice, retinas were washed three times with 1× PBS, and blocked for 1 h at room temperature (RT) in blocking solution (1% [w/v] bovine serum albumin [Sigma A9418], 5% [v/v] Triton X-100 [Sigma T8787], 0.5% [w/v] sodium azide [VWR 786-299], and 10% [v/v] serum [either goat, Millipore S26, or donkey, Millipore S30]).

Retinal vibratome sections. Cryo-protected retinas were embedded into 3% (w/v) Agarose/PBS to obtain coronal sections. Retinas were sliced in 120 µm coronal sections on a vibratome (Leica VT 1200S).

Optic nerve crush (ONC) procedure (performed by Dr. Margaret Maes). Mice were anesthetized in an induction chamber with 5% (v/v) isoflurane (Zoetis) supplied with oxygen at a flow rate of 0.6 L/min. After lack of a foot pinch reflex, mice were maintained at 2.5% (v/v) isoflurane applied through a nose cone while on a heating pad to maintain body

temperature at 37ºC. Proparacaine hydrochloride 0.5% ophthalmic eye drops (Ursapharm Arzneimittel GmbH) were applied to numb the eyes, and subcutaneous injection of 5mg/kg Metacam alleviated pain (Meloxacam, Boehringer Ingelheim). The lateral canthus was de-vascularized by clamping with a hemostat (Fine Science Tools) for 10 seconds. Using a Leica dissection microscope, a lateral canthotomy allowed visualization of the posterior pole. While firmly holding the conjunctiva with a jeweler forceps, the conjunctiva was cut perpendicular to the posterior pole. The surrounding muscle was carefully dissected as to not puncture the vascular plexus. The optic nerve was pinched 1mm from the posterior pole for 4 seconds using a curved N7 self-closing forceps (Dumont). Triple antibiotic ointment was applied to the eye directly after the surgery to prevent infection.

Confocal microscopy. Images were acquired with a Zeiss LSM880 upright Airy scan or with a Zeiss LSM700 upright using a Plan-Apochromat 40× oil immersion objective N.A. 1.4. 2 × 2 z-stack tail-images were acquired with a resolution of 1024 × 1024 pixels.

Image processing. Confocal tile images were stitched using the software Imaris Stitcher 9.3.1.v. Then, the confocal images were loaded in Fiji 1.52e (http://imagej.net/Fiji). To remove the background, the rolling ball radius was set to 35 pixels, and images were filtered using a median 3D filter with x, y, z radii set at 3. Image stacks were exported as .tif files, converted to .ims files using the Imaris converter, and imported into Imaris 8.4.2.v. (Bitplane Imaris).

Quantification of CD68 volume within cells. Surface renderings were generated on microglia and CD68 z-stacks using the surface-rendering module of Imaris 9.2.v Surfaces were generated with the surface detail set to 0.2 μm. To determine the CD68 surface within microglia, the surface-surface coloc plugin was used. This analysis was performed on the entire image. The total ratio of CD68 volume within microglial volume (CD68-to-microglial volume) was calculated per image. To compute the CD68 fold change, the total CD68-to-microglial volume from each condition (sex/time-point) was scaled to the CD68-to-microglial volume ratio from the respective controls. CD68 fold change > 1 means an increase in CD68 volume, CD68 < 1 means a decrease in CD68 volume. CD68 fold-change = 1 denotes no change in CD68 volume.

Quantification of microglia density and statistical analysis. The spot-function plugin of Imaris 9.2.v was used to count the number of cells, i.e the soma of iba-1 positive microglia within every confocal image. Microglial cell density was estimated as total number of cells obtained in this way, divided by the size of the imaged sample in mm^2. After testing the normal

distribution of the data, sex averages for microglia from each region were compared with two-sided t.test or Kruskall-Wallis test for non parametric data.

Other methods such as *Immunofluorescence staining, reconstruction of 3D-traced microglia, topological morphology descriptor (TMD), average and bootstrapped persistence images, subtraction images and TMD distance, dimensionality reduction, UMAP and Palantir* were performed as indicated in the previous method sections (**see section 3**).

8 Results

8.1 MorphOMICs detects subregional microglial phenotypes

To investigate whether differences between OPL_{mg} and IPL_{mg} are reflected at a morphological level in physiological conditions, we acquired confocal images from the retina of adult $Cx3cr1^{GFP/-}$ mice for both sexes in at least biological triplicates. We traced OPL_{mg} and IPL_{mg} to generate a library of three-dimensional (3D) microglial skeletons, and applied MorphOMICs on the reconstructed trees. OPL_{mg} and IPL_{mg} segregated in two distinct clusters in the UMAP space suggesting morphological differences (**Fig. 46**). To gain insights on microglia morphology layer-specific differences, we subtracted the averaged bootstrapped persistence images from OPL_{mg} and IPL_{mg}. The subtraction plot shows that OPL_{mg} contain more primary processes that are more branched in the periphery. In contrast, IPL_{mg} display more short secondary branches.

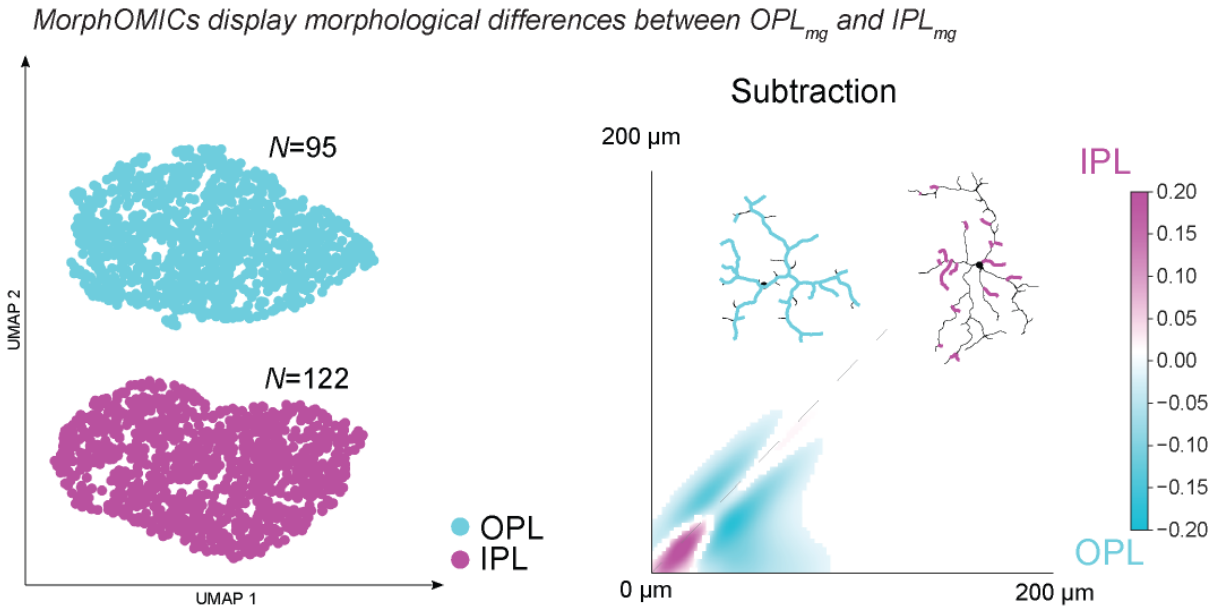

Fig. 46. Microglial morphology in the adult retina. OPL_{mg} (cyan) and IPL_{mg} (magenta). Left: UMAP plot of MorphOMICs-analyzed retinal microglia from adults $Cx3cr1^{+/GFP}$. Each dot represents a bootstrapped persistence image from at least six animals, both sexes combined. Right: Subtraction plot of average bootstrapped persistence image with color-coded overrepresented areas. Grey dashed line: TMD space diagonal. Inlay: Example traced microglia with highlighted distinct features.

Next, we asked whether retinal microglia exhibit a sexually dimorphic phenotype. First, we computed the analysis of region specificity as in (**Fig. 47**). For this, we varied the number of male and female microglia proportion in the bootstrapped population for each layer. In the UMAP space, bootstrapped populations that contain either only male or female microglia were at the extremities of each cluster. Sex-mixed bootstrapped population gradually organized

along the cluster dependent on the number of male or female microglia. Interestingly, in **Fig. 47**, OPL and IPL segregate similar to **Fig. 47** suggesting that the layer-specificity of microglial morphology influences their segregation to a higher degree than the sexual dimorphism.

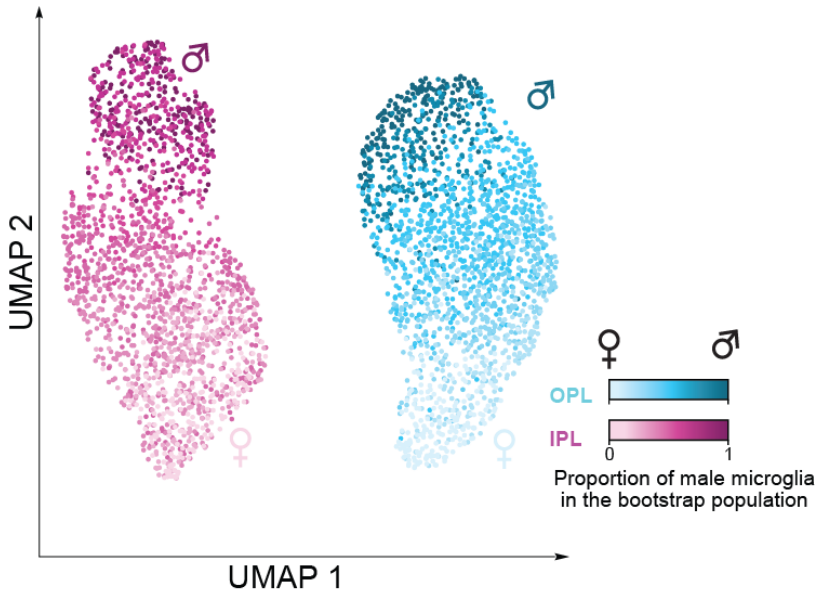

Fig. 47. Sexual dimorphism in adult retina. UMAP plot of OPL_{mg} (cyan) and IPL_{mg} (magenta). Gradient color-coded for the percentage of males in a population: 0, no males (lighter color). 1, pure males bootstraps (darker color). Each dot represents a bootstrap persistence image. Bootstrap size: 20.

Next, we asked whether morphological differences correlate to different microglial distribution in OPL and IPL. Thus, we quantified the density of microglia in each layer and compared it across sexes (**Fig. 48**). However, neither in the OPL nor in the IPL we observed significant difference in the microglia density, even though there was a trend for males having more microglia. Since microglia in females are known to express more phagocytic markers [90], we asked whether the morphological differences could underlie altered pro-phagocytic states. Therefore, we performed immunostaining for the endosomal-lysosomal marker CD68 and analyzed the CD68 volume with the microglial volume. When we compared males and females, we did not find a significant difference between sexes suggesting that the classical phagocytic marker CD68 cannot explain the intrinsic microglial morphological differences between OPL_{mg} and IPL_{mg} (**Fig. 48**).

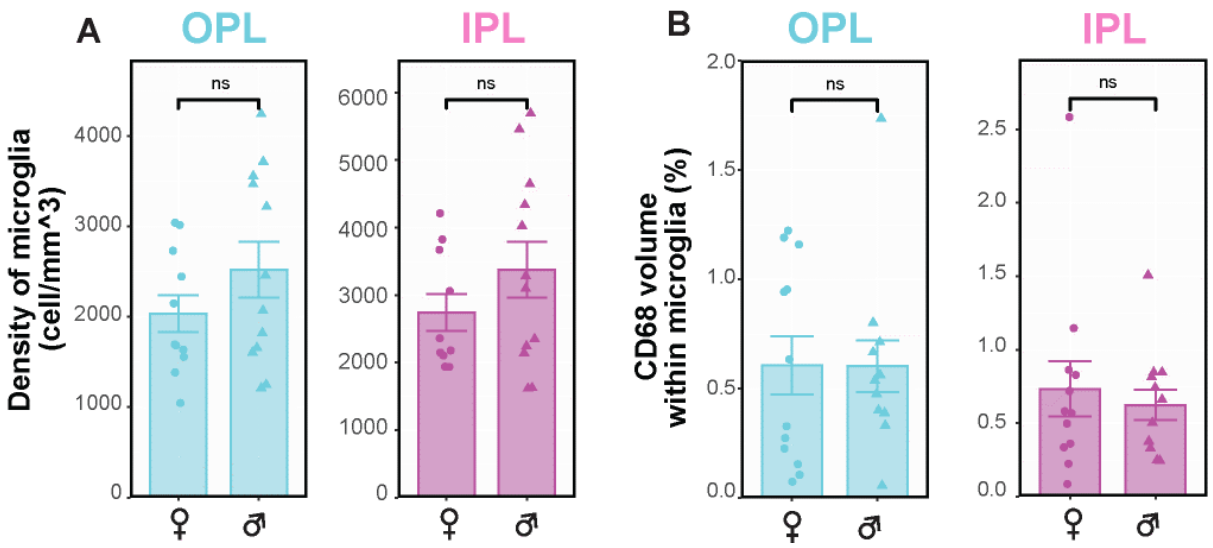

Fig. 48. Microglial density and CD68 across sexes in adult retina. Adult OPL_{mg} (cyan) and IPL_{mg} (magenta). Each data point: one animal. Circle: female. Triangle: male. **A:** Mean densities of $Iba1^{+}$-microglia per mm^3± SD. Kruskal-Wallis test for non-parametric data: OPL_{mg}: $p = 0.2679$, $df = 1$, $n_{♀} = 10$, $n_{♂} = 12$; IPL_{mg}, $p = 0.2914$. $n_{♀} = 10$, $n_{♂} = 12$. **B:** Percentages of CD68 volume within microglial volume. Kruskal-Wallis test for non-parametric data: OPL_{mg}: $p = 0.8625$, $df = 1$, $n_{♀} = 12$, $n_{♂} = 12$; IPL_{mg}: $p = 0.9539$, $n_{♀} = 12$, $n_{♂} = 12$. $p^{ns} > 0.05$, non-significant. SD: standard deviation.

In conclusion, MorphOMICs detects the sub-regional morphological differences in microglia of the healthy adult retinas and suggests that the microglial morphology depends on their local environment similar to the other brain regions.

8.2 Generating the morphological map of microglia in the retina

Microglia exhibit context-dependent morphologies that go beyond the classical dichotomy of surveilling or activated. By applying MorphOMICs to microglial morphologies in the brain, we reconstructed a morphological map across conditions. Next, we focused on deriving a similar spectrum of layer-specific microglial morphologies in the retina built a map based on postnatal development, adulthood, and the rd10 degeneration model.

1.7.1 Spatial morphological differences of microglia during retinal development

To generate a dataset of microglial morphologies during the postnatal retinal development, we acquired for each plexiform layer confocal images of $Cx3cr1^{GFP/-}$ retinas collected postnatally every day from P1 until P30. In this way, we were able to track with a daily resolution the time window where the retinal layers form and undergo remodeling (**Fig. 49**).

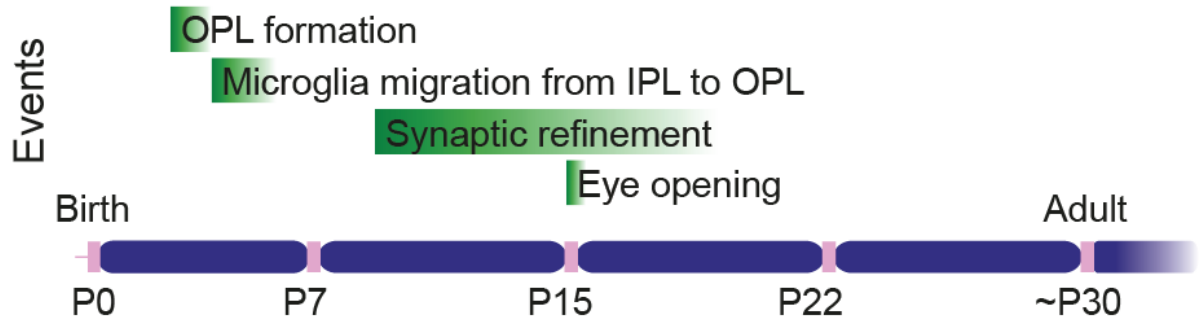

Fig. 49. Time-line of retinal postnatal development. P: postnatal time-point.

We generated 3D-skeletons for each layer. As a note: Since the OPL only occurs as a clearly defined layer starting from postnatal day 7 [227], we start to trace OPL_{mg} starting from P7. From microglial confocal images, we already detect that OPL_{mg} and IPL_{mg} increased their size and acquired ramification over the development, and especially IPL_{mg} displayed process retraction until ~P9 **(Fig. 50**).

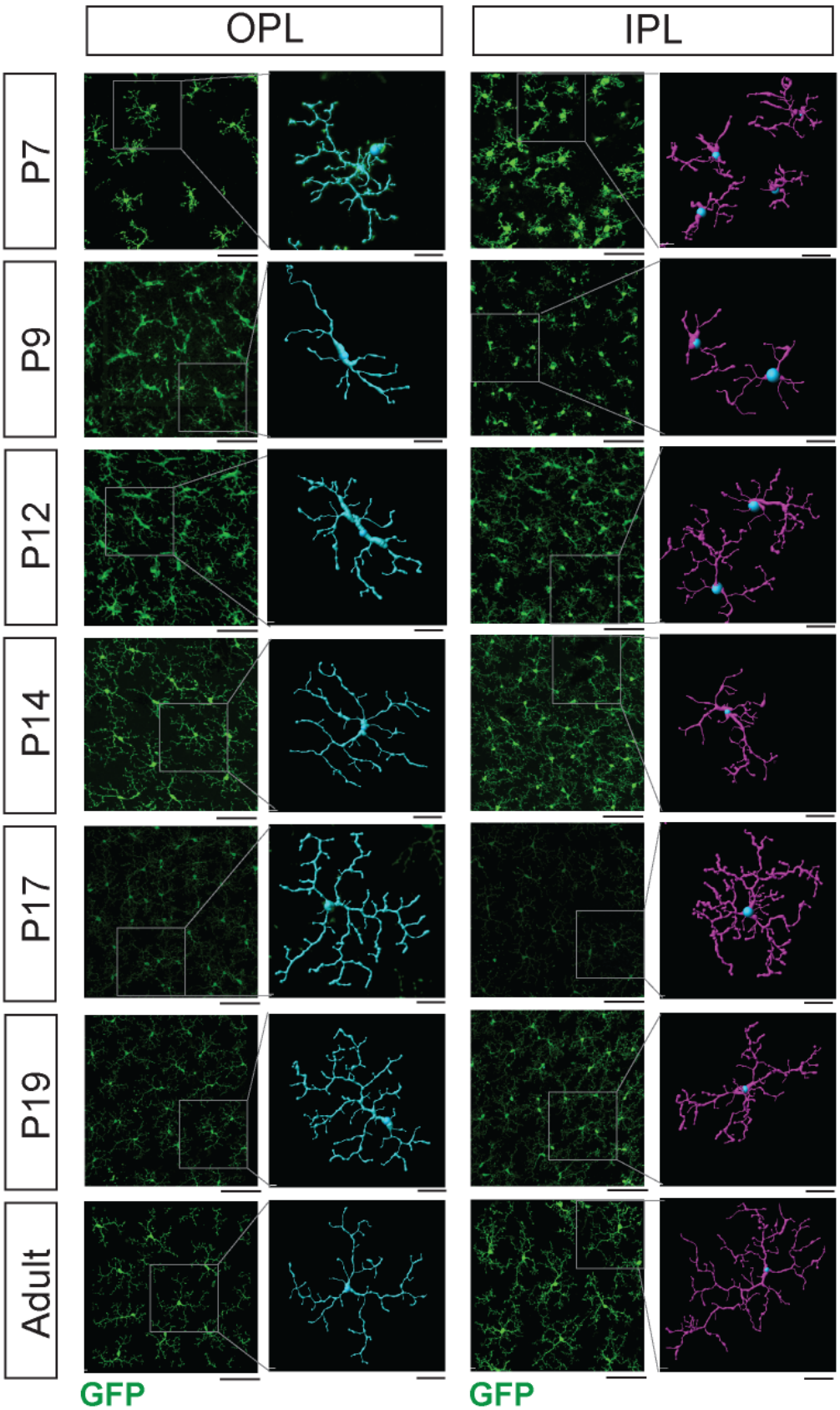

Fig. 50. Retinal microglia during postnatal development. Confocal images of the GFP-positive microglia population (green) in Cx3cr1$^{+/GFP}$ mice in the OPL (left) and IPL (right), Scale bar: 50 µm. Next, zoom-in of a representative tracing for OPL (cyan) or IPL (magenta). Blue dot: location of cell body. Scale bar: 20 µm.

Next, we asked whether the progressive increase in ramification correlated to modifications in microglial distribution and whether this was accompanied by a change in the level of microglial CD68. Therefore, we quantified microglia density and the percentage of microglial volume occupied by CD68 signal in each layer at P7, P15, and P22, representing early, intermediate and late development time-points, respectively (**Fig. 51** and **Fig. 52**). In the OPL, microglial density did not exhibit changes across development and did not upregulate CD68, although we observed a trend of decrease at P15. This indicates that microglia remain stable once microglia reach OPL (**Fig. 51**).

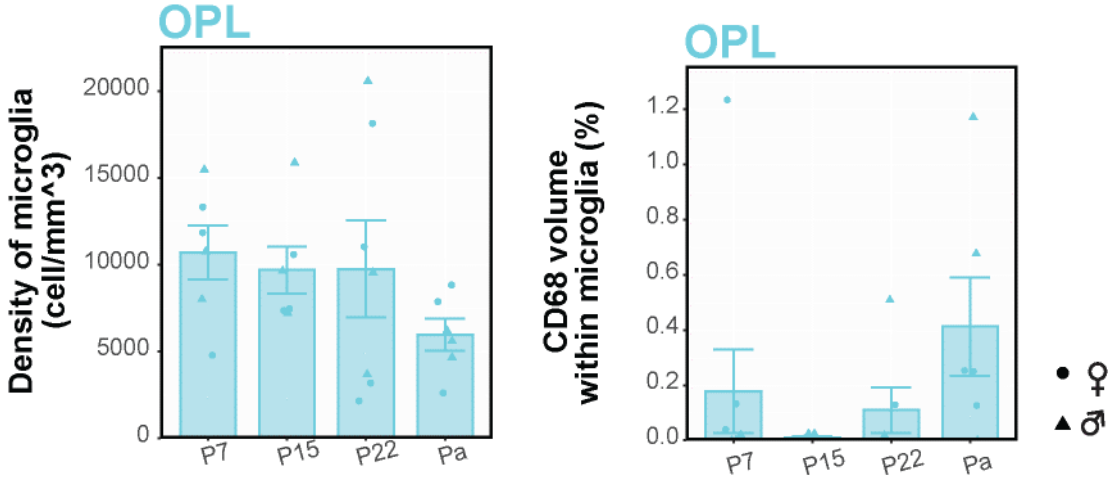

Fig. 51. OPL$_{mg}$ density and CD68 across sexes during postnatal development. Each data point: one animal. Circle: female. Triangle: male. Left: Mean densities of Iba1^{+}-microglia per mm^3 ±SD. Analysis of variance (one-way-ANOVA); OPL$_{mg}$: df = 3, Pr = 0.349. $n_{P7♂}$ = 6, $n_{P15♂}$ = 6, $n_{P22♂}$ = 7, $n_{Pa♂}$ = 6. Right: Percentages of CD68 volume within microglial volume ± SD. Analysis of variance (one-way-ANOVA); OPL$_{mg}$: df = 3, Pr = 0.222. n_{P7} = 8, n_{P15} = 6, n_{P22} = 6, $n_{Pa♂}$ = 3. SD: standard deviation.

Differently than in OPL, the IPL$_{mg}$ number decreased until adulthood. This is likely due to the massive migration towards the ONL layer happening in the first postnatal week [227]. However, also in IPL, CD68 was not significant reduced (**Fig. 52**).

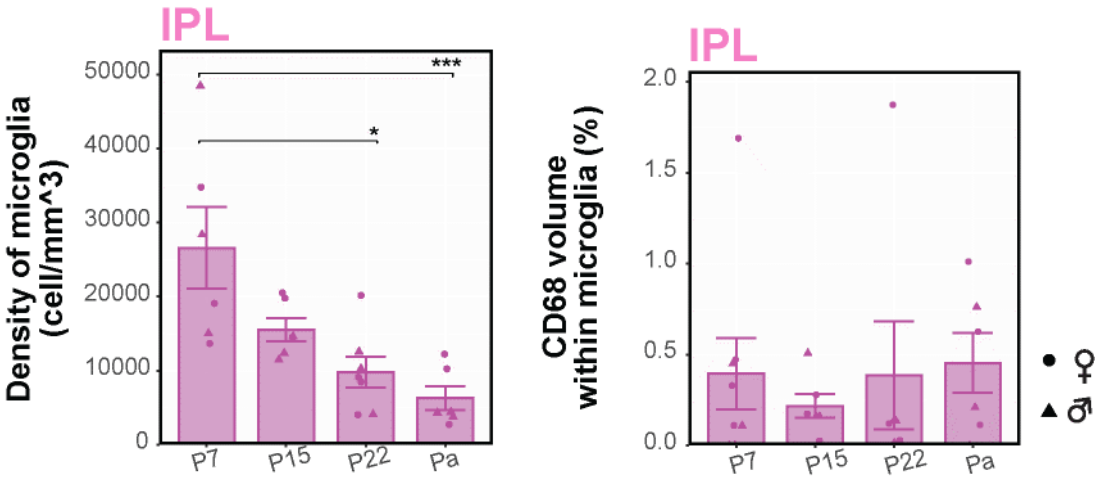

Fig. 52. Microglial density and CD68 across sexes during postnatal development. Adult OPL_{mg} (cyan) and IPL_{mg} (magenta). Each data point: one animal. Circle: female. Triangle: male. Left: Mean densities of $Iba1^{+}$-microglia per mm^3± SD. Analysis of variance (one-way-ANOVA): IPL_{mg}, df = 3, Pr < 0.001. Tukey post-hoc test (confidence interval 95%); $p_{(P22\text{-}P7)}$ = 0.004, $p_{(Pa\text{-}P7)}$ = 0.0009. $n_{P7♂}$ = 6, $n_{P15♂}$ = 6, $n_{P22♂}$= 7, $n_{Pa♂}$ = 6. Right: Percentages of CD68 volume within microglial volume ± SD. Analysis of variance (one-way-ANOVA); IPL_{mg}, df = 3, Pr = 0.869. n_{P7} = 8, n_{P15} = 6, n_{P22}= 6, $_{nPa♂}$ = 3. SD: standard deviation.

Interestingly, we did not observe a strong CD68 increase in OPL_{mg} nor IPL_{mg} in early developmental time-points, although they are characterized by massive microglial removal of apoptotic cells, which is typically linked to increased CD68 [66]. Since microglia are known to take part to circuital remodeling by pruning synapses and phagocytosing apoptotic neurons, we conclude that other pathways orchestrate such activity [227].

8.2.1 OPL-Microglia morphology responds to photoreceptor degeneration

To add microglia from a photoreceptor degeneration environment to the map, we included microglia images from the rd10 mouse model. We therefore sampled rd10 retinas from P10 until P65 every 5 days to cover the different degeneration phases [247] (**Fig. 53**).

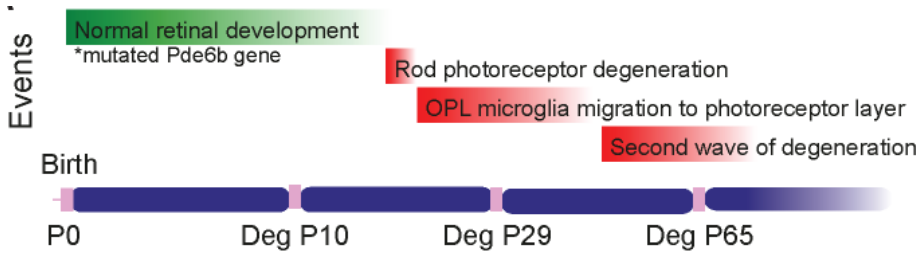

Fig. 53. Timeline of events during retinal degeneration in Rd10 mouse model. Deg.: degeneration time-point.

Then, we immunostained the retinas with the allograft inflammatory factor 1 (Aif1/Iba1) to identify microglia [104] and acquired confocal images of each layer (**Fig. 54**). OPL_{mg} exhibited a thicker morphology with process retraction starting from P15, which is before the start of photoreceptor loss. In the IPL_{mg}, morphological change are less obvious. The early response of OPL_{mg} might be explained since photoreceptor in rd10 model constitutively express the deleterious mutation causing their degeneration. Although they start to show sign of death at around one month of age, photoreceptor activity is likely affected earlier, which might explain microglia early morphological modification in the OPL. Interestingly, microglial morphology

seemed to recover at later stages. Next, we asked whether the degeneration correlated with layer-specific changes in microglial density or phagocytic activity.

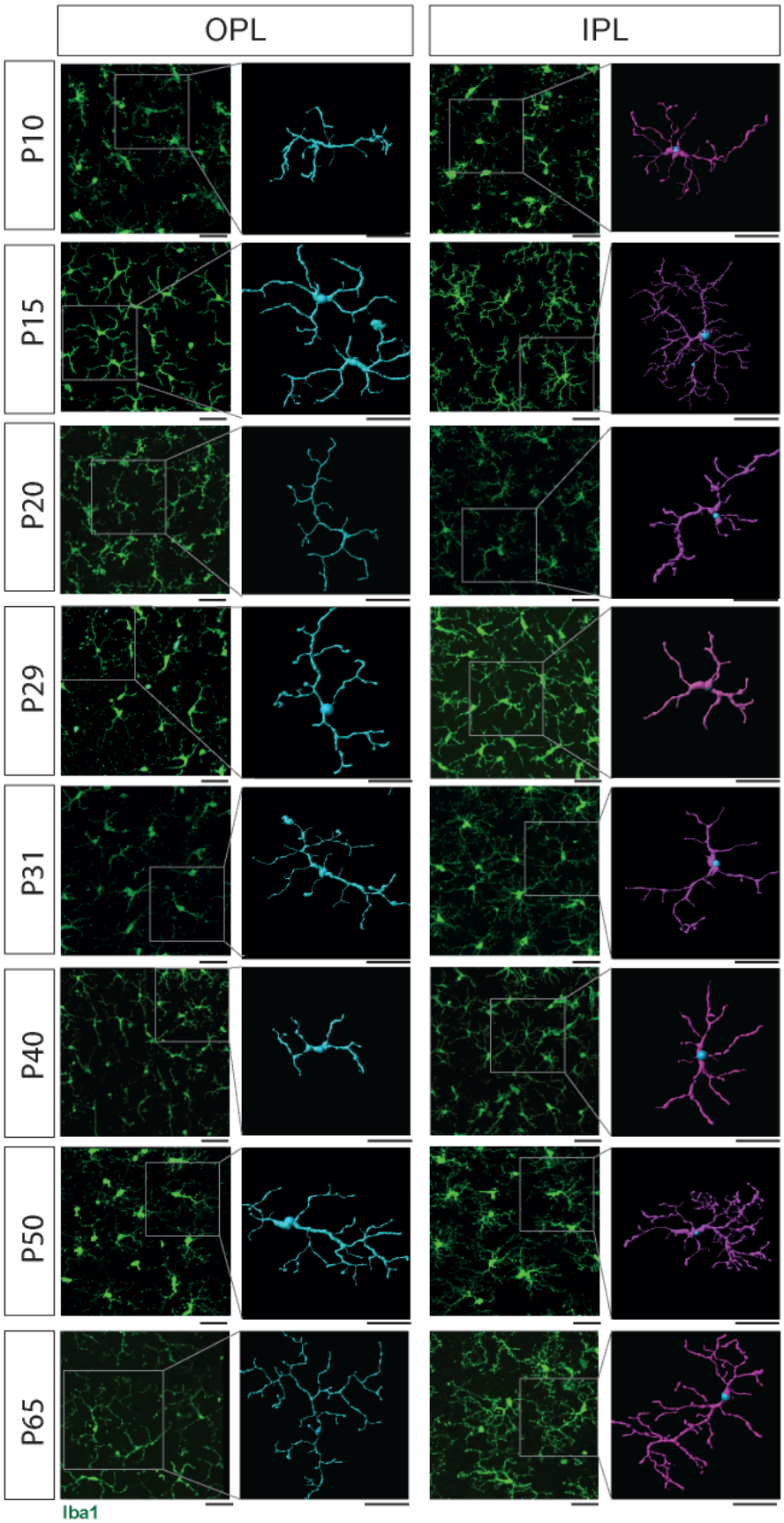

Fig. 54. Retinal microglia during rd10 degeneration. Confocal images of microglia population immunostained with Iba-1 (green) in rd10 mice in the OPL (left) and IPL (right), Scale bar: 50 µm. Next, zoom-in of a representative tracing for OPL (cyan) or IPL (magenta). Blue dot: location of cell body. Scale bar: 20 µm.

To address this question, we analyzed microglial distribution and CD68 content in OPL and IPL of rd10 retinas at P10, P29, P65 and compared the values to adults (**Fig. 55**). In the OPL, we observed significantly increased microglial density in proximity of photoreceptor degeneration peak. This density decreased again at P65. Similarly, OPL_{mg} CD68 content significantly increased at P29 and then recovered to a level comparable to adults from P65.

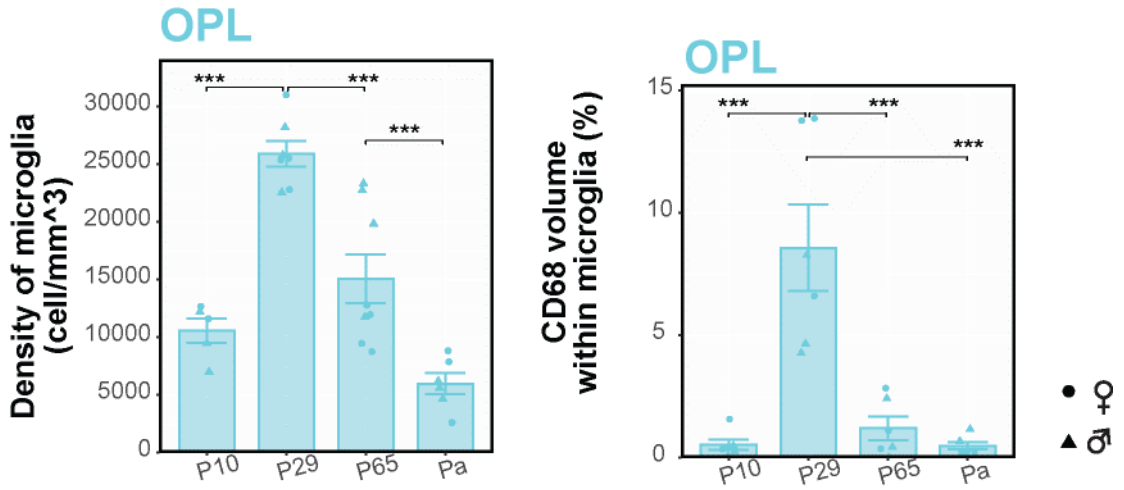

Fig. 55. Microglial density and CD68 across sexes in rd10 degeneration. Each data point: one animal. Circle: female. Triangle: male. Right: Mean densities of $Iba1^+$-microglia per mm^3± SD. Analysis of variance (one-way-ANOVA); OPL_{mg}: df = 3, Pr < 0.001; Tukey post hoc test (confidence interval 95%) $p_{(P29\text{-}P10)} < 0.001$, $p_{(P65\text{-}P29)} < 0.001$, $p_{(Pa\text{-}P65)} < 0.001$. $n_{P10} = 6$, $n_{P29} = 7$, $n_{P65} = 8$, $n_{Pa} = 6$. Right: Percentages of CD68 volume within microglial volume. Analysis of variance (one-way-ANOVA): OPL_{mg}: df = 3, Pr < 0.001. Tukey post-hoc test (confidence interval 95%), $p_{(P29\text{-}P10)} < 0.001$, $p_{(P65\text{-}P29)} < 0.001$, $p_{(Pa\text{-}P29)} < 0.007$. $n_{P10} = 6$, $n_{P29} = 6$, $n_{P65} = 6$, $n_{Pa} = 6$. SD: standard deviation.

In contrast, IPL_{mg} number exhibited a progressive decrease until P65 with a delay compared to the normal development (**Fig. 56**). This delay might be influenced by the acute degeneration phase because the density at P29 is still significantly higher than in adults. Microglial CD68 content in IPL_{mg} significantly increased until P29 and then decreased to baseline levels, although the percentage of microglial CD68 content in IPL barely exceeded the 1%, which was approximately ten-fold lower than in OPL_{mg} at P29. This suggests that photoreceptor abnormalities are sensed also from IPL_{mg}. Overall, OPL_{mg} change their density and CD68 expression to a higher extent than IPL_{mg} hinting a fine spatial regulation of their response.

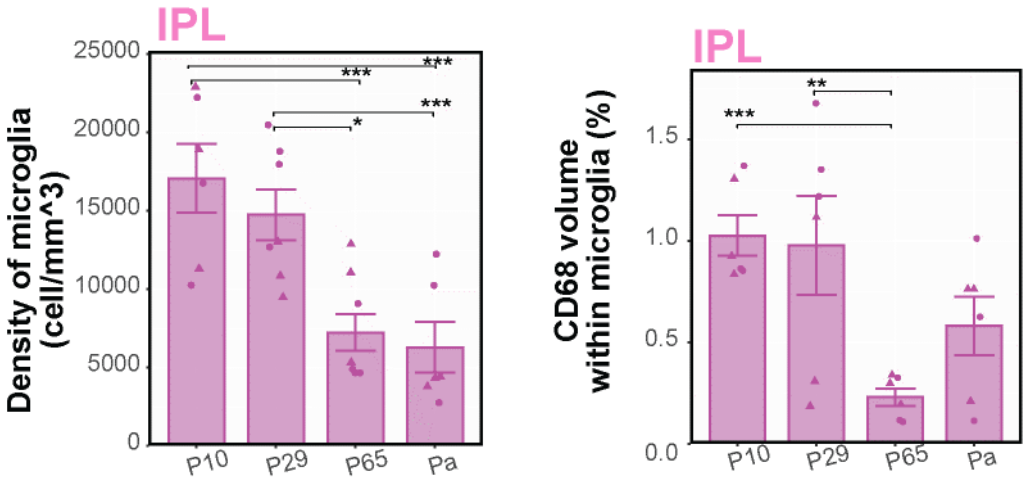

Fig. 56. Microglial density and CD68 across sexes in rd10 degeneration. Each data point: one animal. Circle: female. Triangle: male. Left: Mean densities of Iba1^{+}-microglia per mm^{3}± SD. Analysis of variance (one-way-ANOVA); IPL_{mg}, df = 3, Pr < 0.001. Tukey post hoc test (confidence interval 95%) p(P65-P10) = 0.001, $p_{(Pa-P10)}$ = 0.001, $p_{(P6a-P29)}$ = 0.007, $p_{(Pa-P65)}$ = 0.002; n_{P10} = 6, n_{P29} = 7, n_{P65} = 8, n_{Pa} = 6. SD: standard deviation. Right: Percentages of CD68 volume within microglial volume. Analysis of variance (one-way-ANOVA): IPL_{mg}, df = 3, Pr < 0.001. Tukey post hoc test (confidence interval 95%) $p_{(P65-P10)}$ = 0.006, $p_{(P65-P29)}$ = 0.01. n_{P10} = 6, n_{P29} = 6, n_{P65} = 6, n_{Pa} = 6. SD: standard deviation.

8.2.2 Microglial spectrum in healthy and diseased retina

To reconstruct the morphological spectrum of microglia in the retina, we applied MorphOMICs to OPL_{mg} and IPL_{mg} reconstructed skeletons from the postnatal development and rd10 degeneration and visualized their combined trajectory with Palantir (**Fig. 57** and **58**). We derived layer-specific trajectories reflecting combined male and female microglia.

During OPL development, microglial morphology gradually transitioned from early development to mature morphology, which they reached at approximately P30 (**Fig. 58**). Interestingly, the morphology during rd10 degeneration follows a similar trajectory but moves in the opposite direction. OPL_{mg} at P29 shift to an early development-like phenotype, which resembles phenotypes during the early developmental waves. After the degeneration peak, they re-enter the trajectory of morphological maturation and partially recover but without reaching a full control phenotype at P65.

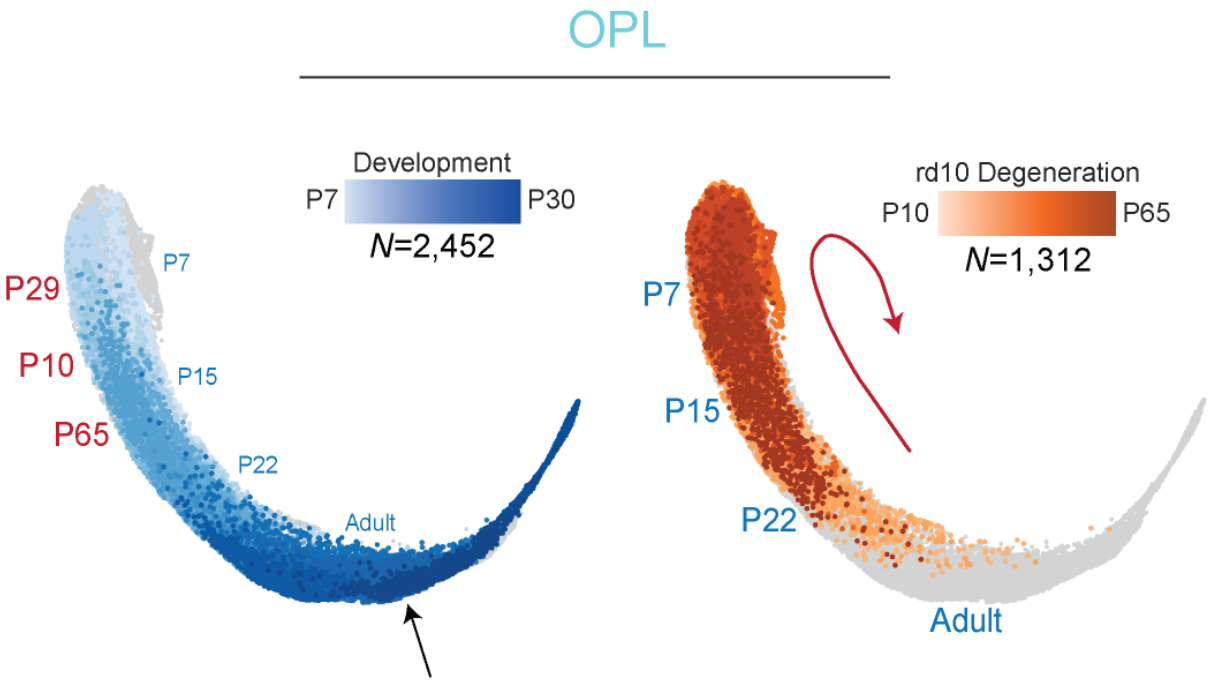

Fig. 57. OPL$_{mg}$ trajectory. Palantir reconstructions showing the reference atlas of microglial phenotypes calculated for OPL across Rd10 degeneration. Each dot is a bootstrap population. Grey points indicate the non-highlighted condition. Black arrow indicates overlap between developmental time-points and adult. Blue numbers indicate development trajectory. Red arrows and numbers indicate degeneration trajectory. Bootstrap size: 10.

During the postnatal development, IPL$_{mg}$ showed a linear trajectory similar to OPL. Interestingly, at P15, IPL$_{mg}$ already reached the adult phenotype, a sign that IPL$_{mg}$ reached maturity earlier than OPL$_{mg}$ (**Fig. 58**). Such linear progression of morphological modifications in IPL$_{mg}$ was maintained during rd10 degeneration indicating that microglia in rd10 disease progression affect mostly the outer retinal layers.

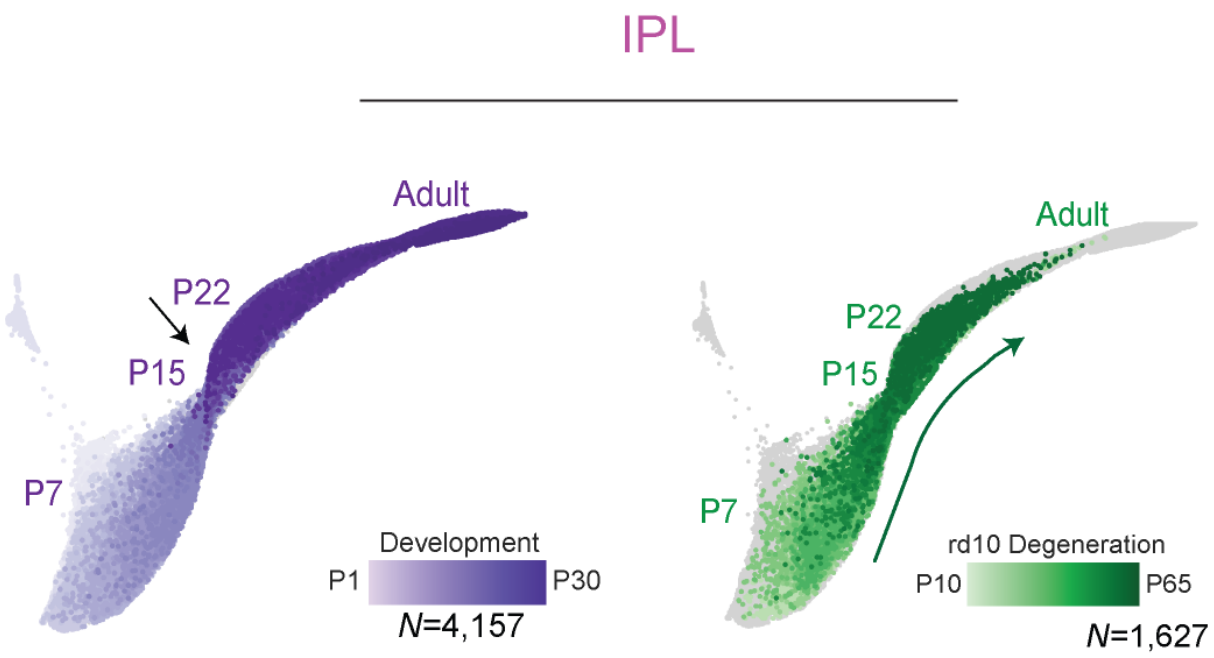

Fig. 58. IPL$_{mg}$ trajectory. Palantir reconstructions showing the reference atlas of microglial phenotypes calculated for IPL across Rd10 degeneration. Each dot is a bootstrap population. Grey points indicate the non-highlighted condition. Black arrow indicates overlap between developmental time-points and adult. Purple numbers indicate development trajectory. Green arrows and numbers indicate degeneration trajectory. Bootstrap size: 10.

8.3 The retinal map of microglial morphology

The spectrum of microglial morphologies that we showed in **Fig. 57** and **Fig. 58** provides an atlas on which we can map microglial morphology from different conditions. Employing a machine-learning algorithm, we trained a linear regression model to infer the coordinates of single cell morphology on the morphological spectrum similar to what we have showed for the brain in **Fig. 40**. Additionally, we can use the model to estimate the centroid position of a new condition on the previously built Palantir trajectory (**Fig. 59**).

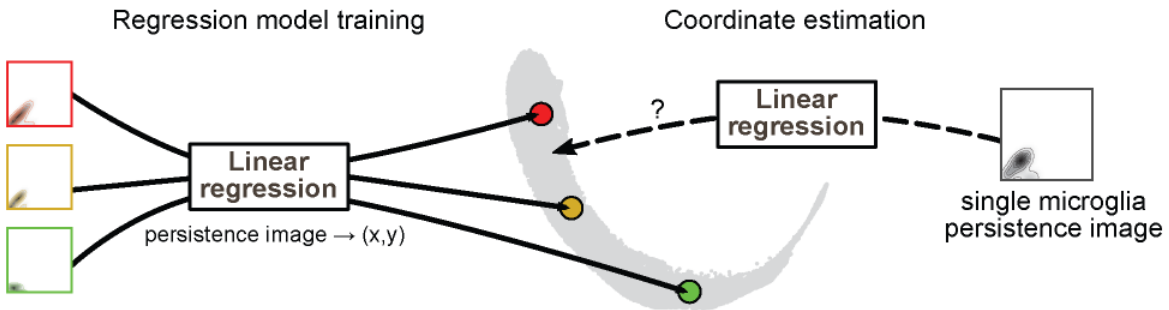

Fig. 59. ***Schematic of MorphOMICs pipeline covering spectrum mapping***. Linear regression was used to map the bootstrapped persistence image to its position in the reference atlas. The same linear regression model is used to map single persistence images into the reference atlas by estimating the location of the Palantir coordinates.

8.3.1 MorphOMICs reveal mild sexual dimorphism during retinal development

First, we used our morphological map to investigate how pronounced sex affects the postnatal developmental trajectories. For this, we trained a linear model to display the position of microglia from female and male Cx3cr1$^{+/GFP}$ mice separately on the previously built Palantir trajectory (**Fig. 57** and **Fig. 58**). We focused on early (P7), intermediate (P15) and late (P22) developmental stage to cover the first two postnatal weeks dominated by apoptosis and phagocytosis, and the later developmental stage, where circuit adaptations and wiring refinement are predominant [227]. OPL$_{mg}$ displayed a sexual dimorphic trajectory with ♀OPL$_{mg}$ rapidly shifting towards the adult phenotype already at P15, while ♂OPL$_{mg}$ show a more gradual maturation (**Fig. 60**). In contrast, the sex did not show any obvious effect on IPL$_{mg}$.

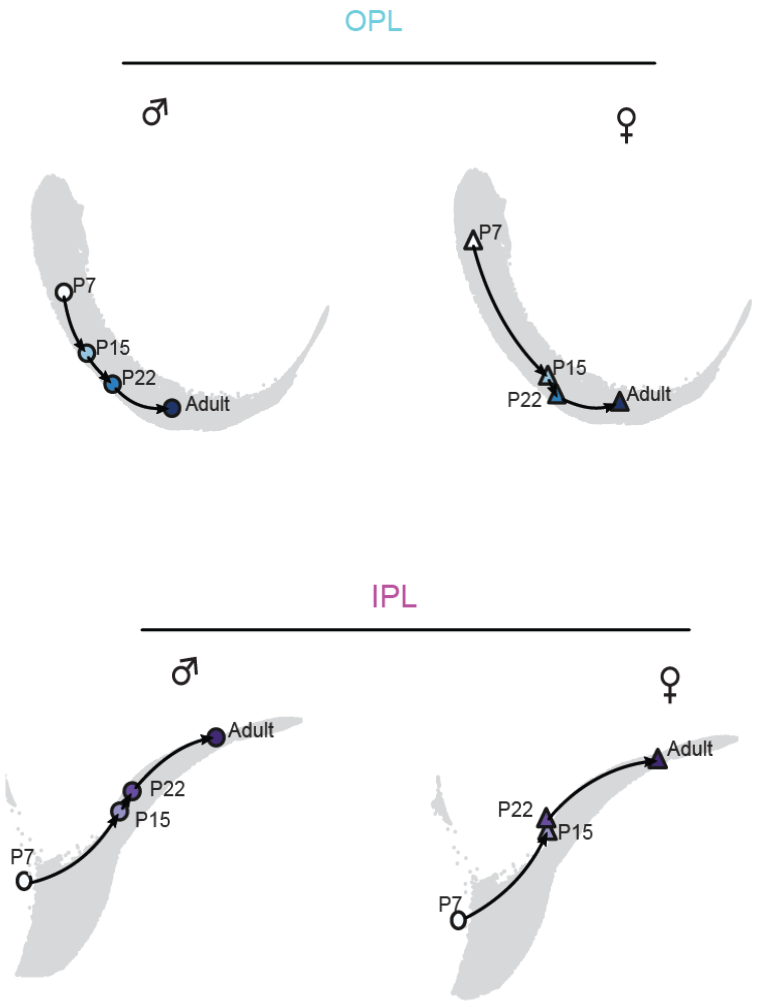

Fig. 60. ***Microglial sexual dimorphism during postnatal development.*** Retinal reference atlas for OPL (left) and IPL (right) with mapped position from postnatal (P) developmental time points at P7, P15, P22 separated by retinal layer and sex

8.3.2 Microglia are mildly sex-specificity in response to rd10 degeneration

We have recently shown that microglia exhibit a sex-specific response in the brain (**see section 2**). Whether a similar phenotype exists in the retina is less explored. Li and colleagues showed that female rd10 mice are more susceptible than males to photoreceptor loss but did not describe whether this correlates with sex-specific microglial differences [262]. To investigate whether microglial morphological trajectory displays sex-specificity in response to rd10 degeneration, we sampled microglia from females and males separately at an early (P10), a middle (P29), and a late degeneration time point (P65). Then, we mapped their position on our Palantir reference trajectory. We started looking at OPL_{mg}, as from our previous trajectory rd10 degeneration largely influences their morphology (**Fig. 61**). Here, both ♀OPL_{mg} and ♂OPL_{mg} microglia assumed an early development-like morphology around P29. At P65, both sexes did not fully recover to the adult controls: At P65, ♂OPL_{mg} resembled the morphology of the first two postnatal weeks, in which microglia are phagocytosing apoptotic cells. Instead, in ♀OPL_{mg}, P65 microglia positioned between P15 and P22, when the postnatal development is characterized by less apoptosis and more wiring adaptation. As expected from **Fig. 58**, IPL_{mg} follow a linear path in both sexes during Rd10. Nevertheless, the maturation of microglial morphology was delayed, and in both sexes did not reach complete maturation. This indicated that microglia respond to photo degeneration even in IPL to small degree, and display a morphology that suggests a persisting refinement state.

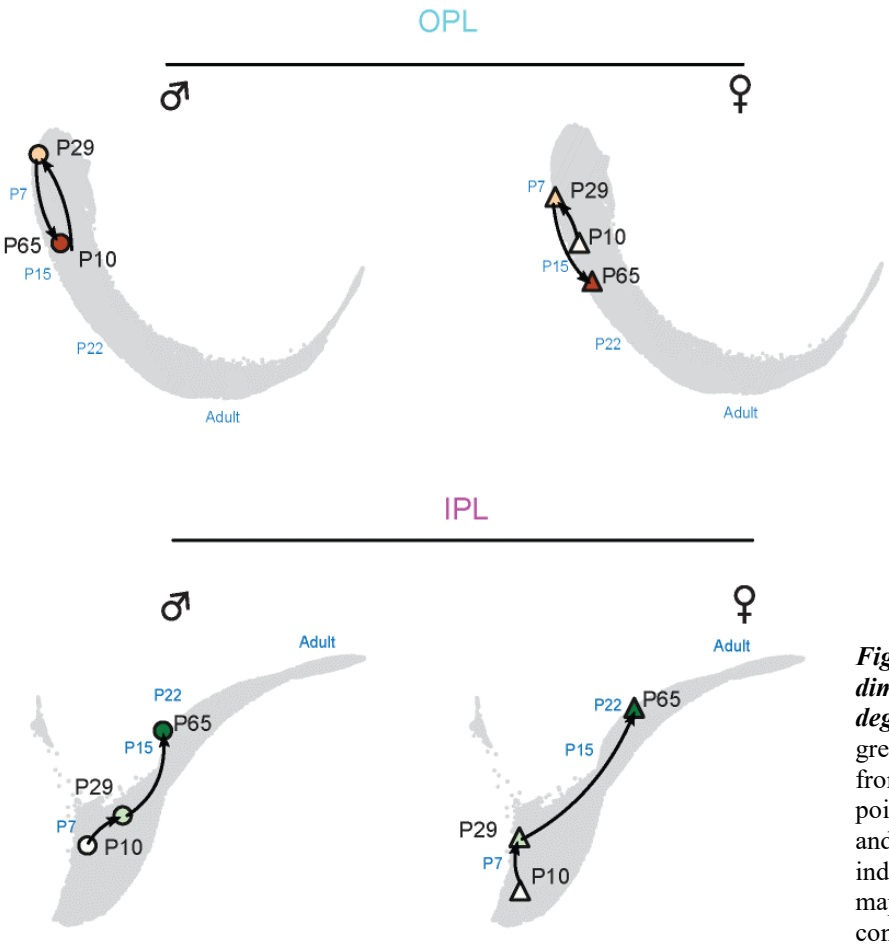

Fig. 61. Microglial sexual dimorphism during rd10 degeneration. Reference atlas in grey with mapped single cells from different degeneration time points, separated by retinal layer and sex. Each dot is a centroid indicating the median position of mapped single cells in a given condition. Black arrows linking dots indicate time progression

8.3.3 MorphOMICs detects microglial sexual dimorphism following ONC

Finally, we were interested to investigate microglial morphological response to a mechanically induced degeneration of retinal ganglion cells via the optic nerve crush (ONC). We therefore performed ONC on adult C57BL/6J mice from both sexes and sampled the retinas 5, 14 and 35 days after the surgical procedures as well as from sham control mice (**Fig. 62**). We chose these time-points because ONC microglia build a strong inflammatory response, which peaks around 5 days after the surgical procedure, and then gradually decreases from 14 days [263]. By collecting samples from 35 days post ONC, we included a middle-term control of microglial morphology recovery.

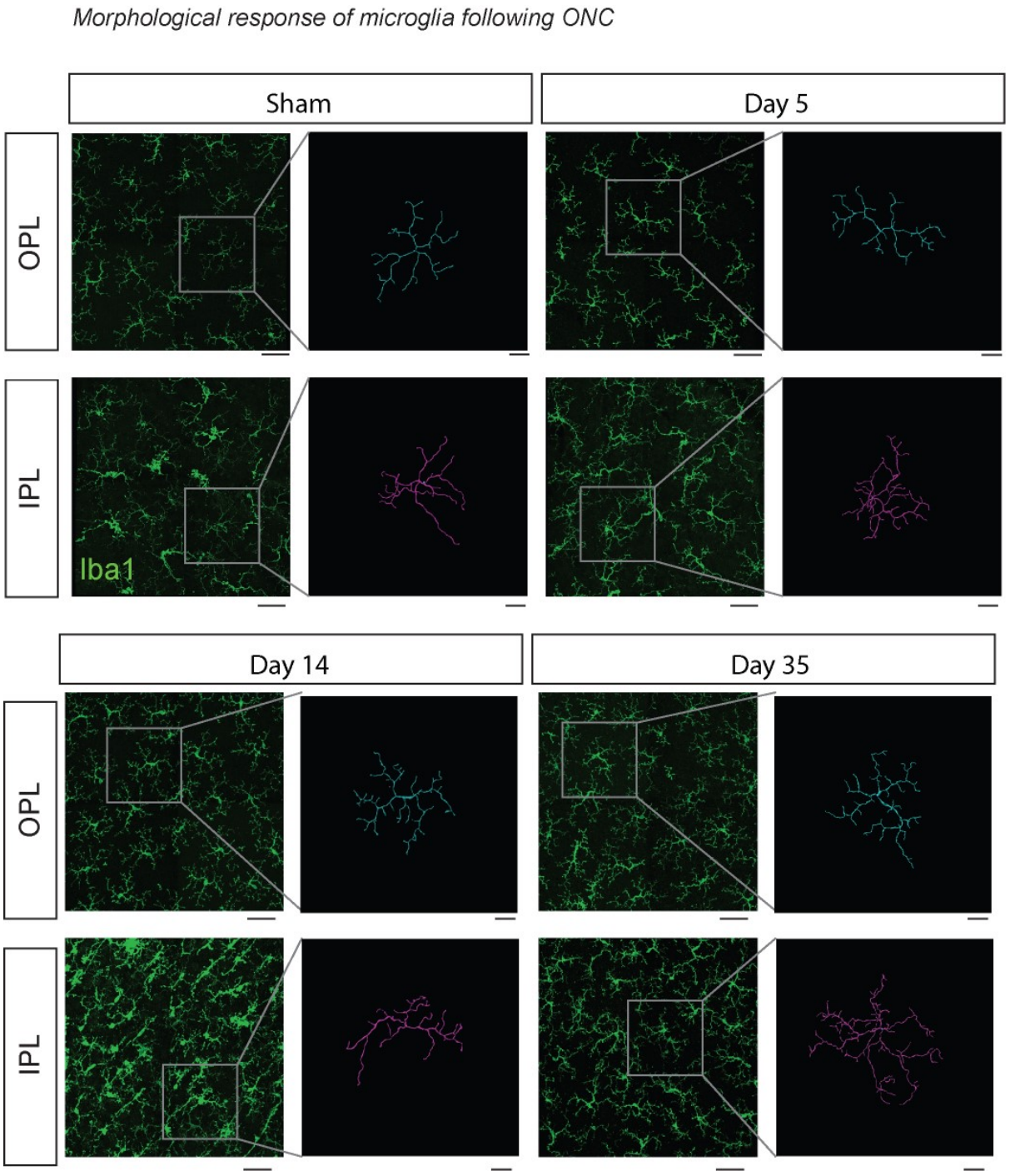

Fig. 62. Microglial morphology following ONC. Confocal images showing microglia (Iba-1,green) from OPL and IPL in C57BL/6J mice 5, 14 and 35 days after ONC compared to control, with zoom-in showing one cell reconstruction. Scale bar: 30 and 20 µm

From the confocal images, OPL_{mg} did not show obvious adaptation during the entire time-course, while IPL_{mg} displayed retracted morphology 5-days after ONC. Limited information is available on sex impact on optic neuropathies. A recent study hints that estrogen seem to exert a protective effect [264]. Since microglial reactivity is known to be influenced by estrogens [215],

we wondered whether microglial morphology respond in a sex-specific manner and therefore divided our data based on sex. To follow microglial morphology in response to ONC, we mapped OPL_{mg} and IPL_{mg} morphology to their corresponding retinal projection map (**Fig. 63**).

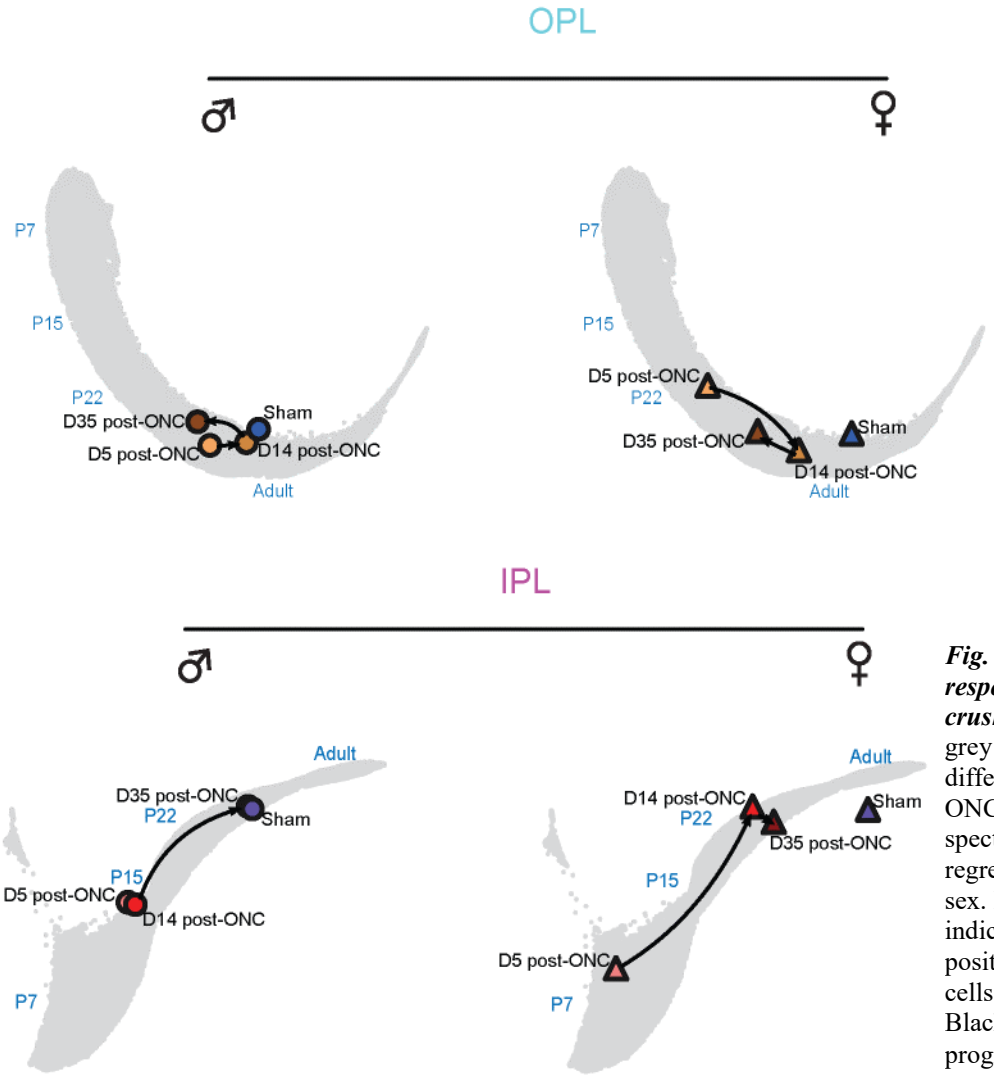

Fig. 63. Microglia response to optic nerve crush Reference atlas in grey with single cells from different time points post-ONC mapped into the spectrum using linear regression, separated by sex. Each dot is a centroid indicating the median position of mapped single cells in a given condition. Black arrows indicate time progression

Based their disposition on the morphology map, OPL_{mg} display a limited morphological response to ONC. Interestingly, 5 days after ONC microglial phenotype in ♀OPL_{mg} shifts more than ♂OPL_{mg} to developmental, which might underlie higher responsivity in females (**Fig. 63**). In IPL_{mg}, both sexes massively respond 5 days after ONC shifting to an immature morphology that resembles a highly phagocytic phenotype of the first two postnatal weeks. However, the morphological response of IPL_{mg} is highly influenced by sex. ♂OPL_{mg} shifted to an earlier development-like morphology and maintained this morphology until 14 days post ONC. From 35 days post ONC, the morphology shifted towards the sham control. In contrast, ♀IPL_{mg} morphology reverted 14 days after the lesion although never completely recovered to the sham phenotype. In summary, our data show that microglial morphology responds more in IPL than

in OPL, as it is closer to retinal ganglion cell and the primarily affected layer after ONC. Moreover, we observed a sex-specific response with ♀IPL_{mg} showing a faster recovery and a more profound morphological shift 5 days after ONC compared to ♂IPL_{mg}.

9 Conclusion

In this study, we generated a dataset of over 11,000 retinal microglia from OPL and IPL. With MorphOMICs, we generated a layer-specific morphological spectrum of microglia sampled from adulthood, postnatal development and during the time course of a genetic model of retinal degeneration. First, MorphOMICs detected layer-specific and sexual-dimorphic microglial phenotype in the adult retina, which is not supported by differences in density nor in CD68 content and was never observed before. As a note, the layer-specific morphology might be partially dependent on spatial constrains, as the OPL is thinner than the IPL. This effect requires further investigations such as morphological modelling to test how microglia optimize their wiring in their niche.

Next, we derived the Palantir trajectory of microglial morphology over postnatal development. We observed that in both OPL_{mg} and IPL_{mg} the morphology gradually shifts from early-development to adult (**Fig. 57** and **Fig. 58**). During this time-windows, the density of OPL_{mg} is stable, while IPL_{mg} significantly decreased reflecting microglia migration to the OPL (**Fig. 51**). In parallel, the CD68 content in both layers is stable. During Rd10 degeneration, the temporal order is disrupted in OPL_{mg}, and microglia acquire an early development-like morphology (**Fig. 54** and **Fig. 57**). This might be explained by microglia during development and reactive microglia in a degenerating environment share features like process retraction and pro-phagocytic state. At the same time, around degeneration peak OPL_{mg} increase in number and in CD68 content and then recover to control level (**Fig. 55**). In contrast, IPL_{mg} develop normally, although some fluctuations in cell density and CD68 suggest that even in IPL, microglia respond to photoreceptor degeneration (**Fig. 56**).

Next, we used a linear-model based machine learning algorithm to map the position of microglia from development and rd10 degeneration on the morphological spectrum. By mapping females and males separately, we gained information on sexual dimorphism. According to our mapping, ♀OPL_{mg} during the development mature faster than ♂OPL_{mg} (**Fig. 60**), while no dimorphic effect is observed in IPL_{mg}. During rd10 degeneration, only OPL_{mg}

show obvious sex dimorphism. After P29, OPL_{mg} shift to an early development-like morphology, which is linked to increased apoptosis and phagocytosis (**Fig. 61**). Instead, ♀OPL_{mg} move towards P22, which characterizes a time-point with less reactivity and more wiring adaptations.

Finally, we used the spectrum as a map to localize the disposition of microglial morphology following ONC (**Fig. 62**). Since microglial response is regulated in space, OPL_{mg} did not show a strong response, while IPL_{mg} show high degree of sexual dimorphism (**Fig. 63**). ♂IPL_{mg} morphology recover 35 days post ONC, while ♀OPL_{mg} move back to sham already after 14 days. Interestingly, neither ♀OPL_{mg} or ♀IPL_{mg} morphology recover completely, which might suggest a female-specific long-term response to optic nerve lesion.

Overall, we see a much greater effect of sex following ONC than in rd10 model of degeneration. This might be explained by the fact that the nerve lesion in ONC causes a sever inflammation cascade, which is a known sexually dimorphic feature in microglia [96]. In contrast, rd10 displays a genetic model of degeneration, where neuronal apoptosis flanks severe alteration in neuronal activity rather than classical inflammation response.

In conclusion, MorphOMICs successfully captures layer- and sex-dependent microglial morphologies in the retina and provides a mapping tool for the detection of fine differences in their trajectory over development and disease.

10 Concluding remarks and perspectives

With MorphOMICs, we built a comprehensive morphology atlas collecting more than 50.000 microglial morphologies from eight brain regions and in response to diverse environmental cues. In the brain, MorphOMICs uncovered region-specific and sexually dimorphic morphological trajectories. In the retina, it allowed us to look with a higher resolution at sub-regional differences in microglia that are exposed to layer-specific microenvironment modifications. With our method, we overcome the dichotomized view of microglial morphology to either ramified, relating to a surveilling function, or amoeboid, for highly phagocytosing.

We anticipate that future studies will build on MorphOMICs and our atlas and will incorporate the epigenetic-, transcriptional- and/or proteomic landscapes along the microglial phenotypic spectrum. We are also working to implement advanced morphological modelling to test wiring optimization in microglia from different layers. Integrating different layers of microglial heterogeneity analysis will help us to characterize their wide spectrum of response and will significantly advance our knowledge of the interplay between microglia and the nervous system.

11 Extended Data Tables

Extended Data Table 1

	Condition	Time point	Total (excl.)	♂	♀	♀ov
Cerebellum (CB)	Adult	8-12 weeks	607 (2)	246	299	60
	Development	P7	399 (0)	189	210	
		P15	685 (0)	175	510	
		P22	656 (4)	440	212	
	5xFAD	3 months	111 (2)	62	47	
		6 months	139 (1)	72	66	
	CK-p25	1 week	122 (0)	71	51	
		2 weeks	66 (1)	33	32	
		6 weeks	213 (1)	97	115	
Frontal cortex (FC)	Adult	8-12 weeks	2014(1)	894	926	193
	Development	P7	378 (1)	184	193	
		P15	953 (0)	584	369	
		P22	877 (0)	407	470	
	5xFAD	3 months	355 (0)	250	105	
		6 months	443 (0)	180	263	
	CK-p25	1 week	413 (0)	194	219	
		2 weeks	756 (0)	492	264	
		6 weeks	1321(1)	462	858	
Olfactory bulb (OB)	Adult	8-12 weeks	1671(1)	701	796	173
	Development	P7	274 (3)	196	75	
		P15	477 (0)	309	168	
		P22	698 (0)	390	308	
	5xFAD	3 months	285 (0)	82	203	
		6 months	776 (0)	244	527	
	CK-p25	1 week	285 (0)	144	140	
		2 weeks	657 (0)	223	432	
		6 weeks	640 (0)	235	405	
Substantia nigra (SN)	Adult	8-12 weeks	2264(2)	976	1050	236
	Development	P7	549 (2)	350	197	
		P15	943 (0)	405	538	
		P22	644 (0)	312	332	
	5xFAD	3 months	319 (0)	166	153	
		6 months	460 (0)	202	258	
	CK-p25	1 week	265 (1)	116	148	
		2 weeks	450 (1)	249	200	
		6 weeks	717 (1)	469	247	

	Condition	Time point	Total	♂	♀	♀ov
Cochlear nucleus (CN)	Adult	8-12 weeks	831 (0)	256	498	77
	Development	P7	478 (1)	252	225	
		P15	747 (0)	413	334	
		P22	659 (21)	311	327	
	5xFAD	3 months	236 (0)	117	119	
		6 months	170 (0)	67	103	
	CK-p25	1 week	208 (0)	129	79	
		2 weeks	249 (1)	133	115	
		6 weeks	209 (0)	72	137	
Dentate gyrus (DG)	Adult	8-12 weeks	1929(1)	913	902	116
	Development	P7	368 (1)	154	214	
		P15	439 (0)	289	150	
		P22	665 (0)	286	379	
	5xFAD	3 months	643 (0)	216	427	
		6 months	533 (0)	303	230	
	CK-p25	1 week	383 (0)	223	160	
		2 weeks	593 (0)	307	286	
		6 weeks	1630 (1)	293	1336	
Somatosensory cortex (S1)	Adult	8-12 weeks	1710(3)	821	719	167
	Development	P7	312 (0)	165	147	
		P15	688 (0)	458	230	
		P22	786 (0)	506	280	
	5xFAD	3 months	540 (0)	254	286	
		6 months	629 (1)	374	254	
	CK-p25	1 week	443 (2)	177	264	
		2 weeks	479 (0)	273	206	
		6 weeks	835 (1)	231	603	
	KXA	1x KXA	377 (4)	213	160	
		2x KXA	295 (0)	159	136	
		3x KXA	292 (2)	136	154	
	Recovery after 3x KXA	3 days	223 (0)	115	108	
		1-week	258 (2)	123	133	
		2-weeks	297 (0)	171	126	

Extended Data Table 1. Number of traced microglia for each brain region, sex, and condition. Total, total number of traced cells. In brackets, number of excluded cells that did not pass the quality check and were discarded from further analysis. ♀ov, ovariectomized females.

Extended Data Table 2 – related to Fig. 1B

Dendritic length

	CB	CN	DG	FC	OB	S1	SN
CB	1.000E+00	1.000E+00	3.910E-06	8.771E-05	2.755E-07	4.132E-11	1.396E-04
CN	1.000E+00	1.000E+00	3.612E-04	4.258E-03	3.982E-05	1.706E-08	5.711E-03
DG	3.910E-06	3.612E-04	1.000E+00	1.000E+00	1.000E+00	7.192E-01	1.000E+00
FC	8.771E-05	4.258E-03	1.000E+00	1.000E+00	1.000E+00	2.127E-01	1.000E+00
OB	2.755E-07	3.982E-05	1.000E+00	1.000E+00	1.000E+00	1.000E+00	1.000E+00
S1	4.132E-11	1.706E-08	7.192E-01	2.127E-01	1.000E+00	1.000E+00	2.595E-01
SN	1.396E-04	5.711E-03	1.000E+00	1.000E+00	1.000E+00	2.595E-01	1.000E+00

Number of branches

	CB	CN	DG	FC	OB	S1	SN
CB	1.000E+00	1.000E+00	1.533E-07	4.747E-05	4.124E-09	1.330E-10	2.383E-05
CN	1.000E+00	1.000E+00	2.932E-03	1.047E-01	2.475E-04	1.398E-05	5.860E-02
DG	1.533E-07	2.932E-03	1.000E+00	1.000E+00	1.000E+00	1.000E+00	1.000E+00
FC	4.747E-05	1.047E-01	1.000E+00	1.000E+00	1.000E+00	4.746E-01	1.000E+00
OB	4.124E-09	2.475E-04	1.000E+00	1.000E+00	1.000E+00	1.000E+00	1.000E+00
S1	1.330E-10	1.398E-05	1.000E+00	4.746E-01	1.000E+00	1.000E+00	9.989E-01
SN	2.383E-05	5.860E-02	1.000E+00	1.000E+00	1.000E+00	9.989E-01	1.000E+00

Number of branching points

	CB	CN	DG	FC	OB	S1	SN
CB	1.000E+00	1.000E+00	2.334E-07	4.446E-05	4.897E-09	1.197E-10	2.250E-05
CN	1.000E+00	1.000E+00	4.192E-03	1.066E-01	3.044E-04	1.424E-05	6.001E-02
DG	2.334E-07	4.192E-03	1.000E+00	1.000E+00	1.000E+00	1.000E+00	1.000E+00
FC	4.446E-05	1.066E-01	1.000E+00	1.000E+00	1.000E+00	4.721E-01	1.000E+00
OB	4.897E-09	3.044E-04	1.000E+00	1.000E+00	1.000E+00	1.000E+00	1.000E+00
S1	1.197E-10	1.424E-05	1.000E+00	4.721E-01	1.000E+00	1.000E+00	9.904E-01
SN	2.250E-05	6.001E-02	1.000E+00	1.000E+00	1.000E+00	9.904E-01	1.000E+00

Number of terminal points

	CB	CN	DG	FC	OB	S1	SN
CB	1.000E+00	1.000E+00	9.996E-08	4.816E-05	3.461E-09	1.479E-10	2.669E-05
CN	1.000E+00	1.000E+00	2.263E-03	1.079E-01	2.262E-04	1.563E-05	6.440E-02
DG	9.996E-08	2.263E-03	1.000E+00	1.000E+00	1.000E+00	1.000E+00	1.000E+00
FC	4.816E-05	1.079E-01	1.000E+00	1.000E+00	1.000E+00	4.903E-01	1.000E+00
OB	3.461E-09	2.262E-04	1.000E+00	1.000E+00	1.000E+00	1.000E+00	1.000E+00
S1	1.479E-10	1.563E-05	1.000E+00	4.903E-01	1.000E+00	1.000E+00	9.820E-01
SN	2.669E-05	6.440E-02	1.000E+00	1.000E+00	1.000E+00	9.820E-01	1.000E+00

Extended Data Table 2. Statistical tests related to Extended Data Figure 19A. P-value for pairwise comparisons between adult microglia of a brain regions for each morphometric. Cerebellum (CB), cochlear nucleus (CN), dentate gyrus (DG), frontal cortex (FC), olfactory bulb (OB), somatosensory cortex (S1), substantia nigra (SN).

Extended Data Table 3 – related to Extended Data Figure 21A

Process length

		♂				♀			
		Control	1 week	2 weeks	6 weeks	Control	1 week	2 weeks	6 weeks
♂	Control	1.00E+00	1.83E-17	1.28E-70	3.80E-131	1.00E+00	1.00E+00	8.40E-22	4.95E-85
	1 week	1.83E-17	1.00E+00	5.13E-03	1.27E-15	7.59E-23	1.90E-08	1.00E+00	4.46E-02
	2 weeks	1.28E-70	5.13E-03	1.00E+00	2.55E-08	6.97E-86	4.71E-28	1.29E-03	1.00E+00
	6 weeks	3.80E-131	1.27E-15	2.55E-08	1.00E+00	1.40E-151	3.74E-56	1.34E-18	3.16E-14
♀	Control	1.00E+00	7.59E-23	6.97E-86	1.40E-151	1.00E+00	3.39E-01	1.57E-28	4.04E-105
	1 week	1.00E+00	1.90E-08	4.71E-28	3.74E-56	3.39E-01	1.00E+00	1.01E-09	8.04E-28
	2 weeks	8.40E-22	1.00E+00	1.29E-03	1.34E-18	1.57E-28	1.01E-09	1.00E+00	1.39E-02
	6 weeks	4.95E-85	4.46E-02	1.00E+00	3.16E-14	4.04E-105	8.04E-28	1.39E-02	1.00E+00

Number of branches

		♂				♀			
		Control	1 week	2 weeks	6 weeks	Control	1 week	2 weeks	6 weeks
♂	Control	1.00E+00	1.83E-17	1.28E-70	3.80E-131	1.00E+00	1.00E+00	8.40E-22	4.95E-85
	1 week	1.83E-17	1.00E+00	5.13E-03	1.27E-15	7.59E-23	1.90E-08	1.00E+00	4.46E-02
	2 weeks	1.28E-70	5.13E-03	1.00E+00	2.55E-08	6.97E-86	4.71E-28	1.29E-03	1.00E+00
	6 weeks	3.80E-131	1.27E-15	2.55E-08	1.00E+00	1.40E-151	3.74E-56	1.34E-18	3.16E-14
♀	Control	1.00E+00	7.59E-23	6.97E-86	1.40E-151	1.00E+00	3.39E-01	1.57E-28	4.04E-105
	1 week	1.00E+00	1.90E-08	4.71E-28	3.74E-56	3.39E-01	1.00E+00	1.01E-09	8.04E-28
	2 weeks	8.40E-22	1.00E+00	1.29E-03	1.34E-18	1.57E-28	1.01E-09	1.00E+00	1.39E-02
	6 weeks	4.95E-85	4.46E-02	1.00E+00	3.16E-14	4.04E-105	8.04E-28	1.39E-02	1.00E+00

Number of branching points

		♂				♀			
		Control	1 week	2 weeks	6 weeks	Control	1 week	2 weeks	6 weeks
♂	Control	1.00E+00	9.96E-27	3.61E-100	1.32E-102	1.00E+00	3.66E-01	7.20E-24	1.00E-60
	1 week	9.96E-27	1.00E+00	1.31E-03	1.80E-04	3.13E-32	1.71E-10	1.00E+00	1.00E+00
	2 weeks	3.61E-100	1.31E-03	1.00E+00	1.00E+00	1.57E-115	3.17E-34	1.75E-08	2.01E-11
	6 weeks	1.32E-102	1.80E-04	1.00E+00	1.00E+00	8.55E-118	2.92E-36	8.83E-10	2.97E-13
♀	Control	1.00E+00	3.13E-32	1.57E-115	8.55E-118	1.00E+00	9.41E-03	9.93E-30	5.78E-75
	1 week	3.66E-01	1.71E-10	3.17E-34	2.92E-36	9.41E-03	1.00E+00	9.21E-08	3.02E-14
	2 weeks	7.20E-24	1.00E+00	1.75E-08	8.83E-10	9.93E-30	9.21E-08	1.00E+00	1.00E+00
	6 weeks	1.00E-60	1.00E+00	2.01E-11	2.97E-13	5.78E-75	3.02E-14	1.00E+00	1.00E+00

Number of terminal points

		♂				♀			
		Control	1 week	2 weeks	6 weeks	Control	1 week	2 weeks	6 weeks
♂	Control	1.00E+00	2.26E-27	7.97E-102	5.11E-100	1.00E+00	2.90E-01	1.68E-23	2.25E-60
	1 week	2.26E-27	1.00E+00	1.34E-03	7.40E-04	7.39E-33	1.26E-10	1.00E+00	1.00E+00
	2 weeks	7.97E-102	1.34E-03	1.00E+00	1.00E+00	4.22E-117	1.77E-34	4.68E-09	4.03E-12
	6 weeks	5.11E-100	7.40E-04	1.00E+00	1.00E+00	8.48E-115	8.97E-35	2.13E-09	1.82E-12
♀	Control	1.00E+00	7.39E-33	4.22E-117	8.48E-115	1.00E+00	7.28E-03	3.13E-29	2.27E-74
	1 week	2.90E-01	1.26E-10	1.77E-34	8.97E-35	7.28E-03	1.00E+00	2.01E-07	7.46E-14
	2 weeks	1.68E-23	1.00E+00	4.68E-09	2.13E-09	3.13E-29	2.01E-07	1.00E+00	1.00E+00
	6 weeks	2.25E-60	1.00E+00	4.03E-12	1.82E-12	2.27E-74	7.46E-14	1.00E+00	1.00E+00

Extended Data Table 3. Statistical tests related to Fig. 21A. P-value for pairwise comparison between microglia from the frontal cortex of the CK-p25 for different conditions and sex.

Extended Data Table 4 – related to Fig. 21B-D

EXTENDED LIST OF MORPHOMETRIC QUANTITIES

	L-measure metric	
1. Whole tree/microglia size		
Summed total process length	*Length*	*Total_Sum*
Number of process tips	*N_tips*	*Total_Sum*
Total process width	*Width*	*Total_Sum*
Total process height	*Height*	*Total_Sum*
Total process depth	*Depth*	*Total_Sum*
2. Bifurcation measures		
Average partition asymmetry	*Partition_Asymmetry*	*Average*
Average local amplitude angle	*Bif_ampl_local*	*Average*
Maximum local amplitude angle	*Bif_ampl_local*	*Maximum*
Average remote amplitude angle	*Bif_ampl_remote*	*Average*
Maximum remote amplitude angle	*Bif_ampl_remote*	*Maximum*
Average local tilt angle	*Bif_tilt_local*	*Average*
Maximum local tilt angle	*Bif_tilt_local*	*Maximum*
Average remote tilt angle	*Bif_tilt_remote*	*Average*
Maximum remote tilt angle	*Bif_tilt_remote*	*Maximum*
Average local torque angle	*Bif_torque_local*	*Average*
Maximum local torque angle	*Bif_torque_local*	*Maximum*
Average remote torque angle	*Bif_torque_remote*	*Average*
Maximum remote torque angle	*Bif_torque_remote*	*Maximum*
3. Process measures		
Average tortuosity	*Contraction*	*Average*
Average fractal dimension	*Fractal_Dim*	*Average*
Maximum fractal dimension	*Fractal_Dim*	*Maximum*
Average branch path length	*Branch_pathlength*	*Average*
Maximum branch path length	*Branch_pathlength*	*Maximum*
4. Compartment measures		
Maximum branch order	*Branch_Order*	*Maximum*
Average terminal degree	*Terminal_degree*	*Average*
Maximum path distance from soma	*PathDistance*	*Maximum*
Maximum branch helicity	*Helix*	*Maximum*

Extended Data Table 4. Classical morphometric related to Extended Data Figure 19B-D. Extended list of classical morphometric quantities [208,265]

Extended Data Table 5. Number of animals used

	Condition	Time point	♂	♀	♀ov
Cerebellum (CB)	Adult	8-12 weeks	12	9	4
	Develop-ment	P7	3	3	
		P15	3	3	
		P22	3	3	
	5xFAD	3 months	3	3	
		6 months	3	3	
	CK-p25	1 week	3	3	
		2 weeks	2	3	
		6 weeks	3	3	

	Condition	Time point	♂	♀	♀ov
Cochlear nucleus (CN)	Adult	8-12 weeks	8	12	4
	Develop-ment	P7	3	3	
		P15	3	3	
		P22	3	3	
	5xFAD	3 months	3	3	
		6 months	3	3	
	CK-p25	1 week	3	3	
		2 weeks	4	3	
		6 weeks	3	3	

Frontal cortex (FC)	Adult	8-12 weeks	12	12	4
	Develop-ment	P7	3	3	
		P15	3	3	
		P22	3	3	
	5xFAD	3 months	3	2	
		6 months	2	3	
	CK-p25	1 week	2	3	
		2 weeks	5	3	
		6 weeks	4	5	

Dentate gyrus (DG)	Adult	8-12 weeks	11	11	4
	Develop-ment	P7	3	3	
		P15	3	3	
		P22	3	3	
	5xFAD	3 months	3	3	
		6 months	3	3	
	CK-p25	1 week	4	3	
		2 weeks	3	3	
		6 weeks	5	7	

Olfactory bulb (OB)	Adult	8-12 weeks	12	12	4
	Develop-ment	P7	3	3	
		P15	3	3	
		P22	3	3	
	5xFAD	3 months	2	4	
		6 months	3	4	
	CK-p25	1 week	2	2	
		2 weeks	4	4	
		6 weeks	3	3	

Somatosensory cortex (S1)	Adult	8-12 weeks	10	10	4
	Develop-ment	P7	3	3	
		P15	3	3	
		P22	3	3	
	5xFAD	3 months	4	3	
		6 months	3	3	
	CK-p25	1 week	3	3	
		2 weeks	3	3	
		6 weeks	5	4	
	KXA	1x KXA	3	3	
		2x KXA	3	3	
		3x KXA	3	3	
	Recovery after 3x KXA	3 days	3	3	
		1-week	3	3	
		2-weeks	3	3	

Substantia nigra (SN)	Adult	8-12 weeks	10	10	4
	Develop-ment	P7	3	3	
		P15	3	3	
		P22	4	2	
	5xFAD	3 months	3	3	
		6 months	3	3	
	CK-p25	1 week	3	3	
		2 weeks	4	3	
		6 weeks	3	4	

Extended Data Table 5. Number of animals used. Total number of animals used per condition. ♀ov, ovariectomized females.

a. Data availability.

The .swc files generated during the current study are available in the NeuroMorpho.org repository, https://neuromorpho.org/KeywordResult.jsp?keywords=%22siegert%22

b. Code availability.

The codes and the reference atlas are available as download on GitHub (https://git.ist.ac.at/rcubero/morphomics), with detailed instructions on implementation.

12 References

1. Ginhoux, F., Lim, S., Hoeffel, G., Low, D. & Huber, T. Origin and differentiation of microglia. *Front. Cell. Neurosci.* **0**, 45 (2013).
2. Rio-Hortega, P. Del. THE MICROGLIA. *Lancet* **233**, 1023–1026 (1939).
3. Del Rio-Hortega, P. Vista de Lo que debe entenderse por «tercer elemento» de los centros nerviosos. *Boll. Socieded Esp* **9**, 69–120 (1919).
4. Boullerne, A. I. & Feinstein, D. L. History of Neuroscience I. P ıo del R ıo-Hortega (1882-1945): The Discoverer of Microglia and Oligodendroglia. *Am. Soc. Neurochem.* **12**, 1–3 (2020).
5. Kettenmann, H., Hanisch, U.-K., Noda, M. & Verkhratsky, A. Physiology of Microglia. *Physiol. Rev.* **91**, 461–553 (2011).
6. Hart, A. D., Wyttenbach, A., Hugh Perry, V. & Teeling, J. L. Age related changes in microglial phenotype vary between CNS regions: Grey versus white matter differences. *Brain. Behav. Immun.* **26**, 754 (2012).
7. Yang, T. T. *et al.* Differential distribution and activation of microglia in the brain of male C57BL/6J mice. *Brain Struct. Funct.* **218**, 1051–1060 (2013).
8. Matcovitch-Natan, O. *et al.* Microglia development follows a stepwise program to regulate brain homeostasis. *Science (80-.).* (2016). doi:10.1126/science.aad8670
9. Masuda, T., Sankowski, R., Staszewski, O. & Prinz, M. Microglia Heterogeneity in the Single-Cell Era. *Cell Reports* **30**, 1271–1281 (2020).
10. Hashemiaghdam, A. & Mroczek, M. Microglia heterogeneity and neurodegeneration: The emerging paradigm of the role of immunity in Alzheimer's disease. *J. Neuroimmunol.* **341**, (2020).
11. Masuda, T. *et al.* Spatial and temporal heterogeneity of mouse and human microglia at single-cell resolution. *Nature* 1 (2019). doi:10.1038/s41586-019-0924-x
12. Lawson, L. J., Perry, V. H., Dri, P. & Gordon, S. Heterogeneity in the distribution and morphology of microglia in the normal adult mouse brain. *Neuroscience* **39**, 151–170 (1990).
13. Stogsdill, J. A. *et al.* Pyramidal neuron subtype diversity governs microglia states in the neocortex. | *Nat.* | **608**, (2022).
14. Ginhoux, F. & Prinz, M. Origin of Microglia: Current Concepts and Past Controversies. *Cold Spring Harb. Perspect. Biol.* **7**, (2015).
15. Hammond, T. R. *et al.* Single-Cell RNA Sequencing of Microglia throughout the Mouse Lifespan and in the Injured Brain Reveals Complex Cell-State Changes. *Immunity* (2019). doi:10.1016/j.immuni.2018.11.004
16. Palis, J. & Yoder, M. C. Yolk-sac hematopoiesis: The first blood cells of mouse and man. *Exp. Hematol.* **29**, 927–936 (2001).
17. Elmore, M. R. P. *et al.* Colony-stimulating factor 1 receptor signaling is necessary for microglia viability, unmasking a microglia progenitor cell in the adult brain. *Neuron* **82**, 380–397 (2014).
18. Zhong, L. *et al.* TREM2/DAP12 Complex Regulates Inflammatory Responses in Microglia via the JNK Signaling Pathway. *Front. Aging Neurosci.* **9**, (2017).
19. Masuda, T. *et al.* IRF8 Is a Critical Transcription Factor for Transforming Microglia into a Reactive Phenotype. *Cell Rep.* **1**, 334–340 (2012).
20. Smith, A. M. *et al.* The Transcription Factor PU.1 is Critical for Viability and Function of Human Brain Microglia. doi:10.1002/glia.22486
21. Dorman, L. C. & Molofsky, A. V. Demystifying Microglia: And Now the Work Begins. *Immunity* **50**, 11–13 (2019).
22. Vainchtein, I. D. *et al.* Astrocyte-derived interleukin-33 promotes microglial synapse

engulfment and neural circuit development. *Science* **359**, 1269–1273 (2018).
23. Hong, S. & Stevens, B. Microglia: Phagocytosing to Clear, Sculpt, and Eliminate. *Developmental Cell* **38**, 126–128 (2016).
24. Kracht, L. *et al.* Human fetal microglia acquire homeostatic immune-sensing properties early in development. *Science (80-.).* **369**, 530–537 (2020).
25. Caggiano, A. O. & Brunjes, P. C. Microglia and the developing olfactory bulb. *Neuroscience* **52**, 717–724 (1993).
26. Fiske, B. K. & Brunjes, P. C. Microglial activation in the developing rat olfactory bulb. *Neuroscience* **96**, 807–815 (2000).
27. Holcomb, P. S. *et al.* Synaptic Inputs Compete during Rapid Formation of the Calyx of Held: A New Model System for Neural Development. *J. Neurosci.* **33**, 12954 (2013).
28. Dinh, M. L., Koppel, S. J., Korn, M. J. & Cramer, K. S. Distribution of glial cells in the auditory brainstem: normal development and effects of unilateral lesion. *Neuroscience* **278**, 237–252 (2014).
29. Nakayama, H. *et al.* Microglia permit climbing fiber elimination by promoting GABAergic inhibition in the developing cerebellum. *Nat. Commun. 2018 91* **9**, 1–15 (2018).
30. Ueno, M. *et al.* Layer V cortical neurons require microglial support for survival during postnatal development. *Nat. Neurosci. 2013 165* **16**, 543–551 (2013).
31. Ferrini, F. & De Koninck, Y. Microglia Control Neuronal Network Excitability via BDNF Signalling. *Neural Plast.* **2013**, 11 (2013).
32. Trang, T., Beggs, S. & Salter, M. W. Brain-Derived Neurotrophic Factor from Microglia: A Molecular Substrate for Neuropathic Pain. *Neuron Glia Biol.* **7**, 99 (2011).
33. Cramer, T. *et al.* Cross-talk between GABAergic postsynapse and microglia regulate synapse loss after brain ischemia. *Sci. Adv* **8**, 112 (2022).
34. Hagemeyer, N. *et al.* Microglia contribute to normal myelinogenesis and to oligodendrocyte progenitor maintenance during adulthood. *Acta Neuropathol.* **134**, 441 (2017).
35. Wlodarczyk, A. *et al.* A novel microglial subset plays a key role in myelinogenesis in developing brain. *EMBO J.* **36**, 3292–3308 (2017).
36. Cunningham, C. L., Martínez-Cerdeño, V. & Noctor, S. C. Microglia Regulate the Number of Neural Precursor Cells in the Developing Cerebral Cortex. *J. Neurosci.* **33**, 4216–4233 (2013).
37. Frick, L. R., Williams, K. & Pittenger, C. Microglial Dysregulation in Psychiatric Disease. *Clin. Dev. Immunol.* **2013**, (2013).
38. Prinz, M. & Priller, J. Microglia and brain macrophages in the molecular age: from origin to neuropsychiatric disease. (2014). doi:10.1038/nrn3722
39. Hollingworth, P. *et al.* Common variants at ABCA7, MS4A6A/MS4A4E, EPHA1, CD33 and CD2AP are associated with Alzheimer's disease. *Nat. Genet.* **43**, 429–436 (2011).
40. Guerreiro, R. *et al.* TREM2 Variants in Alzheimer's Disease . *N. Engl. J. Med.* **368**, 117–127 (2013).
41. Schmechel, D. E. *et al.* Increased amyloid ,8-peptide deposition in cerebral cortex as a consequence of apolipoprotein E genotype in late-onset Alzheimer disease (phenotype/APOE4 gene). *Proc. Natl. Acad. Sci. USA* **90**, 9649–9653 (1993).
42. Tiraboschi, P. *et al.* Impact of APOE genotype on neuropathologic and neurochemical markers of Alzheimer disease. *Neurology* **62**, 1977–1983 (2004).
43. Hashimoto, T. *et al.* Apolipoprotein E, Especially Apolipoprotein E4, Increases the Oligomerization of Amyloid β Peptide. *J. Neurosci.* **32**, 15181–15192 (2012).
44. Koffie, R. M. *et al.* Apolipoprotein E4 effects in Alzheimer's disease are mediated by

synaptotoxic oligomeric amyloid-β. *Brain* **135**, 2155–2168 (2012).
45. Fagan, A. M. *et al.* Human and Murine ApoE Markedly Alters Aβ Metabolism before and after Plaque Formation in a Mouse Model of Alzheimer's Disease. *Neurobiol. Dis.* **9**, 305–318 (2002).
46. Holtzman, D. M. *et al.* Expression of human apolipoprotein E reduces amyloid-β deposition in a mouse model of Alzheimer's disease. *J. Clin. Invest.* **103**, R15–R21 (1999).
47. Castellano, J. M. *et al.* Human apoE isoforms differentially regulate brain amyloid-β peptide clearance. *Sci. Transl. Med.* **3**, (2011).
48. DeMattos, R. B. *et al.* ApoE and Clusterin Cooperatively Suppress Aβ Levels and Deposition: Evidence that ApoE Regulates Extracellular Aβ Metabolism In Vivo. *Neuron* **41**, 193–202 (2004).
49. Sieber, M. W. *et al.* Attenuated Inflammatory Response in Triggering Receptor Expressed on Myeloid Cells 2 (TREM2) Knock-Out Mice following Stroke. *PLoS One* **8**, e52982 (2013).
50. Bouchon, A., Hernández-Munain, C., Cella, M. & Colonna, M. A Dap12-Mediated Pathway Regulates Expression of Cc Chemokine Receptor 7 and Maturation of Human Dendritic Cells. *J. Exp. Med.* **194**, 1111–1122 (2001).
51. Takahashi, K., Rochford, C. D. P. & Neumann, H. Clearance of apoptotic neurons without inflammation by microglial triggering receptor expressed on myeloid cells-2. *J. Exp. Med.* **201**, 647–657 (2005).
52. Piccio, L. *et al.* Blockade of TREM-2 exacerbates experimental autoimmune encephalomyelitis. *Eur. J. Immunol.* **37**, 1290–1301 (2007).
53. Keren-Shaul, H. *et al.* A Unique Microglia Type Associated with Restricting Development of Alzheimer's Disease. *Cell* **169**, 1276-1290.e17 (2017).
54. Schlachetzki, J. C. M. & Hull, M. Microglial Activation in Alzheimer's Disease. *Curr. Alzheimer Res.* **6**, 554–563 (2009).
55. Ferrera, D., Mazzaro, N., Canale, C. & Gasparini, L. Resting microglia react to Aβ42 fibrils but do not detect oligomers or oligomer-induced neuronal damage. *Neurobiol. Aging* **35**, 2444–2457 (2014).
56. Tükel, Ç. *et al.* Responses to Amyloids of Microbial and Host Origin Are Mediated through Toll-like Receptor 2. *Cell Host Microbe* **6**, 45–53 (2009).
57. Halle, A. *et al.* The NALP3 inflammasome is involved in the innate immune response to amyloid-β. *Nat. Immunol. 2008 98* **9**, 857–865 (2008).
58. Lee, J. H. *et al.* Lysosomal Proteolysis and Autophagy Require Presenilin 1 and Are Disrupted by Alzheimer-Related PS1 Mutations. *Cell* **141**, 1146–1158 (2010).
59. Nixon, R. A. *et al.* Extensive Involvement of Autophagy in Alzheimer Disease: An Immuno-Electron Microscopy Study. *J. Neuropathol. Exp. Neurol.* **64**, 113–122 (2005).
60. Scheiblich, H. *et al.* Microglia jointly degrade fibrillar alpha-synuclein cargo by distribution through tunneling nanotubes. *Cell* **184**, 5089-5106.e21 (2021).
61. Henstridge, C. M., Tzioras, M. & Paolicelli, R. C. Glial contribution to excitatory and inhibitory synapse loss in neurodegeneration. *Front. Cell. Neurosci.* **13**, 63 (2019).
62. Leong, S.-K. & Ling, E.-A. *Amoeboid and Ramified Microglia: Their Interrelationship and Response to Brain Injury*. *GLIA* **6**, (1992).
63. Colton, C. A. Heterogeneity of Microglial Activation in the Innate Immune Response in the Brain. *J. Neuroimmune Pharmacol. 2009 44* **4**, 399–418 (2009).
64. Cherry, J. D., Olschowka, J. A. & O'Banion, M. K. Neuroinflammation and M2 microglia: The good, the bad, and the inflamed. *J. Neuroinflammation* **11**, 1–15 (2014).
65. Malyshev, I. & Malyshev, Y. Current Concept and Update of the Macrophage Plasticity Concept: Intracellular Mechanisms of Reprogramming and M3 Macrophage 'Switch'

Phenotype. *Biomed Res. Int.* **2015**, (2015).
66. Walker, D. G. & Lue, L. F. Immune phenotypes of microglia in human neurodegenerative disease: challenges to detecting microglial polarization in human brains. *Alzheimers. Res. Ther.* **7**, (2015).
67. Benusa, S. D., George, N. M. & Dupree, J. L. Microglial heterogeneity: distinct cell types or differential functional adaptation? *Neuroimmunol. Neuroinflammation* **7**, 248–263 (2020).
68. Mildner, A. *et al.* Distinct and non-redundant roles of microglia and myeloid subsets in mouse models of Alzheimer's disease. *J. Neurosci.* **31**, 11159–11171 (2011).
69. Furube, E., Kawai, S., Inagaki, H., Takagi, S. & Miyata, S. Brain Region-dependent Heterogeneity and Dose-dependent Difference in Transient Microglia Population Increase during Lipopolysaccharide-induced Inflammation. *Sci. Rep.* **8**, (2018).
70. Grabert, K. *et al.* Microglial brain regionâ 'dependent diversity and selective regional sensitivities to aging. *Nat. Neurosci.* (2016). doi:10.1038/nn.4222
71. Tan, Y. L., Yuan, Y. & Tian, L. Microglial regional heterogeneity and its role in the brain. *Mol. Psychiatry 2019 252* **25**, 351–367 (2019).
72. Keren-Shaul, H. *et al.* A Unique Microglia Type Associated with Restricting Development of Alzheimer's Disease. *Cell* **169**, 1276-1290.e17 (2017).
73. Sala Frigerio, C. *et al.* The Major Risk Factors for Alzheimer's Disease: Age, Sex, and Genes Modulate the Microglia Response to Aβ Plaques. *Cell Rep.* **27**, 1293-1306.e6 (2019).
74. Srinivasan, K. *et al.* Alzheimer's Patient Microglia Exhibit Enhanced Aging and Unique Transcriptional Activation. *Cell Rep.* **31**, (2020).
75. Absinta, M. *et al.* A lymphocyte-microglia-astrocyte axis in chronic active multiple sclerosis. *Nature* **597**, (2021).
76. Marschallinger, J. *et al.* Lipid-droplet-accumulating microglia represent a dysfunctional and proinflammatory state in the aging brain. *Nat. Neurosci.* **23**, 194–208 (2020).
77. Safaiyan, S. *et al.* White matter aging drives microglial diversity. *Neuron* **109**, 1100-1117.e10 (2021).
78. Hammond, T. R., Robinton, D. & Stevens, B. Microglia and the Brain: Complementary Partners in Development and Disease. *Annu. Rev. Cell Dev. Biol.* (2018). doi:10.1146/annurev-cellbio-100616-060509
79. Li, Q. *et al.* Developmental heterogeneity of microglia and brain myeloid cells revealed by deep single-cell RNA sequencing. *bioRxiv* (2018). doi:10.1101/406363
80. Fonseca, R. S. *et al.* Neurogenic Niche Microglia Undergo Positional Remodeling and Progressive Activation Contributing to Age-Associated Reductions in Neurogenesis. *Stem Cells Dev.* **25**, (2016).
81. Paolicelli, R. *et al.* Defining Microglial States and Nomenclature: A Roadmap to 2030. *SSRN Electron. J.* (2022). doi:10.2139/SSRN.4065080
82. Hanamsagar, R. *et al.* Generation of a microglial developmental index in mice and in humans reveals a sex difference in maturation and immune reactivity. *Glia* **65**, 1504–1520 (2017).
83. Guneykaya, D. *et al.* Transcriptional and Translational Differences of Microglia from Male and Female Brains. *Cell Rep.* **24**, 2773-2783.e6 (2018).
84. Thion, M. S. *et al.* Microbiome Influences Prenatal and Adult Microglia in a Sex-Specific Manner. *Cell* **172**, 500-516.e16 (2018).
85. Villa, A. *et al.* Sex-Specific Features of Microglia from Adult Mice. *Cell Rep.* **23**, 3501–3511 (2018).
86. Nelson, L. H., Saulsbery, A. I. & Lenz, K. M. Small cells with big implications: Microglia and sex differences in brain development, plasticity and behavioral health.

Prog. Neurobiol. **176**, 103 (2019).
87. Song, W. M. & Colonna, M. The identity and function of microglia in neurodegeneration. *Nat. Immunol. 2018 1910* **19**, 1048–1058 (2018).
88. Lenz, K. M. & McCarthy, M. M. A Starring Role for Microglia in Brain Sex Differences. *Neurosci.* **2**, 306–321 (2015).
89. Schwarz, J. M., Sholar, P. W. & Bilbo, S. D. Sex differences in microglial colonization of the developing rat brain. *J. Neurochem.* **120**, 948–963 (2012).
90. Nelson, L. H., Warden, S. & Lenz, K. M. Sex differences in microglial phagocytosis in the neonatal hippocampus. *Brain. Behav. Immun.* **64**, 11–22 (2017).
91. Yanguas-Casás, N. *et al.* Sex differences in the phagocytic and migratory activity of microglia and their impairment by palmitic acid. *Glia* **66**, 522–537 (2018).
92. Caplan, H. W., Cox, C. S. & Bedi, S. S. Do microglia play a role in sex differences in TBI? *J. Neurosci. Res.* **95**, 509–517 (2017).
93. Mouton, P. R. *et al.* Age and gender effects on microglia and astrocyte numbers in brains of mice. *Brain Res.* **956**, 30–35 (2002).
94. Amateau, S. K. & McCarthy, M. M. Induction of PGE2 by estradiol mediates developmental masculinization of sex behavior. *Nat. Neurosci.* **7**, 643–650 (2004).
95. Vegeto, E. *et al.* Estrogen prevents the lipopolysaccharide-induced inflammatory response in microglia. *J. Neurosci.* **21**, 1809–1818 (2001).
96. Villa, A., Rizzi, N., Vegeto, E., Ciana, P. & Maggi, A. Estrogen accelerates the resolution of inflammation in macrophagic cells. *Sci. Rep.* **5**, (2015).
97. Loram, L. C. *et al.* Sex and estradiol influence glial pro-inflammatory responses to lipopolysaccharide in rats. *Psychoneuroendocrinology* **37**, (2012).
98. Rettew, J. A., Huet, Y. M. & Marriott, I. Estrogens augment cell surface TLR4 expression on murine macrophages and regulate sepsis susceptibility in vivo. *Endocrinology* **150**, 3877–3884 (2009).
99. Vegeto, E., Ciana, P. & Maggi, A. Estrogen and inflammation: hormone generous action spreads to the brain. *Mol. Psychiatry* **7**, 236–238 (2002).
100. Vegeto, E. *et al.* The endogenous estrogen status regulates microglia reactivity in animal models of neuroinflammation. *Endocrinology* **147**, 2263–2272 (2006).
101. Hestrin, S. & Armstrong, W. E. Morphology and Physiology of Cortical Neurons in Layer I. *J. Neurosci.* **16**, 5290–5300 (1996).
102. Hübener, M. & Bolz, J. Morphology of identified projection neurons in layer 5 of rat visual cortex. *Neurosci. Lett.* **94**, 76–81 (1988).
103. del Rio-Hortega, P. El tercer elemento de los centros nerviosos: histogénesis y evolución normal; éxodo y distribución regional de la microglia. *Memorias la Real Soc. Española Hist. Nat.* (1921).
104. Ito, D. *et al.* Microglia-specific localisation of a novel calcium binding protein, Iba1. *Mol. Brain Res.* **57**, 1–9 (1998).
105. Carson, M. J., Reilly, C. R., Sutcliffe, J. G. & Lo, D. *Mature Microglia Resemble Immature Antigen-Presenting Cells*.
106. Harrison, J. K. *et al.* Role for neuronally derived fractalkine in mediating interactions between neurons and CX3CR1-expressing microglia. *Proc. Natl. Acad. Sci.* **95**, 10896–10901 (1998).
107. Sedgwick, J. D. *et al.* Isolation and direct characterization of resident microglial cells from the normal and inflamed central nervous system. *Proc. Natl. Acad. Sci.* **88**, 7438–7442 (1991).
108. Cserép, C. *et al.* Microglia monitor and protect neuronal function through specialized somatic purinergic junctions. *Science (80-.).* **367**, 528–537 (2020).
109. Satoh, J. ichi *et al.* TMEM119 marks a subset of microglia in the human brain.

Neuropathology **36**, 39–49 (2016).
110. Lee, M., Lee, Y., Song, J., Lee, J. & Chang, S. Y. Tissue-specific Role of CX3CR1 Expressing Immune Cells and Their Relationships with Human Disease. *Immune Netw.* **18**, (2018).
111. Karlstetter, M., Ebert, S. & Langmann, T. Microglia in the healthy and degenerating retina: Insights from novel mouse models. *Immunobiology* **215**, 685–691 (2010).
112. Nimmerjahn, A., Kirchhoff, F. & Helmchen, F. Resting Microglial Cells Are Highly Dynamic Surveillants of Brain Parenchyma in Vivo. *Science (80-.).* **308**, 1314–1318 (2005).
113. Davalos, D. *et al.* Stable in vivo imaging of densely populated glia, axons and blood vessels in the mouse spinal cord using two-photon microscopy. *J. Neurosci. Methods* **169**, 1–7 (2008).
114. Grabert, K. *et al.* Microglial brain regionâ 'dependent diversity and selective regional sensitivities to aging. *Nat. Neurosci.* **19**, 504–516 (2016).
115. Lenz, K. M. & Nelson, L. H. Microglia and beyond: Innate immune cells as regulators of brain development and behavioral function. *Front. Immunol.* **9**, 698 (2018).
116. Stratoulias, V., Venero, J. L., Tremblay, M. & Joseph, B. Microglial subtypes: diversity within the microglial community. *EMBO J.* **38**, (2019).
117. Venturino, A. *et al.* Microglia enable mature perineuronal nets disassembly upon anesthetic ketamine exposure or 60-Hz light entrainment in the healthy brain. *Cell Rep.* **36**, (2021).
118. Wada, R., Tifft, C. J. & Proia, R. L. Microglial activation precedes acute neurodegeneration in Sandhoff disease and is suppressed by bone marrow transplantation. *Proc. Natl. Acad. Sci. U. S. A.* **97**, 10954 (2000).
119. Ponomarev, E. D., Shriver, L. P., Maresz, K. & Dittel, B. N. Microglial cell activation and proliferation precedes the onset of CNS autoimmunity. *J. Neurosci. Res.* **81**, 374–389 (2005).
120. Wu', C. H., Wen', C. Y., Shieh, J. Y. & Ling2, E. A. A quantitative and morphometric study of the transformation of amoeboid microglia into ramified microglia in the developing corpus callosum in rats. *J. Anathomy* **181**, 423–430 (1992).
121. Sholl, D. A. Dendritic organization in the neurons of the visual and motor cortices of the cat. *J. Anat.* **87**, 387 (1953).
122. Soltys, Z. *et al.* Quantitative morphological study of microglial cells in the ischemic rat brain using principal component analysis. *J. Neurosci. Methods* **146**, 50–60 (2005).
123. Kozlowski, C. & Weimer, R. M. An automated method to quantify microglia morphology and application to monitor activation state longitudinally in vivo. *PLoS One* **7**, (2012).
124. Valous, N. A., Lahrmann, B., Zhou, W., Veltkamp, R. & Grabe, N. Multistage histopathological image segmentation of Iba1-stained murine microglias in a focal ischemia model: Methodological workflow and expert validation. *J. Neurosci. Methods* **213**, 250–262 (2013).
125. Lu, Y. *et al.* Quantitative profiling of microglia populations using harmonic co-clustering of arbor morphology measurements. *Proc. - Int. Symp. Biomed. Imaging* 1360–1363 (2013). doi:10.1109/ISBI.2013.6556785
126. Xu, Y. *et al.* Unsupervised inference of arbor morphology progression for microglia from confocal microscope images. *Proc. - Int. Symp. Biomed. Imaging* 1356–1359 (2013). doi:10.1109/ISBI.2013.6556784
127. Kongsui, R., Beynon, S. B., Johnson, S. J. & Walker, F. R. Quantitative assessment of microglial morphology and density reveals remarkable consistency in the distribution and morphology of cells within the healthy prefrontal cortex of the rat. *J.*

Neuroinflammation **11**, 1–9 (2014).
128. Del Mar Fernández-Arjona, M. *et al.* Microglia Morphological Categorization in a Rat Model of Neuroinflammation by Hierarchical Cluster and Principal Components Analysis. (2017). doi:10.3389/fncel.2017.00235
129. Ding, Y. *et al.* Novel Methods for Microglia Segmentation, Feature Extraction, and Classification. *IEEE/ACM Trans. Comput. Biol. Bioinforma.* **14**, 1366–1377 (2017).
130. Healy, S., McMahon, J., Owens, P., Dockery, P. & FitzGerald, U. Threshold-based segmentation of fluorescent and chromogenic images of microglia, astrocytes and oligodendrocytes in FIJI. *J. Neurosci. Methods* **295**, 87–103 (2018).
131. Salamanca, L. *et al.* MIC-MAC: An automated pipeline for high-throughput characterization and classification of three-dimensional microglia morphologies in mouse and human postmortem brain samples. *Glia* **67**, 1496–1509 (2019).
132. Leyh, J. *et al.* Classification of Microglial Morphological Phenotypes Using Machine Learning. *Front. Cell. Neurosci.* **15**, (2021).
133. Ash, N. F., Massengill, M. T., Harmer, L., Jafri, A. & Lewin, A. S. Automated segmentation and analysis of retinal microglia within ImageJ. *Experimental Eye Research* **203**, 108416 (2021).
134. Clarke, D., Crombag, H. S. & Hall, C. N. An open-source pipeline for analysing changes in microglial morphology. *Open Biol.* **11**, (2021).
135. Silburt, J. & Aubert, I. MORPHIOUS: an unsupervised machine learning workflow to detect the activation of microglia and astrocytes. *J. Neuroinflammation* **19**, 24 (2021).
136. Choi, S. *et al.* Automated characterisation of microglia in ageing mice using image processing and supervised machine learning algorithms. *Sci. Reports 2022 121* **12**, 1–12 (2022).
137. Rouchdy, Y. & Cohen, L. D. The shading zone problem in geodesic voting and its solutions for the segmentation of tree structures. Application to the segmentation of Microglia extensions. 66–71 (2010). doi:10.1109/CVPRW.2009.5204046
138. Kanari, L. *et al.* A Topological Representation of Branching Neuronal Morphologies. *Neuroinformatics 2017 161* **16**, 3–13 (2017).
139. Clarke, D., Crombag, H. S. & Hall, C. N. An Open-Source Pipeline for Analyzing Changes In Microglial Morphology Running Title: Open-Source Microglia Analysis. *bioRxiv* 2021.01.12.426422 (2021). doi:10.1101/2021.01.12.426422
140. Scorcioni, R., Polavaram, S. & Ascoli, G. A. L-Measure: a Web-accessible tool for the analysis, comparison, and search of digital reconstructions of neuronal morphologies. *Nat. Protoc.* **3**, 866 (2008).
141. Loussaief, S. & Abdelkrim, A. Machine learning framework for image classification. *2016 7th Int. Conf. Sci. Electron. Technol. Inf. Telecommun. SETIT 2016* 58–61 (2017). doi:10.1109/SETIT.2016.7939841
142. Kanari, L. *et al.* Objective Classification of Neocortical Pyramidal Cells. *bioRxiv* (2018). doi:10.1101/349977
143. Gouwens, N. W. *et al.* Classification of electrophysiological and morphological neuron types in the mouse visual cortex. *Nat. Neurosci. 2019 227* **22**, 1182–1195 (2019).
144. Morrison, H. W. & Filosa, J. A. A quantitative spatiotemporal analysis of microglia morphology during ischemic stroke and reperfusion. *J. Neuroinflammation* **10**, 1–20 (2013).
145. Heindl, S. *et al.* Automated morphological analysis of microglia after stroke. *Front. Cell. Neurosci.* **12**, (2018).
146. Bachstetter, A. D. *et al.* Disease-related microglia heterogeneity in the hippocampus of Alzheimer's disease, dementia with Lewy bodies, and hippocampal sclerosis of aging. *Acta Neuropathol. Commun.* (2015). doi:10.1186/s40478-015-0209-z

147. Paolicelli, R. C. *et al.* Synaptic Pruning by Microglia Is Necessary for Normal Brain Development. *Science (80-.).* **333**, 1456–1458 (2011).
148. Pont-Lezica, L., Béchade, C., Belarif-Cantaut, Y., Pascual, O. & Bessis, A. Physiological roles of microglia during development. *J. Neurochem.* **119**, 901–908 (2011).
149. Carlsson, G. *Topology and data. Bulletin od the American Mathematical Society*. *BULLETIN (New Series) OF THE AMERICAN MATHEMATICAL SOCIETY* **46**, (2009).
150. Li, Y., Wang, D., Ascoli, G. A., Mitra, P. & Wang, Y. Metrics for comparing neuronal tree shapes based on persistent homology. *PLoS One* **12**, e0182184 (2017).
151. Cruz, J. C., Tseng, H. C., Goldman, J. A., Shih, H. & Tsai, L. H. Aberrant Cdk5 activation by p25 triggers pathological events leading to neurodegeneration and neurofibrillary tangles. *Neuron* **40**, 471–483 (2003).
152. Cruz, J. C. *et al.* p25/cyclin-dependent kinase 5 induces production and intraneuronal accumulation of amyloid β in vivo. *J. Neurosci.* **26**, 10536–10541 (2006).
153. Fischer, A., Sananbenesi, F., Pang, P. T., Lu, B. & Tsai, L. H. Opposing roles of transient and prolonged expression of p25 in synaptic plasticity and hippocampus-dependent memory. *Neuron* **48**, 825–838 (2005).
154. Erny, D. *et al.* Host microbiota constantly control maturation and function of microglia in the CNS. *Nat. Neurosci. 2015 187* **18**, 965–977 (2015).
155. Venturino, A. & Siegert, S. Minimally invasive protocols and quantification for microglia-mediated perineuronal net disassembly in mouse brain. *STAR Protoc.* **2**, 101012 (2021).
156. Lein, E. S. *et al.* Genome-wide atlas of gene expression in the adult mouse brain. *Nat. 2006 4457124* **445**, 168–176 (2006).
157. Stockley, E., Cole, H., Brown, A. & Wheal, H. A system for quantitative morphological measurement and electronic modelling of neurons: three-dimensional reconstruction. *J. Neurosci. Methods* **47**, 39–51 (1993).
158. Mcinnes, L., Healy, J. & Melville, J. UMAP: Uniform Manifold Approximation and Projection for Dimension Reduction. (2020).
159. Setty, M. *et al.* Characterization of cell fate probabilities in single-cell data with Palantir. *Nat. Biotechnol.* **37**, 451–460 (2019).
160. Nowotschin, S. *et al.* The emergent landscape of the mouse gut endoderm at single-cell resolution. *Nat. 2019 5697756* **569**, 361–367 (2019).
161. Cao, J. *et al.* The single-cell transcriptional landscape of mammalian organogenesis. *Nat. 2019 5667745* **566**, 496–502 (2019).
162. Riihimäki, H. & Chacholski, W. Generalized persistence analysis based on stable rank invariant. (2018).
163. Agerberg, J., Ramanujam, R., Scolamiero, M. & Chachólski, W. Supervised Learning Using Homology Stable Rank Kernels. *Front. Appl. Math. Stat.* **0**, 39 (2021).
164. Braak, H., Braak, E., Bohl, J. & Lang, W. Alzheimer's disease: amyloid plaques in the cerebellum. *J. Neurol. Sci.* **93**, 277–287 (1989).
165. Jacobs, H. I. L. *et al.* The cerebellum in Alzheimer's disease: evaluating its role in cognitive decline. *Brain* **141**, 37–47 (2018).
166. Sinha, U. K., Hollen, K. M., Rodriguez, R. & Miller, C. A. Auditory system degeneration in Alzheimer's disease. *Neurology* **43**, 779–779 (1993).
167. Larner, A. J. The Cerebellum in Alzheimer's Disease. *Dement. Geriatr. Cogn. Disord.* **8**, 203–209 (1997).
168. Ohm, T. G. & Braak, H. Auditory brainstem nuclei in Alzheimer's disease. *Neurosci. Lett.* **96**, 60–63 (1989).

169. Kazee, A. M., Cox, C. & Richfield, E. K. Substantia nigra lesions in Alzheimer disease and normal aging. *Alzheimer Dis. Assoc. Disord.* **9**, 61–67 (1995).
170. Brar, S., Henderson, D., Schenck, J. & Zimmerman, E. A. Iron Accumulation in the Substantia Nigra of Patients With Alzheimer Disease and Parkinsonism. *Arch. Neurol.* **66**, 371–374 (2009).
171. Zarow, C., Lyness, S. A., Mortimer, J. A. & Chui, H. C. Neuronal Loss Is Greater in the Locus Coeruleus Than Nucleus Basalis and Substantia Nigra in Alzheimer and Parkinson Diseases. *Arch. Neurol.* **60**, 337–341 (2003).
172. Burns, J. M., Galvin, J. E., Roe, C. M., Morris, J. C. & McKeel, D. W. The pathology of the substantia nigra in Alzheimer disease with extrapyramidal signs. *Neurology* **64**, 1397–1403 (2005).
173. Wiesman, A. I. *et al.* Somatosensory dysfunction is masked by variable cognitive deficits across patients on the Alzheimer's disease spectrum. *EBioMedicine* **73**, 103638 (2021).
174. Stephen, J. M. *et al.* Somatosensory responses in normal aging, mild cognitive impairment, and Alzheimer's disease. *J. Neural Transm.* **117**, 217–225 (2010).
175. Thompson, P. M. *et al.* Mapping hippocampal and ventricular change in Alzheimer disease. *Neuroimage* **22**, 1754–1766 (2004).
176. Lehtovirta, M. *et al.* Volumes of hippocampus, amygdala and frontal lobe in Alzheimer patients with different apolipoprotein E genotypes. *Neuroscience* **67**, 65–72 (1995).
177. Gosche, K. M., Mortimer, J. A., Smith, C. D., Markesbery, W. R. & Snowdon, D. A. Hippocampal volume as an index of Alzheimer neuropathology. *Neurology* **58**, 1476–1482 (2002).
178. Leuba, G. *et al.* Differential Changes in Synaptic Proteins in the Alzheimer Frontal Cortex with Marked Increase in PSD-95 Postsynaptic Protein. *J. Alzheimer's Dis.* **15**, 139–151 (2008).
179. Rao, J. S., Keleshian, V. L., Klein, S. & Rapoport, S. I. Epigenetic modifications in frontal cortex from Alzheimer's disease and bipolar disorder patients. *Transl. Psychiatry 2012 27* **2**, e132–e132 (2012).
180. DeKosky, S. T. & Scheff, S. W. Synapse loss in frontal cortex biopsies in Alzheimer's disease: Correlation with cognitive severity. *Ann. Neurol.* **27**, 457–464 (1990).
181. Kovács, T., Cairns, N. J. & Lantos, P. L. beta-amyloid deposition and neurofibrillary tangle formation in the olfactory bulb in ageing and Alzheimer's disease. *Neuropathol. Appl. Neurobiol.* **25**, 481–491 (1999).
182. Rombaux, P. *et al.* Increased olfactory bulb volume and olfactory function in early blind subjects. *Neuroreport* **21**, 1069–1073 (2010).
183. Ohm, T. G. & Braak, H. Olfactory bulb changes in Alzheimer's disease. *Acta Neuropathol. 1987 734* **73**, 365–369 (1987).
184. Zusso, M. *et al.* Regulation of postnatal forebrain amoeboid microglial cell proliferation and development by the transcription factor runx1. *J. Neurosci.* **32**, 11285–11298 (2012).
185. Adams, H. *et al.* Persistence Images: A Stable Vector Representation of Persistent Homology. *J. Mach. Learn. Res.* **18**, 1–35 (2017).
186. Van Der Maaten, L. & Hinton, G. Visualizing Data using t-SNE. *J. Mach. Learn. Res.* **9**, 2579–2605 (2008).
187. Lenz, K. M., Nugent, B. M., Haliyur, R. & McCarthy, M. M. Microglia are essential to masculinization of brain and behavior. *J. Neurosci.* **33**, 2761–2772 (2013).
188. Han, J., Fan, Y., Zhou, K., Blomgren, K. & Harris, R. A. Uncovering sex differences of rodent microglia. *J. Neuroinflammation 2021 181* **18**, 1–11 (2021).
189. Caligioni, C. S. Assessing reproductive status/stages in mice. *Curr. Protoc. Neurosci.*

Appendix (2009). doi:10.1002/0471142301.nsa04is48
190. Perez-Pouchoulen, M., VanRyzin, J. W. & McCarthy, M. M. Morphological and phagocytic profile of microglia in the developing rat cerebellum. *eNeuro* **2**, 36–51 (2015).
191. Yang, J. M., Zhang, J., Yu, Y. Q., Duan, S. & Li, X. M. Postnatal development of 2 microcircuits involving fast-spiking interneurons in the mouse prefrontal cortex. *Cereb. Cortex* **24**, 98–109 (2014).
192. Wong, T. *et al.* Postnatal development of intrinsic GABAergic rhythms in mouse hippocampus. *Neuroscience* **134**, 107–120 (2005).
193. Kroon, T., van Hugte, E., van Linge, L., Mansvelder, H. D. & Meredith, R. M. Early postnatal development of pyramidal neurons across layers of the mouse medial prefrontal cortex. *Sci. Rep.* **9**, 1–16 (2019).
194. Terry, R. D. Cell death or synaptic loss in Alzheimer disease. *Journal of Neuropathology and Experimental Neurology* **59**, 1118–1119 (2000).
195. Serrano-Pozo, A., Frosch, M. P., Masliah, E. & Hyman, B. T. Neuropathological alterations in Alzheimer disease. *Cold Spring Harb. Perspect. Med.* **1**, a006189 (2011).
196. Hemonnot, A. L., Hua, J., Ulmann, L. & Hirbec, H. Microglia in Alzheimer disease: Well-known targets and new opportunities. *Frontiers in Cellular and Infection Microbiology* **9**, 233 (2019).
197. Taipa, R. *et al.* Inflammatory pathology markers (activated microglia and reactive astrocytes) in early and late onset Alzheimer disease: a post mortem study. *Neuropathol. Appl. Neurobiol.* **44**, 298–313 (2018).
198. Congdon, E. E. Sex differences in autophagy contribute to female vulnerability in Alzheimer's disease. *Frontiers in Neuroscience* **12**, 372 (2018).
199. Gamache, J., Yun, Y. & Chiba-Falek, O. Sex-dependent effect of APOE on Alzheimer's disease and other age-related neurodegenerative disorders. *Dis. Model. Mech.* **13**, (2020).
200. Manji, Z. *et al.* 5xFAD Mice Display Sex-Dependent Inflammatory Gene Induction During the Prodromal Stage of Alzheimer's Disease. *J. Alzheimer's Dis.* **70**, 1259–1274 (2019).
201. Oakley, H. *et al.* Intraneuronal β-amyloid aggregates, neurodegeneration, and neuron loss in transgenic mice with five familial Alzheimer's disease mutations: Potential factors in amyloid plaque formation. *J. Neurosci.* **26**, 10129–10140 (2006).
202. Chistiakov, D. A., Killingsworth, M. C., Myasoedova, V. A., Orekhov, A. N. & Bobryshev, Y. V. CD68/macrosialin: Not just a histochemical marker. *Lab. Investig.* **97**, 4–13 (2017).
203. Struble, R. G. & Clark, H. B. Olfactory bulb lesions in alzheimer's disease. *Neurobiol. Aging* **13**, 469–473 (1992).
204. Cruz, J. C. & Tsai, L. H. A Jekyll and Hyde kinase: Roles for Cdk5 in brain development and disease. *Current Opinion in Neurobiology* **14**, 390–394 (2004).
205. Camins, A., Verdaguer, E., Folch, J., Canudas, A. M. & Pallàs, M. The role of CDK5/P25 formation/inhibition in neurodegeneration. *Drug News and Perspectives* **19**, 453–460 (2006).
206. Wang, X., Zhang, C., Szábo, G. & Sun, Q. Q. Distribution of CaMKIIα expression in the brain in vivo, studied by CaMKIIα-GFP mice. *Brain Res.* **1518**, 9–25 (2013).
207. Trapnell, C. *et al.* The dynamics and regulators of cell fate decisions are revealed by pseudotemporal ordering of single cells. *Nat. Biotechnol. 2014 324* **32**, 381–386 (2014).
208. Bijari, K., Valera, G., López-Schier, H. & Ascoli, G. A. Quantitative neuronal morphometry by supervised and unsupervised learning. *STAR Protoc.* **2**, 100867 (2021).
209. Grabert, K. & McColl, B. W. Isolation and phenotyping of adult mouse microglial cells.

in *Methods in Molecular Biology* **1784**, 77–86 (Humana Press Inc., 2018).
210. Payami, H. *et al.* Gender difference in apolipoprotein E - associated risk for familial alzheimer disease: A possible clue to the higher incidence of alzheimer disease in women. *Am. J. Hum. Genet.* **58**, 803–811 (1996).
211. Turner, R. S. Alzheimer's disease in man and transgenic mice: Females at higher risk. *American Journal of Pathology* **158**, 797–801 (2001).
212. Lenz, K. M. & McCarthy, M. M. A starring role for microglia in brain sex differences. *Neuroscientist* **21**, 306–321 (2015).
213. Nissen, J. C. Microglial function across the spectrum of age and gender. *International Journal of Molecular Sciences* **18**, (2017).
214. Ayata, P. *et al.* Epigenetic regulation of brain region-specific microglia clearance activity. *Nat. Neurosci.* **21**, 1049–1060 (2018).
215. Villa, A., Vegeto, E., Poletti, A. & Maggi, A. Estrogens, Neuroinflammation, and Neurodegeneration. *Endocr. Rev.* **37**, 372 (2016).
216. Crain, J. M. & Watters, J. J. Estrogen and P2 purinergic receptor systems in microglia: Therapeutic targets for neuroprotection. *Open Drug Discovery Journal* **2**, 148–167 (2010).
217. Bruce-Keller, A. J. *et al.* Antiinflammatory effects of estrogen on microglial activation. *Endocrinology* **141**, 3646–3656 (2000).
218. Maklad, A. & Fritzsch, B. Development of vestibular afferent projections into the hindbrain and their central targets. *Brain Research Bulletin* **60**, 497–510 (2003).
219. Hattori, T. & McGeer, P. L. Synaptogenesis in the corpus striatum of infant rat. *Exp. Neurol.* **38**, 70–79 (1973).
220. Tremblay, M.-È. *et al.* The role of microglia in the healthy brain. *J. Neurosci.* **31**, 16064–9 (2011).
221. Masland, R. H. The fundamental plan of the retina. *Nat. Neurosci. 2001 49* **4**, 877–886 (2001).
222. Jacobson, M. & Hirose, G. Origin of the Retina from Both Sides of the Embryonic Brain: A Contribution to the Problem of Crossing at the Optic Chiasma. *Science (80-.).* **202**, 637–639 (1978).
223. Yamauchi, K. & Yamadori, T. Retinal Projection to the Inferior Colliculus in the Rat. *Cells Tissues Organs* **114**, 355–360 (1982).
224. Kerschensteiner, D. & Guido, W. Organization of the dorsal lateral geniculate nucleus in the mouse. *Vis. Neurosci.* **34**, E008 (2017).
225. Reichenbach, A. & Bringmann, A. New functions of Müller cells. *Glia* **61**, 651–678 (2013).
226. Luna, G. *et al.* Astrocyte structural reactivity and plasticity in models of retinal detachment. *Exp. Eye Res.* **150**, 4–21 (2016).
227. Li, F., Jiang, D. & Samuel, M. A. Microglia in the developing retina. *Neural Dev. 2019 141* **14**, 1–13 (2019).
228. O'Koren, E. G. *et al.* Microglial Function Is Distinct in Different Anatomical Locations during Retinal Homeostasis and Degeneration. *Immunity* **50**, 723-737.e7 (2019).
229. Santos, A. M. *et al.* Embryonic and postnatal development of microglial cells in the mouse retina. *J. Comp. Neurol.* **506**, 224–239 (2008).
230. Maes, M. E., Colombo, G., Sternberg, F., Pohl, E. E. & Siegert, S. Sex, stress and UCP2: mitochondria illuminate microglial identity beyond the dichotomy. *https://www.biorxiv.org/content/10.1101/2022.08.22.504738v1.full.pdf*
231. Pei, Y. F. & Rhodin, J. A. G. The prenatal development of the mouse eye. *Anat. Rec.* **168**, 105–125 (1970).
232. Silverman, S. M. & Wong, W. T. Microglia in the Retina: Roles in Development,

Maturity, and Disease. *https://doi.org/10.1146/annurev-vision-091517-034425* **4**, 45–77 (2018).
233. Schafer, D. P. & Stevens, B. Phagocytic glial cells: sculpting synaptic circuits in the developing nervous system. doi:10.1016/j.conb.2013.09.012
234. Huang, T., Cui, J., Li, L., Hitchcock, P. F. & Li, Y. The role of microglia in the neurogenesis of zebrafish retina. *Biochem. Biophys. Res. Commun.* **421**, 214–220 (2012).
235. Schafer, D. P. *et al.* Microglia Sculpt Postnatal Neural Circuits in an Activity and Complement-Dependent Manner. *Neuron* **74**, 691–705 (2012).
236. Lawson, L. J., Perry, V. H. & Gordon, S. Turnover of resident microglia in the normal adult mouse brain. *Neuroscience* **48**, 405–415 (1992).
237. Greter, M. *et al.* Stroma-derived interleukin-34 controls the development and maintenance of langerhans cells and the maintenance of microglia. *Immunity* **37**, 1050–1060 (2012).
238. Hilla, A. M., Diekmann, H. & Fischer, D. Microglia Are Irrelevant for Neuronal Degeneration and Axon Regeneration after Acute Injury. *J. Neurosci.* **37**, 6113 (2017).
239. Zabel, M. K. *et al.* Microglial phagocytosis and activation underlying photoreceptor degeneration is regulated by CX3CL1-CX3CR1 signaling in a mouse model of retinitis pigmentosa. *Glia* **64**, 1479–1491 (2016).
240. Roche, S. L., Wyse-Jackson, A. C., Ruiz-Lopez, A. M., Byrne, A. M. & Cotter, T. G. Fractalkine-CX3CR1 signaling is critical for progesterone-mediated neuroprotection in the retina. *Sci. Rep.* **7**, (2017).
241. Kezic, J. M., Chen, X., Rakoczy, E. P. & Mcmenamin, P. G. The Effects of Age and Cx 3 cr1 Deficiency on Retinal Microglia in the Ins2 Akita Diabetic Mouse. (2013). doi:10.1167/iovs.12-10876
242. Chen, L., Yang, P. & Kijlstra, A. Distribution, markers, and functions of retinal microglia. *http://dx.doi.org/10.1076/ocii.10.1.27.10328* **10**, 27–39 (2009).
243. Wang, X. *et al.* Requirement for Microglia for the Maintenance of Synaptic Function and Integrity in the Mature Retina. *J. Neurosci.* **36**, 2827–2842 (2016).
244. Hartong, D. T., Berson, E. L. & Dryja, T. P. Retinitis pigmentosa. *Lancet* **368**, 1795–1809 (2006).
245. Weinreb, R. N., Aung, T. & Medeiros, F. A. The Pathophysiology and Treatment of Glaucoma: A Review. *JAMA* **311**, 1901–1911 (2014).
246. Norris, G. T. *et al.* Neuronal integrity and complement control synaptic material clearance by microglia after CNS injury. *J. Exp. Med.* **215**, 1789–1801 (2018).
247. Gargini, C., Terzibasi, E., Mazzoni, F. & Strettoi, E. Retinal organization in the retinal degeneration 10 (rd10) mutant mouse: A morphological and ERG study. *J. Comp. Neurol.* **500**, 222–238 (2007).
248. Otani, A. *et al.* Rescue of retinal degeneration by intravitreally injected adult bone marrow–derived lineage-negative hematopoietic stem cells. *J. Clin. Invest.* **114**, 765–774 (2004).
249. Rex, T. S. *et al.* Systemic but not intraocular Epo Gene Transfer Protects the Retina from Light-and Genetic-Induced Degeneration. *Mol. Ther.* **10**, 855–861 (2004).
250. Chang, B. *et al.* Retinal degeneration mutants in the mouse. *Vision Res.* **42**, 517–525 (2002).
251. Chang, B. *et al.* Two mouse retinal degenerations caused by missense mutations in the β-subunit of rod cGMP phosphodiesterase gene. *Vision Res.* **47**, 624–633 (2007).
252. Shen, N., Wang, B., Soto, F. & Kerschensteiner, D. Homeostatic Plasticity Shapes the Retinal Response to Photoreceptor Degeneration. *Curr. Biol.* **30**, 1916-1926.e3 (2020).
253. Zhao, L. *et al.* Microglial phagocytosis of living photoreceptors contributes to inherited

retinal degeneration. *EMBO Mol. Med.* **7**, 1179–1197 (2015).
254. Peng, B. *et al.* Suppression of Microglial Activation Is Neuroprotective in a Mouse Model of Human Retinitis Pigmentosa. *J. Neurosci.* **34**, 8139–8150 (2014).
255. Arroba, A. I., Álvarez-Lindo, N., van Rooijen, N. & de la Rosa, E. J. Microglia-Mediated IGF-I Neuroprotection in the rd10 Mouse Model of Retinitis Pigmentosa. *Invest. Ophthalmol. Vis. Sci.* **52**, 9124–9130 (2011).
256. Cammalleri, M. Optic nerve crush as a model of retinal ganglion cell degeneration. *Ann. Eye Sci.* **7**, 17–17 (2022).
257. Williams, P. R., Benowitz, L. I., Goldberg, J. L. & He, Z. Axon Regeneration in the Mammalian Optic Nerve. *https://doi.org/10.1146/annurev-vision-022720-094953* **6**, 195–213 (2020).
258. Li, Y., Schlamp, C. L. & Nickells, R. W. Experimental induction of retinal ganglion cell death in adult mice. *Investig. Ophthalmol. Vis. Sci.* **40**, 1004–1008 (1999).
259. Au, N. P. B. & Ma, C. H. E. Neuroinflammation, Microglia and Implications for Retinal Ganglion Cell Survival and Axon Regeneration in Traumatic Optic Neuropathy. *Front. Immunol.* **13**, 860 (2022).
260. Heuss, N. D. *et al.* Optic nerve as a source of activated retinal microglia post-injury. *Acta Neuropathol. Commun.* **6**, 66 (2018).
261. Ramirez, A. I. *et al.* The role of microglia in retinal neurodegeneration: Alzheimer's disease, Parkinson, and glaucoma. *Front. Aging Neurosci.* **9**, 214 (2017).
262. Li, B. *et al.* Sex-related differences in the progressive retinal degeneration of the rd10 mouse. *Exp. Eye Res.* **187**, (2019).
263. Nadal-Nicolás, F. M. *et al.* Microglial dynamics after axotomy-induced retinal ganglion cell death. *J. Neuroinflammation* **14**, (2017).
264. Nuzzi, R., Scalabrin, S., Becco, A. & Panzica, G. Sex hormones and optic nerve disorders: A review. *Front. Neurosci.* **13**, 57 (2019).
265. Polavaram, S., Gillette, T. A., Parekh, R. & Ascoli, G. A. Statistical analysis and data mining of digital reconstructions of dendritic morphologies. *Front. Neuroanat.* **8**, 138 (2014).